DISS. ETH NO. 28557

Imaging oceanic electrical conductivity structures by jointly inverting multi-source electromagnetic transfer functions. An approach, implementation and results

A dissertation submitted to attain the degree of

DOCTOR OF SCIENCES of ETH ZURICH
(Dr. sc. ETH Zürich)

presented by

CHAOJIAN CHEN

Master of Engineering in Applied Geophysics,
Central South University, Changsha, China
born on April 14, 1993
citizen of China

accepted on the recommendation of

Prof. Dr. Alexey Kuvshinov, ETH Zürich, examiner
Dr. Mikhail Kruglyakov, University of Otago, co-examiner
Prof. Dr. Andreas Junge, Goethe University, co-examiner
Prof. Dr. Jakub Velimský, Charles University, co-examiner
Prof. Dr. Martin Saar, ETH Zürich, co-examiner

2022

To my parents and sister

Abstract

Determining the physical properties of the Earth's interior in oceanic regions attracts widespread interest in geosciences. Seismic tomography has already provided a variety of global three-dimensional (3-D) velocity models. However, the interpretation of these models is often uncertain in terms of thermodynamical and compositional parameters. An alternative approach to directly probing the Earth's physical properties is the electromagnetic (EM) method, which reveals the electrical conductivity structures of the Earth. Electrical conductivity provides a wealth of information on the thermal and compositional state of the Earth's interior, being highly sensitive to fractions of conductive phases, such as fluids and partial melts. One data source to probe the oceanic conductivity distribution is magnetic field variations measured at island geomagnetic observatories. From these data one can estimate: a) magnetotelluric (MT) tippers, which can be inverted to study the relatively shallow Earth's structures and b) longer-period geomagnetic depth sounding (GDS) transfer functions (TFs), which can be inverted to probe the deeper structures of the Earth. Usually, the analysis of tippers is performed in Cartesian geometry, whereas the analysis of GDS TFs – in spherical geometry. The challenge here is that both MT and GDS responses at island observatories may be strongly distorted by the effects of lateral conductivity contrast between land and ocean (ocean induction effect; OIE), which should be accounted for – through modelling – as accurate as possible. Moreover, so far the island tippers and GDS TFs are inverted separately resulting in a reduced vertical resolution of the recovered models.

The main objectives of this work are three-fold: (a) to develop 3-D EM forward modelling tools to compute island MT tippers and GDS responses efficiently and accurately; (b) to develop a tool to simultaneously invert MT and GDS TFs; and (c) constrain local conductivity distributions beneath islands and try to explain the lateral variability of the recovered conductivity models.

Regarding computations of GDS responses, I developed and validated a global-to-Cartesian (G2C) 3-D EM forward modelling tool which is based on a nested integral equation (IE) approach. Within this approach, the IE modelling in spherical geometry

is first performed on the whole globe using a coarse grid, and then the results are refined in the region of interest by performing computations in Cartesian geometry at a smaller domain and on a denser grid. At the latter stage, the modelling results obtained at the previous step are exploited. It allowed me to compute GDS TFs in the problem setups requiring highly detailed laterally-variable bathymetry – an entity which controls the strength and spatial structure of OIE. I computed (long-period) GDS responses at two island geomagnetic observatories (Cocos-Keeling and Honolulu) by exploiting different – from relatively coarse, $1° \times 1°$, to immensely fine, $0.01° \times 0.01°$ – lateral grids, and demonstrate that very local bathymetry variations substantially influence the GDS responses at periods as long as 20 days. Besides, high-resolution modelling using the G2C tool makes it possible to explain anomalous behaviour of the experimental GDS responses on the island observatories.

As for computations of MT tippers, I developed a Cartesian-to-Cartesian (C2C) 3-D EM forward modelling tool, which is also based on a nested IE approach. An important novelty of the tool that distinguishes it from the G2C tool is developing a "rim-domain" concept that further improves the performance of the multi-nested IE approach. I verified the C2C tool on both idealized and realistic 3-D conductivity models and demonstrated its efficiency and accuracy. In particular, I succeeded in reproducing experimental tippers at observatory Gan (located on the southernmost island of the Maldives archipelago), which required modelling at very fine meshes.

Further, I developed – based on the above-discussed tools – a quasi-1D tool to simultaneously invert multi-source EM responses, including MT tippers (with periods ranging from a few minutes to 3 hours), solar quiet (Sq) global-to-local (G2L) TFs (with periods ranging from 6 hours to 24 hours) of ionospheric origin, and magnetospheric global Q-responses (with periods ranging from a few days to a few months). Note that the term "quasi" is used to stress that during 1-D inversions, the three-dimensional (3-D) forward modelling operator is invoked to account for OIE.

Finally, I implemented the developed tool to jointly invert multi-source EM responses estimated from island observatory and satellite data and obtained local 1-D conductivity profiles from crust to the upper mantle, including the mantle transition zone, beneath three island observatories. Revealed conductivity profiles indicate plume-like structures

beneath Tristan da Cunha and Oahu (Hawaii) islands. Besides, the recovered conductivity profiles imply oceanic lithosphere of different thicknesses beneath each island, confirming an age's progressive thickening of oceanic lithosphere.

Zusammenfassung

Die Bestimmung der physikalischen Eigenschaften des Erdinneren in ozeanischen Regionen stößt auf breites Interesse in den Geowissenschaften. Die seismische Tomographie hat bereits eine Vielzahl globaler dreidimensionaler (3-D) Geschwindigkeitsmodelle bereitgestellt. Allerdings ist die Interpretation dieser Modelle hinsichtlich thermodynamischer und kompositorischer Parameter oft unsicher. Ein alternativer Ansatz zur direkten Untersuchung der physikalischen Eigenschaften der Erde ist die elektromagnetische (EM) Methode, die die elektrischen Leitfähigkeitsstrukturen der Erde aufzeigt. Die elektrische Leitfähigkeit liefert eine Fülle von Informationen über den thermischen und Zusammensetzungszustand des Erdinneren, da sie sehr empfindlich auf Fraktionen leitfähiger Phasen wie Flüssigkeiten und Teilschmelzen reagiert. Eine Datenquelle zur Untersuchung der ozeanischen Leitfähigkeitsverteilung sind Magnetfeldvariationen, die an geomagnetischen Observatorien auf Inseln gemessen wurden. Aus diesen Daten kann man Folgendes abschätzen: a) magnetotellurische (MT) Tipper, die invertiert werden können, um die relativ flachen Erdstrukturen zu untersuchen, und b) geomagnetische Tiefensondierungs-(GDS) Transferfunktionen (TFs) mit längerer Periode, die zur Sondierung invertiert werden können die tieferen Strukturen der Erde. Normalerweise wird die Analyse von Kippern in kartesischer Geometrie durchgeführt, während die Analyse von GDS TFs in sphärische Geometrie durchgeführt wird. Die Herausforderung dabei ist, dass sowohl die MT- als auch die GDS-Antworten an Inselobservatorien durch die Auswirkungen des seitlichen Leitfähigkeitskontrasts zwischen Land und Ozean (Ozean-Induktionseffekt; OIE) stark verzerrt werden können, was – durch Modellierung – so genau wie möglich berücksichtigt werden sollte möglich. Außerdem werden die Inselkipper und GDS TFs bisher separat invertiert, was zu einer reduzierten vertikalen Auflösung der geborgenen Modelle führt.

Die Hauptziele dieser Arbeit sind dreifach: (a) Entwicklung von 3-D EM Vorwärtsmodellierungswerkzeugen zur effizienten und genauen Berechnung von Insel-MT-Kippern und GDS-Antworten; (b) Entwicklung eines Tools zur gleichzeitigen Invertierung von MT- und GDS-TFs; und (c) lokale Leitfähigkeitsverteilungen unter Inseln einschränken

und versuchen, die laterale Variabilität der gewonnenen Leitfähigkeitsmodelle zu erklären.

In Bezug auf Berechnungen von GDS-Antworten habe ich ein Global-to-Cartesian (G2C) 3-D-EM-Vorwärtsmodellierungstool entwickelt und validiert, das auf einem Ansatz mit verschachtelten Integralgleichungen (IE) basiert. Bei diesem Ansatz wird die IE-Modellierung in Kugelgeometrie zuerst auf dem gesamten Globus unter Verwendung eines groben Gitters durchgeführt, und dann werden die Ergebnisse in der interessierenden Region verfeinert, indem Berechnungen in kartesischer Geometrie in einem kleineren Bereich und auf einem dichteren Gitter durchgeführt werden. In der letzten Phase werden die im vorherigen Schritt erhaltenen Modellierungsergebnisse genutzt. Es erlaubte mir, GDS TFs in den Problemstellungen zu berechnen, die hochdetaillierte lateral-variable Bathymetrie erfordern – eine Entität, die die Stärke und räumliche Struktur von OIE steuert. Ich habe (Langzeit-)GDS-Antworten an zwei geomagnetischen Observatorien der Insel (Cocos-Keeling und Honolulu) berechnet, indem ich verschiedene ausnutzte – von relativ grob, $1° \times 1°$, bis zu immens fein, $0.01° \times 0.01°$ – seitliche Gitter und zeigen, dass sehr lokale Bathymetrievariationen die GDS-Antworten in Zeiträumen von bis zu 20 Tagen wesentlich beeinflussen. Außerdem ermöglicht die hochauflösende Modellierung mit dem G2C-Tool die Erklärung des anomalen Verhaltens der experimentellen GDS-Antworten auf den Inselobservatorien.

Für Berechnungen von MT-Kippern habe ich ein Cartesian-to-Cartesian (C2C) 3-D-EM-Vorwärtsmodellierungstool entwickelt, das ebenfalls auf einem verschachtelten IE-Ansatz basiert. Eine wichtige Neuerung des Tools, die es vom G2C-Tool unterscheidet, ist die Entwicklung eines "Rim-Domain" Konzepts, das die Leistung des mehrfach verschachtelten IE-Ansatzes weiter verbessert. Ich habe das C2C-Tool sowohl auf idealisierte als auch auf realistische 3-D-Leitfähigkeit verifiziert Modellen und demonstrierte seine Effizienz und Genauigkeit.Insbesondere gelang es mir, experimentelle Tipper am Observatorium Gan (auf der südlichsten Insel des Malediven-Archipels) zu reproduzieren, was eine Modellierung mit sehr feinen Maschen erforderte.

Außerdem habe ich – basierend auf den oben diskutierten Tools – ein Quasi-1D-Tool entwickelt, um gleichzeitig EM-Antworten aus mehreren Quellen zu invertieren, einschließlich MT-Tipper (mit Perioden im Bereich von wenigen Minuten bis 3 Stun-

den), Solar Quiet (Sq) global-to-local (G2L) TFs (mit Zeiträumen von 6 Stunden bis 24 Stunden) ionosphärischen Ursprungs und magnetosphärische globale Q-Antworten (mit Zeiträumen von einigen Tagen bis zu einigen Monaten). Beachten Sie, dass der Begriff "quasi"verwendet wird, um zu betonen, dass während 1-D-Inversionen der dreidimensionale (3-D) Vorwärtsmodellierungsoperator aufgerufen wird, um OIE zu berücksichtigen.

Schließlich implementierte ich das entwickelte Tool, um gemeinsam EM-Reaktionen aus mehreren Quellen zu invertieren, die aus Inselobservatoriums- und Satellitendaten geschätzt wurden, und erhielt lokale 1-D-Leitfähigkeitsprofile von der Kruste bis zum oberen Mantel, einschließlich der Mantelübergangszone, unter drei Inselobservatorien. Aufgedeckte Leitfähigkeitsprofile weisen auf wolkenähnliche Strukturen unter den Inseln Tristan da Cunha und Oahu (Hawaii) hin. Außerdem implizieren die gewonnenen Leitfähigkeitsprofile ozeanische Lithosphäre unterschiedlicher Dicke unter jeder Insel, was die fortschreitende Verdickung der ozeanischen Lithosphäre im Laufe der Zeit bestätigt.

Contents

Chapter 1

Introduction

1.1 Motivation

The Earth's mantle provides thermal and mechanical driving forces for plate tectonics, contributing to volcanoes, seafloor spreading, and orogeny. One technique that has reached a level of maturity is seismic tomography. Seismic tomography has already provided a variety of global three-dimensional (3-D) velocity models. Still, the interpretation of these models in terms of thermodynamics is often uncertain, especially when it comes to constraints on water content (Fei et al., 2017; Schulze et al., 2018; Buchen et al., 2018). In addition, it suffers from the inability to separate compositional and thermal variations effects. An alternative approach is electromagnetic (EM) sounding, which probes the electrical conductivity distribution of the Earth's interior. As electrical conductivity is highly sensitive to temperature and the presence of conductive phases such as water and melt, it provides a wealth of information on the thermal and compositional state of the Earth's interior, helping to understand the Earth's origin, evolution, and modern dynamics (Banks, 1969; Kelbert et al., 2009; Yoshino, 2010; Shimizu et al., 2010; Khan, 2016; Johansen et al., 2019). The Earth's relatively shallow electrical conductivity structures (from near-surface down to $\sim$ 200 km) are conventionally studied with the magnetotelluric (MT) sounding technique. In contrast, deeper structures (from $\sim$ 200 km down to $\sim$ 1500 km) are probed with the geomagnetic depth sounding (GDS) method, both relying on the analysis and interpretation of electromagnetic transfer functions (TFs) in the frequency domain.

In general, continents are explored by MT and GDS methods significantly better than the oceans for two obvious reasons: a) surface observations are tied to islands that are sparsely scattered; b) seafloor observations are usually logistically as well instrumentally demanding. Despite the latter challenge, several seafloor MT surveys were performed, however, the coverage with EM observations in the oceans remains poor. In this context, the magnetic field data from island geomagnetic observatories is considered a valuable source of information about marine electrical conductivity structures. However – due to the very irregular distribution of the island observatories – at most, one can constrain the one-dimensional (1-D) conductivity structures beneath each observatory and explore the lateral variability of the recovered 1-D structures.

Previously, EM induction studies at islands primarily relied on the GDS technique (cf. Khan et al., 2011; Munch et al., 2018; Chen et al., 2020; Simpson et al., 2000; Guzavina et al., 2019). With TFs estimated from these data, one can obtain 1-D conductivity profiles (beneath specific locations) in the depth range of $\sim 200 - 1500\,\mathrm{km}$.

Samrock & Kuvshinov (2013) demonstrated that island MT tippers relating variations of vertical and horizontal magnetic field components are sensitive to 1-D conductivity distributions beneath islands at depths $\sim 0 - 200\,\mathrm{km}$. Morschhauser et al. (2019) performed "quasi" 1-D inversion of MT tippers estimated from the data at two island geomagnetic observatories and found significant lateral variability of the recovered 1-D conductivity profiles. Here the term "quasi" is used to stress that during 1-D inversion, the 3-D forward modelling operator is invoked to calculate tippers which are large due to the ocean induction effect (OIE); recall that the OIE originates from lateral conductivity contrasts between the ocean and land (Parkinson & Jones, 1979; Kuvshinov et al., 2002) and is mainly governed by local bathymetry in the region of interest.

So far, island GDS and MT TFs were analysed/inverted separately, resulting in a reduced vertical resolution of the recovered conductivity structures outside the target depths.

My Ph.D. project aims to constrain the local electrical conductivity structures beneath oceans from crust to mantle by a joint inversion of MT and GDS TFs, estimated from island geomagnetic observatory data. Special attention is paid to as accurate as feasible accounting for the OIE in island EM TFs. This is achieved by developing the

Cartesian-to-Cartesian (C2C) and global-to-Cartesian (G2C) 3-D EM forward modelling tools based on a nested integral equation (IE) approach. These tools allow us to efficiently calculate MT and GDS TFs in the problem setups which require accounting for high-resolution bathymetry in the vicinity of island observatories. Before outlining the main goals of my Ph.D. thesis in Section 1.3, I will first – in Section 1.2 – introduce MT and GDS TFs, which I will use in my work and, in addition, list some recent papers which show the progress status in MT and GDS studies.

1.2 A brief review of deep electromagnetic studies
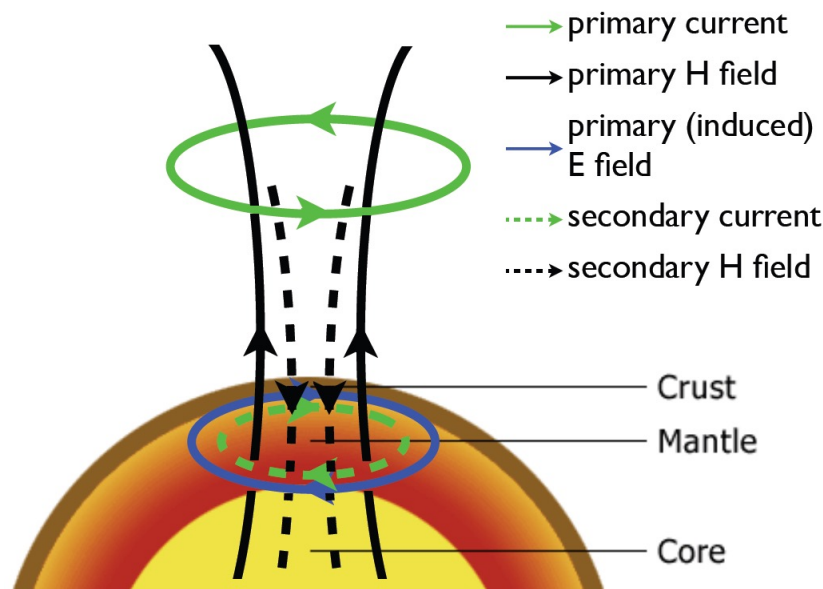
Figure 1.1: Concept of EM induction method which is taken from Püthe (2015). The primary current generates a primary (external, inducing) magnetic field. The primary magnetic field induces an electric field in the Earth, driving a secondary current. This secondary current generates a secondary (internal, induced) magnetic field. Measurements conducted above or beneath the Earth's surface contain primary and secondary magnetic fields.

The concept of the EM induction method is presented in Figure 1.1. The primary current in the magnetosphere or ionosphere generates a primary (external, inducing) magnetic field. The external magnetic field induces an electric field in the conducting Earth, which drives a secondary current. The secondary current generates a secondary (internal, induced) magnetic field in the Earth. Based on the measurements above

or below the Earth's surface, one can collect both primary and secondary (electrical and) magnetic fields. Through analyzing the measured signals, one can constrain the conductivity structures of the Earth's interior.

Table 1.1: Summary of EM methods that can be used to probe the deep Earth.

Method	Magnetotellurics	Geomagnetic depth sounding	
Source	Polar current systems/Lightnings	Ionospheric Sq current system	Magnetospheric ring current
Period band	5 min – 3 hours	4 – 24 hours	2 – 180 days
Depth range (km)	$0 - \sim 200$	$\sim 200 - \sim 500$	$\sim 500 - \sim 1500$
Data acquisition	Observatories/ Temporary stations	Observatories/ Temporary stations	Observatories/ Satellites

There are mainly two EM methods that can be used to probe deep Earth's electrical conductivity structures – the long-period MT technique and the GDS method; see Table 1.1 for details. These two methods rely on analyzing and interpreting EM transfer functions in the frequency domain. Note, that working with these TFs, one relies on the solution of Maxwell's equations in the frequency domain

$$
\begin{aligned}
\nabla \times \mathbf{H} &= \sigma \mathbf{E} + \mathbf{j}^{ext}, \\
\nabla \times \mathbf{E} &= i\omega\mu_0 \mathbf{H},
\end{aligned}
\tag{1.1}
$$

where $i = \sqrt{-1}$, $\mathbf{E}$ and $\mathbf{H}$ are electric and magnetic fields, respectively, $\mathbf{j}^{ext}$ is the extraneous current (source), σ is the Earth's conductivity distribution, $\omega = 2\pi/T$, T is the period, and μ_0 is the magnetic permeability of free space. Note that displacement currents are ignored in the considered period range and the Fourier transform convention $e^{-i\omega t}$ is adopted.

The TFs, relating various components of the (electric and magnetic) field in the frequency domain, allow us to obtain information on Earth's conductivity structures. Through inverting MT and GDS TFs, one can obtain electrical conductivity distributions in the Earth's interiors. A short summary of transfer functions used in MT and GDS studies is presented in the following section.

1.2.1 TFs of magnetotelluric method

Magnetotelluric method works with EM field variations with periods shorter than 3 hours. At these periods the source of the EM signals can be well approximated by a vertically incidenting plane wave. Plane wave approximation allows researchers to introduce MT transfer functions that are either impedances, Z, relating horizontal electric filed, $\mathbf{E}_\tau$, to the horizontal magnetic field, $\mathbf{H}_\tau = (H_x \, H_y)$, as

$$\mathbf{E}_\tau(\mathbf{r}_s, \omega) = Z(\mathbf{r}_s, \omega)\mathbf{H}_\tau(\mathbf{r}_s, \omega), \quad Z(\mathbf{r}_s, \omega) = \begin{pmatrix} Z_{xx} & Z_{xy} \\ Z_{yx} & Z_{yy} \end{pmatrix}, \tag{1.2}$$

or/and tippers, $T = (T_{zx} \, T_{zy})$, relating vertical magnetic field component, H_z, to the horizontal magnetic field, $\mathbf{H}_\tau$, as

$$H_z(\mathbf{r}_s, \omega) = T_{zx}(\mathbf{r}_s, \omega)H_x(\mathbf{r}_s, \omega) + T_{zy}(\mathbf{r}_s, \omega)H_y(\mathbf{r}_s, \omega). \tag{1.3}$$

Here $\mathbf{r}_s$ is the observation site and ω is the angular frequency,

Through inverting MT TFs, one can constrain the Earth's conductivity structures from near-surface down to approximately 200 km. Nowadays, a great amount of inland large-scale MT surveys are conducted, revealing substantial 3-D conductivity structures in many regions of the world, for instance, beneath south Australia (Heinson et al., 2006; Robertson et al., 2015), central Australia (Selway et al., 2011), northwestern USA (Bedrosian & Feucht, 2014; Meqbel et al., 2014), north-central USA (Yang et al., 2015), southeastern USA (Murphy & Egbert, 2017), Southeast China (Zhang et al., 2015; Han et al., 2021), Southwest China (Bai et al., 2010), North China (Yin et al., 2017) and contiguous USA Yang et al. (2021).

Besides, more and more seafloor MT surveys are performed (cf. Heinson et al., 1996; Baba et al., 2010; Suetsugu et al., 2012; Baba et al., 2013, 2017a; Key et al., 2013; Naif et al., 2013; Matsuno et al., 2020; Blatter et al., 2022), thus stepwise filling the gap in our knowledge about the subsurface electrical conductivity distribution in the vast oceanic regions.

1.2.2   TFs of geomagnetic depth sounding

Conventional GDS studies are mainly based on analyzing magnetic variations with periods longer than one day, measured at global net of geomagnetic observatories. These variations are generated by magnetospheric ring current, which is seen (by observer at Earth's surface) as spatially simple and described via Y_1^0, the first zonal spherical harmonic (SH) in geomagnetic coordinates. Then, the so-called local C-response can be introduced at a given site as

$$C(\mathbf{r}_a, \omega) = -\frac{a}{2} \tan\theta \frac{B_r(\mathbf{r}_a, \omega)}{B_\theta(\mathbf{r}_a, \omega)}, \qquad (1.4)$$

where a is the mean Earth's radius, θ is the geomagnetic colatitude of the observation site, and B_r and B_θ are the radial and horizontal components of the magnetic field, respectively. The complex-valued C-response has a physical dimension of length, whose real part indicates the depth to which EM field penetrates (Weidelt, 1972). By inverting (long-period) C-responses, one can constrain the Earth's conductivity structures at depths ranging from ~ 500 to ~ 1500 km.

Based on an inversion of the local C-responses, estimated at a global net of geomagnetic observatories, several global 3-D mantle conductivity models were built in the last decade (Kelbert et al., 2009; Semenov & Kuvshinov, 2012; Li et al., 2020). However, considering the very irregular spatial distribution of the geomagnetic observatories (with substantial gaps in oceanic regions), the recovery of a cogent 3-D mantle conductivity distribution beneath oceans from observatory data is probably not feasible. Moreover, the recovered conductivity distributions at upper mantle depths (< 500 km) are poorly constrained.

Tighter constraints on the electrical conductivity structures of the Earth's upper mantle require the consideration of magnetic field variations at the periods ranging from a few hours to one day, whose dominating source is ionospheric solar-quiet (Sq) current system (Yamazaki & Maute, 2017). The Sq current system has a much more complex spatio-temporal structure compared to the magnetospheric ring current, thus precluding the usage of the above-discussed local C-response concept. However, one can still estimate the local C-response without prior assumptions about source geometry by using

the Z:Y-method (Schmucker, 1985; Olsen, 1992, 1998). In this method, the C-response is given as

$$C(\mathbf{r}_a, \omega) = -\frac{B_r(\mathbf{r}_a, \omega)}{\nabla_\tau \cdot \mathbf{B}_\tau(\mathbf{r}_a, \omega)}, \tag{1.5}$$

where $\nabla_\tau \cdot \mathbf{B}_\tau$ is the angular part of the divergence of the horizontal magnetic field. However, the need to estimate the local angular derivatives of the horizontal magnetic field makes the method generally impractical.

An alternative approach to account for the complex spatio-temporal structure of the source is to estimate the so-called global-to-local (G2L) transfer functions. The concept of G2L TFs was initially proposed to account for the non-zonal contributions to the magnetospheric ring current. These TFs relate a set of SH expansion coefficients (ϵ_n^m) describing the source to various locally measured EM field components. For instance, for the vertical component, one can write (Püthe et al., 2015; Guzavina et al., 2019)

$$B_r(\mathbf{r}_s, \omega) = \sum_{n,m \in L(\omega)} \epsilon_n^m(\omega) T_n^m(\mathbf{r}_s, \omega), \tag{1.6}$$

where $L(\omega)$ specifies a subset of SH for each period. For each ω, one first determines ϵ_n^m from horizontal magnetic field components measured at the global network of observatories assuming a prior 3-D conductivity Earth. Then, the corresponding T_n^m are estimated by relating the local vertical magnetic field component with the estimated source coefficients ϵ_n^m.

1.3   Outline of the thesis

My thesis pursued four main goals: a) development of a global-to-Cartesian (G2C) 3-D EM forward modelling tool – which is based on a nested integral equation (NIE) approach – to calculate GDS responses/transfer functions efficiently; b) development of a Cartesian-to-Cartesian (C2C) 3-D EM forward modelling tool – based, also, on the NIE approach – to compute MT responses, again, efficiently; c) development of a tool to jointly invert MT and GDS responses/transfer functions using G2C and C2C solvers and stochastic optimization approach; d) ultimately implementation of the developed inversion tool to constrain the local 1-D conductivity structures beneath islands from

crust to mantle.

The structure of the thesis is as follows. Chapter 2 presents the details of the G2C tool. Using the G2C tool, I computed the long-period responses at two island (Cocos-Keeling and Honolulu) geomagnetic observatories by exploiting different – from relatively coarse $1° \times 1°$ to very fine $0.01° \times 0.01°$ – lateral grids, and demonstrate that very local bathymetry variation substantially influence the GDS responses at periods as long as 20 days. Furthermore, using the responses computed at $0.01° \times 0.01°$ grid, new 1-D conductivity models beneath considered islands were obtained, and remarkable agreement between modelled and experimental (i.e. estimated from the data) responses was observed. In particular, the anomalous behaviour of experimental C-responses at the Cocos-Keeling observatory was reproduced.

Chapter 3 presents the details of the C2C tool. The developed tool was used to calculate the MT tippers at observatory Gan, located on the southernmost island of the Maldives archipelago. The modelled tippers were compared with observed MT tippers, and, again, a remarkable agreement between modelled and experimental responses was achieved.

Chapter 4 describes the quasi-1D joint inversion tool based on a stochastic approach, as well as its application to constrain the local 1-D conductivity structures beneath three geomagnetic observatories, located at Tristan da Cunha (INTERMAGNET code of observatory: TDC), Oahu (INTERMAGNET code of observatory: HON), and Cocos-Keeling (INTERMAGNET code of observatory: CKI) islands. Revealed conductivity profiles indicate a conductive upper mantle beneath Tristan da Cunha and Oahu islands. Besides, the recovered conductivity profiles reveal oceanic lithosphere of different thicknesses beneath each island, confirming an age's progressive thickening of oceanic lithosphere.

The thesis also includes four Appendices that provide further details on the main text results. Appendix A presents the results of two numerical tests aimed at verifying the proposed global-to-Cartesian 3-D EM forward problem modelling approach discussed in Chapter 2. Appendix B details the numerical implementation of the nested C2C approach. Appendix C presents actual values for the depths to the top of each layer, thicknesses, conductivities, and 95 % confidence intervals of the layered 1-D conductivity

profiles which were recovered beneath three island geomagnetic observatories. Appendix D outlines the stochastic optimization approach, named Covariance Matrix Adaptation Evolution Strategy, adopted to solve the quasi-1D inversion problem.

Chapter 2

Global-to-Cartesian three-dimensional electromagnetic modeling using a nested integral equation approach

Summary

There is significant interest in constraining mantle conductivity structure beneath oceans. One data source to probe oceanic mantle conductivity structure is magnetic fields measured at island observatories. From these data, local electromagnetic (EM) responses are estimated and then inverted in terms of conductivity. However, island responses may be strongly distorted by the ocean induction effect (OIE) originating from conductivity contrasts between ocean and land. Insufficiently accurate accounting for OIE may lead to wrong interpretation of the responses. OIE is generally modeled by global simulations using relatively coarse grids to represent bathymetry. In this chapter, I explore whether very local bathymetry influences island responses. To address this question, a methodology for efficient modeling of effects of bathymetry of any resolution was developed.

On an example of two island observatories, I demonstrate that small-scale bathymetry dramatically influences the responses. Using new methodology, new conductivity models beneath considered islands and observe remarkable agreement between modeled and experimental responses were obtained.

2.1 Introduction

Determining the three-dimensional (3-D) distribution of physical properties in Earth's mantle attracts widespread interest in the geosciences. Seismic tomography provides a variety of global 3-D velocity models, but the interpretation of seismic velocities in terms of thermodynamics is often uncertain, especially when it comes to constraints on water content (Karato & Wang, 2013; Fei et al., 2017; Schulze et al., 2018; Buchen et al., 2018). An alternative way to probe the Earth's mantle is by means of Geomagnetic Depth Sounding (GDS), which exploits magnetic field variations of magnetospheric and/or ionospheric origin to constrain the electrical conductivity structure at depth. From these data, local GDS responses (cf. Banks (1969)) are estimated and then inverted in terms of conductivity. Since conductivity is sensitive to temperature, hydrogen content, and the presence of melt (Yoshino, 2010; Karato, 2011; Karato & Wang, 2013; Yoshino & Katsura, 2013; Khan, 2016), mapping this property constrains the chemistry and physical state of the mantle. GDS mostly relies on the data coming from a global network of geomagnetic observatories. However, bearing in mind the very irregular spatial distribution of the geomagnetic observatories (with substantial gaps in oceanic regions), the recovery of a cogent 3-D mantle conductivity model beneath oceans from observatory data is probably not feasible. At most, one can decipher local one-dimensional (1-D) conductivity profiles beneath island observatories and explore lateral variability of the recovered 1-D mantle structures. The challenge here is that the GDS responses at island observatories may be strongly distorted by the effects from lateral conductivity contrast between land and ocean (the ocean induction effect; OIE) (Parkinson & Jones, 1979; Kuvshinov et al., 2002), which in its turn may lead to misinterpretation of the results, if OIE is not accurately enough accounted or corrected for. Over the last decade, a number of GDS studies were carried out with the goal of constraining 1-D conductivity distributions beneath coastal and island geomagnetic observatories (Khan et al., 2011; Munch

et al., 2018; Guzavina et al., 2019). The OIE was modeled in these papers using a global 3-D EM forward modeling code X3DG (Kuvshinov, 2008) which is based on an integral equation (IE) approach, and is benchmarked in a number of publications (Yoshimura & Oshiman, 2002; Kelbert et al., 2014; Velímský et al., 2018, among others). Due to the high computational costs of global 3-D forward simulations, relatively coarse lateral grids (with at best $0.25° \times 0.25°$ resolution) were used to represent the OIE. However, the pronounced disagreement between modeled and observed (i.e. estimated from the data) GDS responses detected by Munch et al. (2018) at a number of island observatories raises the question of whether this discrepancy is due to very local bathymetry which is not accounted for in "coarse grid" modeling.

To address this question, a global-to-Cartesian (G2C) electromagnetic (EM) forward modeling methodology (described in Section 2.2) was developed, which also exploits the IE approach but allows to efficiently calculate the EM responses in the problem setups requiring highly detailed bathymetry in the (local) region of interest. In Section 2.3, I compute long-period responses at two island (Cocos-Keeling and Honolulu) geomagnetic observatories by exploiting different – from rather coarse $1° \times 1°$ to very fine $0.01° \times 0.01°$ – lateral grids, and demonstrate that very local bathymetry variations substantially influence the GDS responses at periods as long as 20 days. By using the responses computed at $0.01° \times 0.01°$ grid, new 1-D conductivity models beneath considered islands were obtained and remarkable agreement between modeled and experimental responses was observed. In particular, the anomalous behavior of responses at Cocos-Keeling observatory was reproduced. Finally, in Section 2.4, I summarize the findings of this work, and discuss the potential ways to better constrain conductivity distribution in oceanic mantle.

2.2 Methods

2.2.1 Conventional IE approach

In the frequency domain and for a given 3-D conductivity model of the Earth, σ, and a given source, $\mathbf{j}^{ext}$, the electric, $\mathbf{E}$, and magnetic, $\mathbf{H}$, fields obey Maxwell's equations:

$$\nabla \times \mathbf{H}(\mathbf{r}) \;=\; \sigma(\mathbf{r})\mathbf{E}(\mathbf{r}) + \mathbf{j}^{ext}(\mathbf{r}), \tag{2.1}$$

$$\nabla \times \mathbf{E}(\mathbf{r}) \;=\; i\omega\mu_0\mathbf{H}(\mathbf{r}), \tag{2.2}$$

where $i = \sqrt{-1}$, μ_0 is the magnetic permeability of free space and ω angular frequency. For global (spherical) and local (Cartesian) problem setups, $\mathbf{r} = (r, \theta, \phi)$, and $\mathbf{r} = (x, y, z)$, respectively. Displacement currents are neglected in the considered period range, and the Fourier transform convention $e^{-i\omega t}$ is adopted. Note, that hereinafter the dependence of the fields on ω is omitted but implied.

Within an IE approach, eqs (2.1)-(2.2) are reduced to the IE with respect to the electric field:

$$\mathbf{E}(\mathbf{r}) - \int_{V^1} \widehat{G}_{1D}^{ej}(\mathbf{r}, \mathbf{r}')\Delta\sigma(\mathbf{r}')\mathbf{E}(\mathbf{r}')dv' = \mathbf{E}_0(\mathbf{r}),\ \mathbf{r} \in V^1, \tag{2.3}$$

where V^1 is the region in which $\Delta\sigma = \sigma - \sigma_0 \neq 0$, σ_0 is the background 1-D conductivity distribution, $\mathbf{E}_0$ the background electric field, and $\widehat{G}_{1D}^{ej}$ the "electric" dyadic Green's tensor (Kuvshinov & Semenov, 2012; Kruglyakov & Bloshanskaya, 2017).

After solving eq. (3.9), the electric and magnetic fields at any location $\mathbf{r}$ are calculated as:

$$\mathbf{E}(\mathbf{r}) = \mathbf{E}_0(\mathbf{r}) + \int_{V^1} \widehat{G}_{1D}^{ej}(\mathbf{r}, \mathbf{r}')\Delta\sigma(\mathbf{r}')\mathbf{E}(\mathbf{r}')dv', \tag{2.4}$$

$$\mathbf{H}(\mathbf{r}) = \mathbf{H}_0(\mathbf{r}) + \int_{V^1} \widehat{G}_{1D}^{hj}(\mathbf{r}, \mathbf{r}')\Delta\sigma(\mathbf{r}')\mathbf{E}(\mathbf{r}')dv', \tag{2.5}$$

where $\mathbf{H}_0$ is the background magnetic field, and $\widehat{G}_{1D}^{hj}$ is the "magnetic" dyadic Green's tensor. Similarly as for the fields, the dependence of Green's tensors on ω is omitted but implied.

In the most of IE solvers, 1-D or 2-D fast Fourier transforms (FFT) are used to

significantly decrease computational loads while performing the integration. For global simulations (invoking spherical geometry) the complexity is of order $O(N_\phi N_\theta^2 N_r^2)$, where N_ϕ, N_θ and N_r are the number of cells in the ϕ-, θ- and r-directions, respectively. In local simulations (invoking Cartesian geometry) the complexity is of $O(N_x N_y N_z^2)$, where N_x, N_y and N_z are the number of cells in the x-, y- and z-directions. The usage of FFT requires a uniform grid in one (for global problem setups) or in two (for local problem setups) lateral directions. Due to the global nature of the sources which are responsible for GDS magnetic field variations, the OIE is generally modeled by means of global 3-D EM simulations. However, in order to simulate effects from small-scale bathymetry, global simulations based on a FFT-based IE approach require prohibitively high computational loads. The next section explains how this problem can be alleviated by using a nested IE approach which couples global (spherical) and local (Cartesian) simulations.

2.2.2   Global-to-Cartesian (G2C) approach
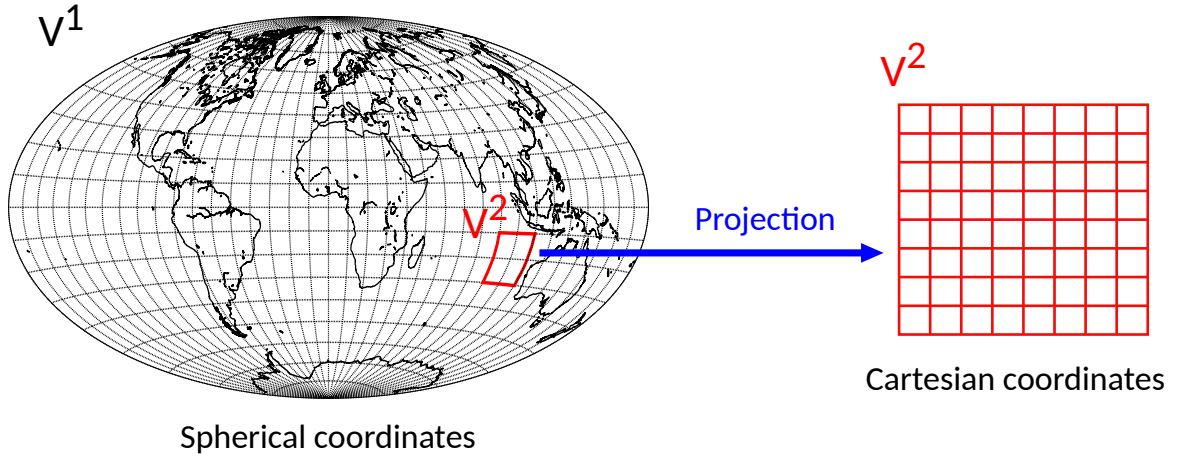
Figure 2.1: Setup for the global-to-Cartesian approach. V^1 is discretized by a coarse grid in spherical coordinates and V^2 is discretized by a fine grid in Cartesian coordinates.

The idea behind the approach is as follows. The whole (global) modeling domain, V^1, is divided into two parts: a local domain of interest, V^2, and its complement, V^1/V^2, as shown in Figure 2.1. Then eq. (3.9) can be rewritten as:

$$\mathbf{E}(\mathbf{r}) - \int_{V^2} \widehat{G}_{1D}^{ej}(\mathbf{r},\mathbf{r}')\Delta\sigma(\mathbf{r}')\mathbf{E}(\mathbf{r}')dv' = \mathbf{E}_0(\mathbf{r}) + \int_{V^1/V2} \widehat{G}_{1D}^{ej}(\mathbf{r},\mathbf{r}')\Delta\sigma(\mathbf{r}')\mathbf{E}(\mathbf{r}')dv', \ \mathbf{r} \in V^2 \quad (2.6)$$

This equation is a basis of the G2C approach. Specifically, V^1 is discretized by a coarse grid, and a global IE solver is utilized to compute "global" fields, $\mathbf{E}^{(g)}$ and $\mathbf{H}^{(g)}$, in V^1. Here, the X3DG code is used to compute $\mathbf{E}^{(g)}$ and $\mathbf{H}^{(g)}$. Then, V^2 is discretized by a fine grid, and a Cartesian IE solver is exploited to compute "Cartesian" fields, $\mathbf{E}^{(C)}$ and $\mathbf{H}^{(C)}$ in V^2. In particular, eq. (2.6) for $\mathbf{E}^{(C)}$ reads:

$$\mathbf{E}^{(C)}(\mathbf{r}) - \int_{V^2} \widehat{G}_{1D}^{ej(C)}(\mathbf{r},\mathbf{r}')\Delta\sigma^{(C)}(\mathbf{r}')\mathbf{E}^{(C)}(\mathbf{r}')dv' = P_g^C\left[\mathbf{E}_0^{(g)}(\mathbf{r}) + \mathbf{E}^{add(g)}(\mathbf{r})\right], \mathbf{r} \in V^2. \quad (2.7)$$

After solving eq. (2.7), the electric field is calculated at any location $\mathbf{r} \in V^2$ as:

$$\mathbf{E}^{(C)}(\mathbf{r}) = P_g^C\left[\mathbf{E}_0^{(g)}(\mathbf{r}) + \mathbf{E}^{add(g)}(\mathbf{r})\right] + \int_{V^2} \widehat{G}_{1D}^{ej(C)}(\mathbf{r},\mathbf{r}')\Delta\sigma^{(C)}(\mathbf{r}')\mathbf{E}^{(C)}(\mathbf{r}')dv', \quad (2.8)$$

where

$$\mathbf{E}^{add(g)}(\mathbf{r}) = \int_{V^1/V^2} \widehat{G}_{1D}^{ej(g)}(\mathbf{r},\mathbf{r}')\Delta\sigma^{(g)}(\mathbf{r}')\mathbf{E}^{(g)}(\mathbf{r}')dv'. \quad (2.9)$$

The magnetic field at any location $\mathbf{r} \in V^2$ is calculated similarly. Here, the quantities with superscripts (g) and (C) denote those calculated using global and Cartesian IE solvers, respectively, and operator P_g^C projects the fields from a global (coarse) grid to a Cartesian (fine) grid. In the implementation of G2C approach, the Mercator projection is exploited; for further details on this projection the reader is referred to Snyder (1982) and Grayver et al. (2019). In this approach, the PGIEM2G code (Kruglyakov & Kuvshinov, 2018) is adopted to compute $\mathbf{E}^{(C)}$ and $\mathbf{H}^{(C)}$. The results of numerical tests on a 1-D layered Earth model and a North-South hemisphere model, aimed to verify the developed G2C approach, are summarized in Appendix A. It is relevant to note here that for simplicity of explanation only the above mentioned two-step strategy is discussed, but the concept can be readily generalized to include multiple (nested) steps.

2.3   Results

Two geomagnetic observatories located at Cocos-Keeling (Intermagnet code of observatory: CKI) and Oahu (Intermagnet code: HON) islands, shown in Figure 2.2(b), are chosen to study the OIE in long-period responses.
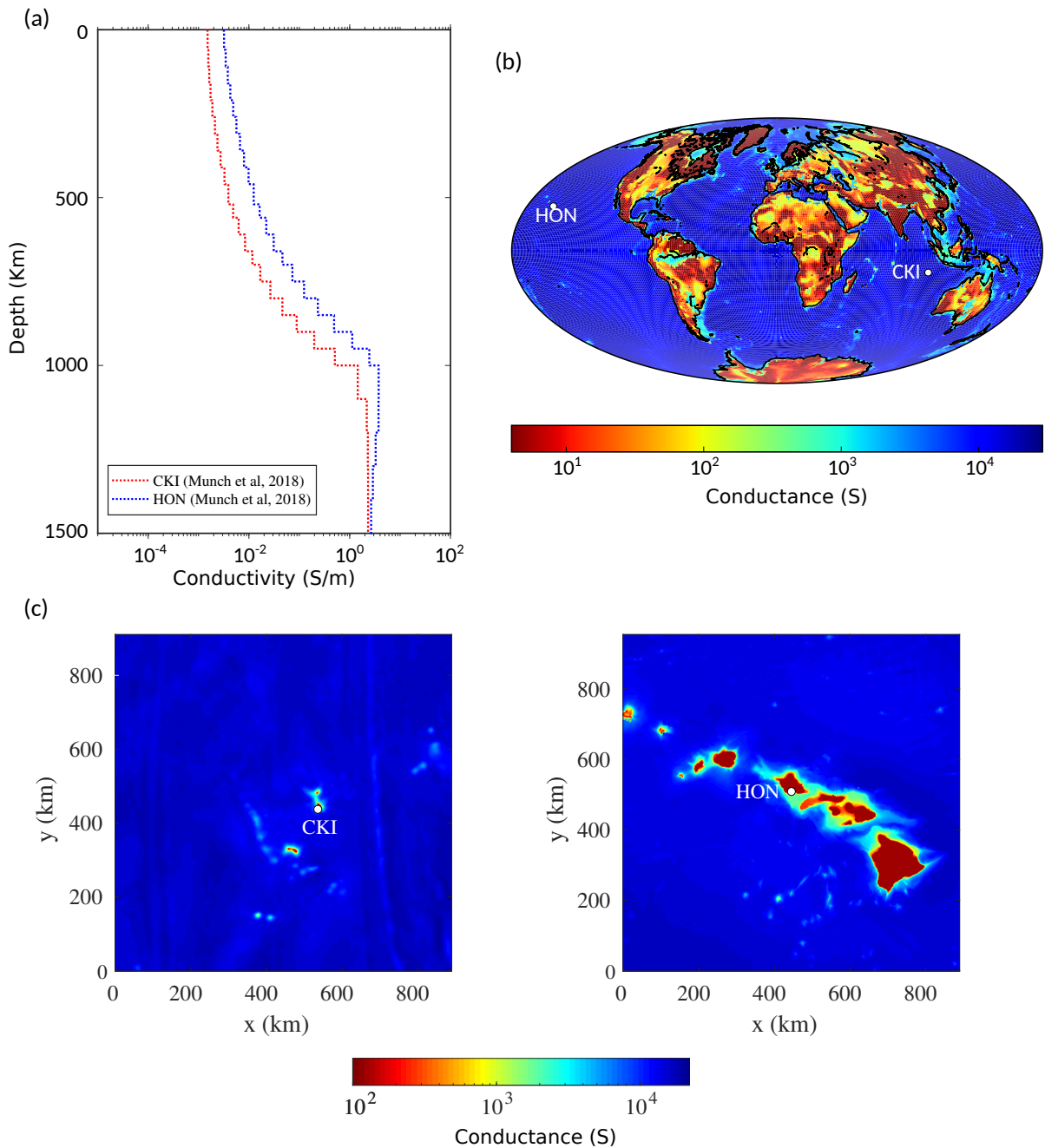
Figure 2.2: (a) 1-D conductivity profiles beneath CKI and HON observatories obtained by Munch et al. (2018), (b) conductance of the surface thin shell used in global modeling and locations of CKI and HON observatories, and (c) local conductance distributions (of resolution $0.01° \times 0.01°$) in a vicinity of CKI and HON observatories.

2.3.1   Modeling island responses

I analyze the magnetic field variations in the period range between a few days and a few months. There is a common consensus that these variations are due to a magnetospheric (ring current) source and are described via Y_1^0, the first zonal spherical harmonic in

geomagnetic coordinates. Assuming this geometry, one can determine the so-called local
C-responses as (Banks, 1969):

$$C_1(\mathbf{r}_a, \omega) = -\frac{a}{2} \tan \theta \frac{B_r(\mathbf{r}_a, \omega)}{B_\theta(\mathbf{r}_a, \omega)}, \tag{2.10}$$

where a is the mean Earth's radius, and $\mathbf{r}_a = (a, \theta, \phi)$. To explore OIE in the responses,
a conductivity model, which consists of a 1-D mantle overlaid by a surface thin shell of
known laterally-variable conductance, is used. For the periods considered in this study
– from 2.9 days to 83.2 days – the penetration depth varies approximately from 400 km
to 1200 km, which is much larger than the depth of the oceans; thus, the surface thin
shell of laterally-variable conductance is an adequate approximation of the nonuniform
distributions of conductive oceans and resistive landmasses which are responsible for the
OIE. To verify this, I calculated the responses in full 3-D models (not shown in this
Chapter) and observed only negligible difference in the results. Global (shown in Figure
2.2b) and local (shown in Figure 2.2c) conductance distributions are constructed using
bathymetry data from the ETOPO1 Global Relief Model (Amante & Eakins, 2009),
which has $0.016° \times 0.016°$ (arcmin) resolution. The land and seawater conductivities are
set as $0.02\,\mathrm{S/m}$ and $3.2\,\mathrm{S/m}$, respectively. The lateral variations of seawater conductivity
is ignored with the assumption that at considered periods the effects from such variations
are small compared to those originating from conductivity contrasts between the ocean
and land. In the course of G2C modeling, a $8° \times 8°$ region is set as the local domain
of fine grid simulations. I notice here that the lateral size of the local domain should
be large enough to account for details of the bathymetry in the vicinity of observation
site, but at the same time should be sufficiently small to minimize distortions from the
projection. Actual size of the local domain ($8° \times 8°$) is justified by using the trial and
error approach. The resolution of the conductance during the global modeling was fixed
to $1° \times 1°$, whereas during G2C simulations I varied the cell sizes in the local domain
which correspond to the conductance resolutions of $1° \times 1°$, $0.3° \times 0.3°$, $0.1° \times 0.1°$,
$0.02° \times 0.02°$ and $0.01° \times 0.01°$.

As for 1-D mantle profile which underlay the surface shell, it varied during simulations
depending on which observatory was considered. 1-D conductivity profiles beneath CKI
and HON observatories (shown in Figure 2.2a) were obtained by Munch et al. (2018)

through quasi 1-D inversion of the corresponding experimental local C-responses. Here
the term "quasi" is used to stress the fact that during 1-D inversion the 3-D forward
modeling operator was exploited by Munch et al. (2018) to account for OIE.
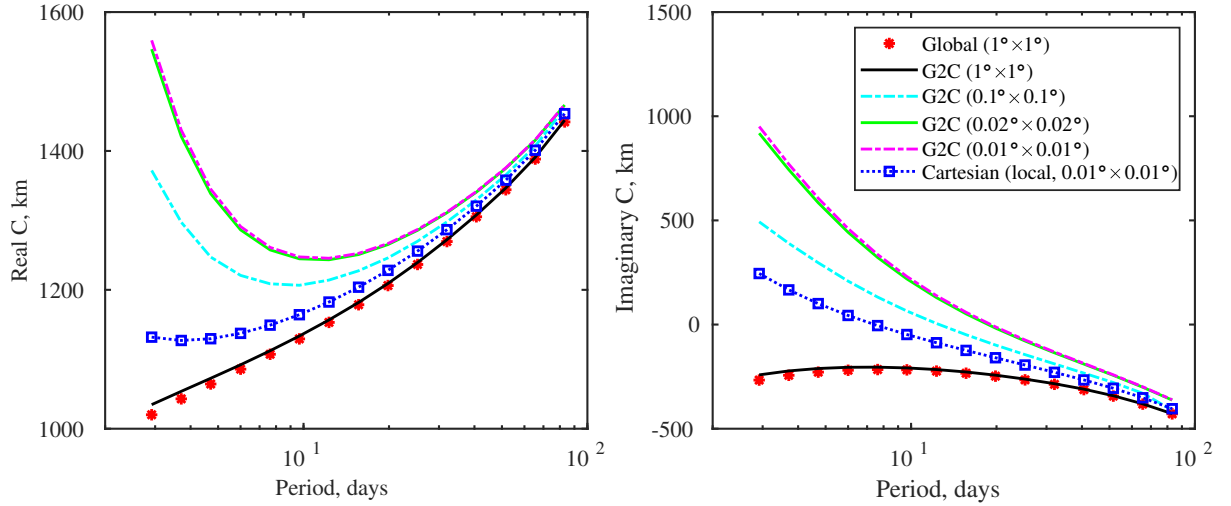
Figure 2.3: Modeled C-responses at CKI observatory. Responses are computed by
X3DG using global conductance distribution of $1° \times 1°$ resolution, by the G2C approach
using cell sizes in the local domain corresponding to conductance distributions of reso-
lutions of $1° \times 1°$, $0.1° \times 0.1°$, $0.02° \times 0.02°$ and $0.01° \times 0.01°$, and by PGIEM2G only
considering the local domain. 1-D profile from Munch et al. (2018) is used during the
modeling.

Figure 2.3 presents real and imaginary parts of the modeled C-responses at CKI
observatory. The responses calculated by global and G2C approaches using the same,
$1° \times 1°$ resolution of conductance distribution, match well as expected. Small difference
in the results at shorter periods is attributed to different numerical algorithms used
in X3DG and PGIEM2G to solve the corresponding IE. Increase of resolution during
G2C simulations from $1° \times 1°$ through $0.1° \times 0.1°$ to $0.02° \times 0.02°$ leads to significant
changes in the responses, especially in the imaginary part, and overall at periods shorter
than 20 days. Further increase of resolution up to $0.01° \times 0.01°$ change, however, the
results rather insignificantly, in spite of the fact that $0.02° \times 0.02°$ and $0.01° \times 0.01°$
conductance distributions differ by construction. Two remarks are relevant at this point.
First, the resolution as fine as $0.01° \times 0.01°$ is invoked in order to reproduce the actual
distribution of conductance around this very small island which is only a few kilometers
in size. Second, using finer than $0.01° \times 0.01°$ resolution during G2C modeling does not
make sense since our conductance distributions are constructed using bathymetry model

ETOPO1 which has a resolution of $0.016° \times 0.016°$. Summing up, I can state that for this island the conductance distributions of $0.02° \times 0.02°$ or $0.01° \times 0.01°$ resolution have to be exploited in order to accurately account for the ocean induction effect.

However, for the relatively large islands, seemingly there is no need for such high-resolution modeling to account for the OIE in local C-responses, at least in the considered period range (from a few days to a few months). Figure 2.4 illustrates this fact. It presents the modeled C-responses at HON observatory. It is seen that the responses change insignificantly when the conductance resolution in the model is finer than $0.3° \times 0.3°$. I argue that for the HON observatory conductance distribution of $0.3° \times 0.3°$ resolution is sufficient to model OIE. Note, that other possible reason that different resolutions are needed for accurate modeling OIE at different islands is the distance between the observatory site and coast; for instance, CKI observatory is much closer to the coast than HON observatory.

One can ask is there a need to account for the distant structures (for instance, nonuniform distribution of oceans and continents) during local modeling, or in other words, whether the term $\mathbf{E}^{add(g)}$ in eq. (2.8) is indeed important? To address this question, I set $\mathbf{E}^{add(g)}$ to zero and calculate C-responses (blue squares in Figures 2.3 and 2.4) using $0.01° \times 0.01°$ conductance resolution. It is seen that neglecting this term leads to rather different results. Thus, I conclude that both global and local structures must be taken into account.

2.3.2 Obtaining new 1-D profiles beneath CKI and HON observatories

As it was discussed in Introduction, Munch et al. (2018) estimated long-period C-responses at a global net of geomagnetic observatories and performed their quasi 1-D inversion using the model which incorporated the surface shell with conductance distribution of $1° \times 1°$ resolution. They detected the pronounced disagreement between modeled and experimental C-responses at a number of island observatories, including CKI observatory. Moreover, Munch et al. (2018) observed anomalous behaviour of imaginary part of the experimental CKI responses, namely change of sign at shorter periods, which they failed to reproduce. The model study described in previous section clearly
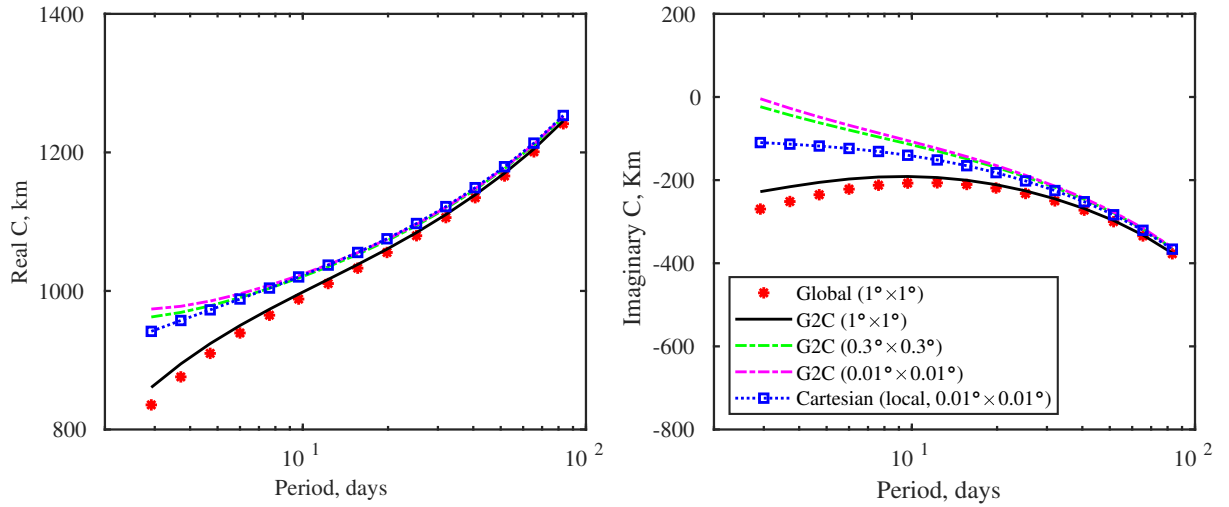
Figure 2.4: Modeled C-responses at HON observatory. Responses are computed by X3DG using global conductance distribution of $1° \times 1°$ resolution, by the G2C approach using cell sizes in the local domain corresponding to conductance distributions of resolutions of $1° \times 1°$, $0.3° \times 0.3°$, and $0.01° \times 0.01°$, and by PGIEM2G only considering the local domain. 1-D profile from Munch et al. (2018) is used during the modeling.

demonstrate that this anomalous behavior is imitable if one uses during simulations the conductance distributions of finer resolution (cf. right plot in Figure 2.3). This result motivated me to invert C-responses obtained at CKI (and HON) observatories using "surface shell" models with as fine as practicable resolution of conductance distribution in a vicinity of observation sites. New 1-D conductivity models beneath these two islands were obtained as follows. I took 1-D profiles for CKI and HON obtained by Munch et al. (2018) and computed C-responses in the models with and without surface shell, denoted by $C^{\text{1D+shell}}$ and C^{1D}, respectively. Computation of C-responses in the model with the surface shell was performed using G2C approach and exploiting local conductance distribution of $0.01° \times 0.01°$ resolution. Further I corrected the observed (i.e. estimated from the data) C-responses following the correction scheme of Kuvshinov et al. (2002)

$$C^{\text{obs,corr}}(\mathbf{r}_a, \omega) = C^{\text{obs}}(\mathbf{r}_a, \omega) \cdot \frac{C^{\text{1D}}(\mathbf{r}_a, \omega)}{C^{\text{1D+shell}}(\mathbf{r}_a, \omega)}. \tag{2.11}$$

Corrected responses were then inverted in terms of 1-D conductivity distribution. An inversion exploited Gauss-Newton optimization method as applied to a function consisting of the data misfit and regularization term. The regularization term in the implementation penalized the deviation of 1-D conductivity distribution from the reference 1-D
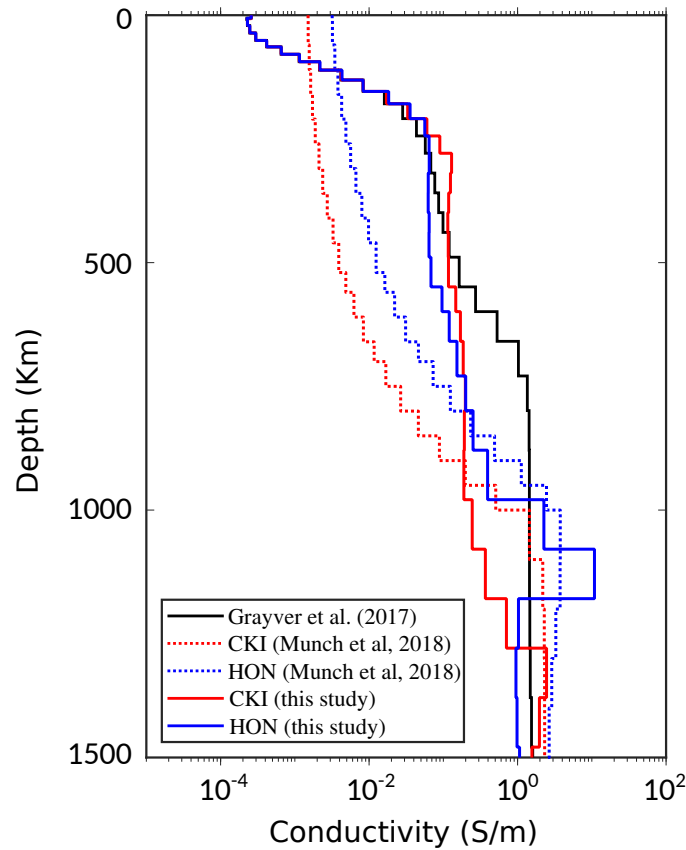
Figure 2.5: Obtained in this study (solid colored lines) and old (dashed colored lines) 1-D conductivity profiles beneath CKI and HON observatories. Black line depicts global 1-D profile from Grayver et al. (2017).

model which was taken from Grayver et al. (2017). Their model was obtained by joint inversion of satellite-detected tidal and magnetospheric signals and is believed to represent globally averaged 1-D mantle structure beneath the oceans. Old and new 1-D profiles are shown in Figure 2.5 by dashed and solid colored lines, respectively. One can see that the new profiles are very different from those obtained by Munch et al. (2018). At the same time, they are very close to the reference model of Grayver et al. (2017) at depths 0 - 250 km which is not surprising since the responses at considered periods have very limited sensitivity to upper mantle structures. At depths 500 - 1200 km both profiles significantly differ from global 1-D profile of Grayver et al. (2017), moreover they noticeably differ between each other at depths 900 - 1200 km. It is interesting that the new 1-D profile beneath HON has a prominent enhancement in conductivity at depths 1000 - 1200 km.

Finally, C-responses were computed in the model with the $0.01° \times 0.01°$ surface shell
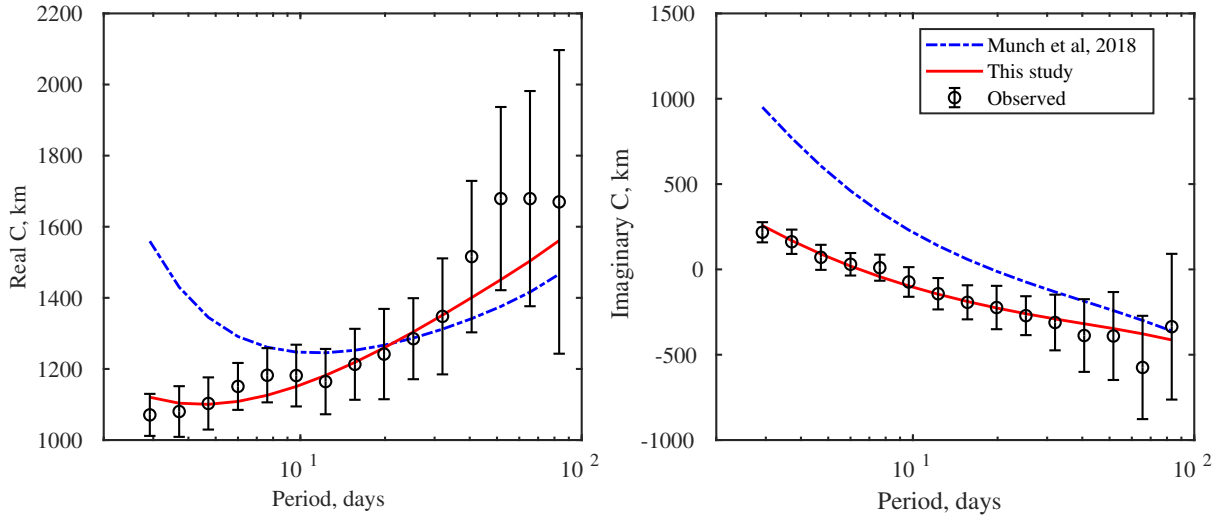
Figure 2.6: Modeled and observed *C*-responses at CKI observatory. The modeled responses are calculated by using 1-D profiles from Munch et al. (2018) and obtained in this study. Both modelings are performed by G2C approach with local conductance distribution of $0.01° \times 0.01°$ resolution. Observed responses are taken from Munch et al. (2018). Uncertainties of the observed C-responses are indicated by the error bars.
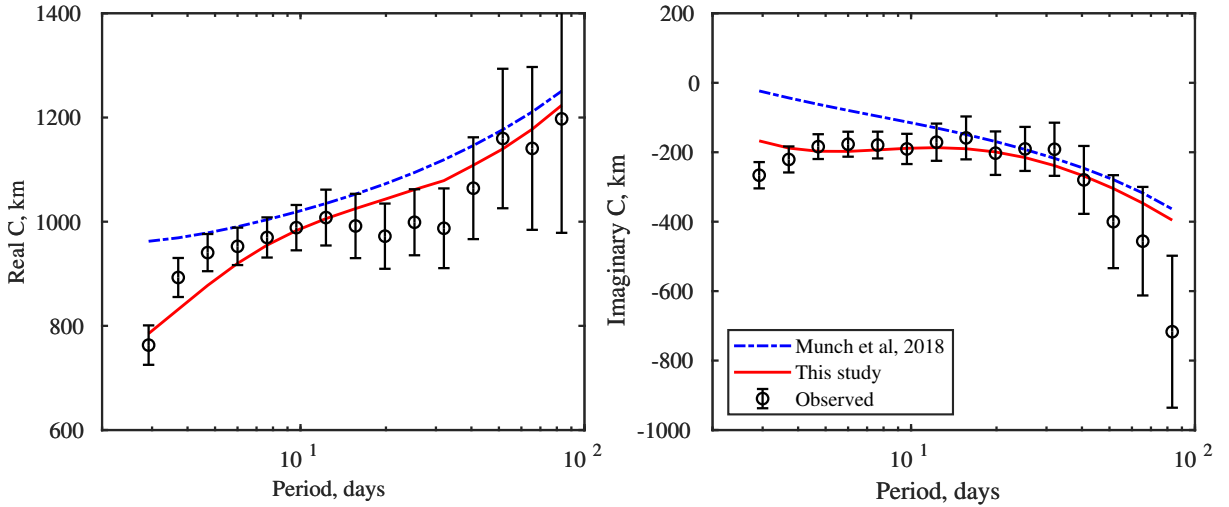
Figure 2.7: As in Figure 2.6, but for HON observatory.

and new 1-D mantle conductivity profiles underneath. Remarkably, modeled responses match very well (within the experimental uncertainties) with the observed responses for all considered periods and for both, real and imaginary, parts of the responses (cf. Figures 2.6 and 2.7). In particular, I succeeded to quantitatively reproduce anomalous behavior (change of sign) of imaginary part of *C*-response at CKI observatory. In contrast, the modeled responses obtained in the model with the $0.01° \times 0.01°$ surface shell but with the old 1-D mantle conductivity profiles underneath differ much from the observed responses.

2.4   Conclusions

In this Chapter, I revisit the ocean induction effect in long-period GDS responses at island observatories. A global-to-Cartesian (G2C) EM modeling methodology based on a nested IE approach is proposed to efficiently and accurately account for the effects from very local bathymetry. Two island, Cocos-Keeling and Honolulu, geomagnetic observatories, are chosen to study bathymetry effects in the local C-response. Numerical experiments demonstrate that very local bathymetry may dramatically influence the results, illustrating the importance of using high-resolution bathymetry when computing C-responses at island observatories.

By using G2C methodology, I obtain new 1-D conductivity models beneath considered islands and observe remarkable agreement between modeled and experimental responses. In particular, I succeeded to reproduce anomalous behavior of the responses at Cocos-Keeling observatory. An interpretation of the obtained models and their further adjustment including uncertainty quantification is beyond the scope of this work, but will be the subject of future work. Furthermore, by combining long-period responses with global-to-local Sq transfer functions (Guzavina et al., 2019) and magnetotelluric tippers (Morschhauser et al., 2019), nested IE-based inversion would provide an opportunity to probe the electrical structure of the oceanic mantle throughout its full depth range, which will be presented in Chapter 4.

Chapter 3

Cartesian-to-Cartesian three-dimensional electromagnetic modeling using a nested integral equation approach

Summary

Most of the existing three-dimensional (3-D) electromagnetic (EM) modeling solvers based on the integral equation (IE) method exploit fast Fourier transform (FFT) to accelerate the matrix-vector multiplications. This in turn requires a laterally-uniform discretization of the modeling domain. However, there is often a need for multi-scale modeling and inversion, for instance, to properly account for the effects of non-uniform distant structures, and at the same time, to accurately model the effects from local anomalies. In such scenarios, the usage of laterally-uniform grids leads to excessive computational loads, both in terms of memory and time. To alleviate this problem,

I developed an efficient 3-D EM modeling tool based on a multi-nested IE approach. Within this approach, the IE modeling is first performed at a large domain and on a (laterally-uniform) coarse grid, and then the results are refined in the region of interest by performing modeling at a smaller domain and on a (laterally-uniform) denser grid. At the latter stage, the modeling results obtained at the previous stage are exploited. The lateral uniformity of the grids at each stage allows to keep using the FFT for the matrix-vector multiplications. In addition, I proposed a "rim domain" concept to further improve the performance of the multi-nested IE approach. I verify the developed tool on both idealized and realistic 3-D conductivity models, and demonstrate its efficiency and accuracy.

3.1   Introduction

Electromagnetic (EM) methods in geophysics aim to constrain the electrical conductivity of the Earth's interior. Since the conductivity is sensitive to the temperature, chemical composition and water content, it helps to understand the Earth's origin, past evolution and modern dynamics (Yoshino, 2010; Chave & Jones, 2012; Karato & Wang, 2013; Khan, 2016; Johansen et al., 2019). Nowadays, an immense amount of EM data is available at different scales – from global to local – including the data from a global network of geomagnetic observatories (St-Louis et al., 2011), low-orbit satellites (Olsen & Floberghagen, 2018), continental-scale magnetotelluric (MT) surveys (Chopping et al., 2016; Dong & Li, 2010; Schultz, 2010), as well as from numerous regional and local EM field campaigns around the world. Most of the modern data sets require an interpretation in terms of three-dimensional (3-D) conductivity models. To perform credible and comprehensive interpretation, robust and efficient 3-D EM modeling tools are of vital importance.

There are four basic numerical simulation techniques for computing the frequency-domain EM fields and responses in the 3-D Earth's conductivity models, namely finite difference (FD) (Mackie et al., 1994; Newman & Alumbaugh, 2002; Egbert & Kelbert, 2012; Varilsuha & Candansayar, 2018; Dong & Egbert, 2019; Li et al., 2019b), finite element (FE) (Mogi, 1996; Key & Weiss, 2006; Farquharson & Miensopust, 2011; Ren et al., 2013a; Grayver & Kolev, 2015; Li et al., 2019a), finite volume (FV) (Haber & As-

cher, 2001; Haber & Ruthotto, 2014; Jahandari & Farquharson, 2014; Han et al., 2018), and integral equation (IE) (Avdeev et al., 2002a; Hursan & Zhdanov, 2002; Koyama et al., 2008; Singer, 2008) methods. The solvers based on FD, FE, and FV methods have the advantage that they generate a sparse system of linear equations, and non-uniform grids can be adopted to approximate complicated structures, for instance, topography and bathymetry. However, these solvers require a discretization of the volume which is much larger than the volume occupied by the 3-D anomalies under consideration. Moreover, the generated system of linear equations is usually poorly conditioned, thus requiring pre-conditioning. In contrast, the solvers based on the IE method only need a discretization of 3-D anomalies, which eventually leads to a smaller (but dense) matrix. Moreover, combined with the contraction operator (Pankratov & Kuvshinov, 2016), the IE technique generates a well-conditioned system of linear equations, which can be effectively solved by using iterative methods. In this chapter, I report the progress in further advancing the numerical tools based on the IE method, confining, however, to the flat Earth (Cartesian geometry) problem setups.

As mentioned before, the drawback of IE method is that it generates a dense matrix, which leads to a large computational complexity. This means that the IE method requires prohibitive computational loads if dealing with large-scale (in terms of the number of unknowns) problems. In the past several decades, significant efforts have been undertaken to improve the performance of the IE method. For instance, the matrix decomposition (MD) algorithm (Canning, 1989; Sun & Kuvshinov, 2015), fast multipole method (FMM) (Gumerov & Duraiswami, 2005; Ren et al., 2013b) and fast Fourier transform (FFT) (Avdeev et al., 2002a; Hursan & Zhdanov, 2002; Singer, 2008; Kruglyakov & Bloshanskaya, 2017, among others) were invoked to accelerate the matrix-vector multiplication – one of the core operations in the IE method – as well as to reduce the memory requirement. The MD method is rather straightforward, but in general is slower than FMM and FFT algorithms. FMM is relatively fast but intricate in implementation. In this Chapter, I exploit the FFT approach as a baseline for the improved performance of the IE method.

When Cartesian geometry is invoked in the IE method, the usage of the two-dimensional (2-D) fast Fourier transform algorithm in lateral directions tremendously reduces the

computational loads in terms of both memory and CPU time, but requires a laterally-uniform grid. However, rather often the researchers encounter situations when the data interpretation necessitates multi-scale modeling and inversion. For instance, one often needs to appropriately take into account the effects from inhomogeneous remote structures, and at the same time to accurately model the effects from local inhomogeneities, like topography and bathymetry. In this case, the usage of laterally-uniform grids leads to prohibitively high computational loads even when the 2-D FFT is used. To alleviate this problem, Nie et al. (2013) and Kamm & Pedersen (2014) applied the pre-corrected FFT method to use the non-uniform grid in the modeling domain. In their approach, the nested FFTs are utilized to approximate matrix-vector multiplication when iteratively solving the system of linear equations (Phillips & White, 1997). Another approach to address the problem is to work with nested, but still uniformly discretized, *domains*. Specifically, modeling is first performed at a large domain and on a coarse grid, and then the results are refined by performing modeling at a smaller domain and on a finer grid, exploiting at the latter step the previous "coarser grid" results.

This nested domains approach was discussed in a two-step realization by Avdeev et al. (2002) and Kuvshinov et al. (2005) as applied to the induction logging and global EM induction problems, respectively. However, both studies presented prototype solutions rather than usable tools. In Chapter 2, I developed a two-step nested IE-based tool (Chen et al., 2020) which combines the global IE (Kuvshinov, 2008) and Cartesian IE (Kruglyakov & Kuvshinov, 2018) solvers, and allows researchers to efficiently and accurately model the ocean induction effect in the long-period EM responses. Note that the global solver works in spherical geometry and thus – in contrast to the Cartesian case – allows the application of the FFT in one lateral direction only. Inspired by the successful implementation of the two-step nested IE approach in mixed (spherical and Cartesian) geometries, in this chapter, I present a nested IE-based modeling tool that exclusively works in the flat (Cartesian) Earth's models. In contrast to aforementioned (two-step) solutions, this tool may include multiple steps thus allowing recursively an increase in detail of the model in the region of interest. Moreover, I introduce in this chapter a new, "rim domain" concept, which further improves the efficacy of the nested IE approach.

The structure of this chapter is as follows. Section 3.2 presents the theoretical aspects of IE in both conventional and nested versions. Section 3.3 provides the implementation details of a nested IE approach. Section 3.4 discusses the verification of the developed tool on an example of two 3-D conductivity models. Section 3.5 summarizes the results of the work and discusses the potential directions of the future work. Further details on the numerical implementation of the nested approach are presented in Appendix B.

3.2   Theory

3.2.1   Conventional IE method

The frequency-domain electric and magnetic fields, $\mathbf{E}$ and $\mathbf{H}$, induced by the impressed (extraneous) current, $\mathbf{j}^{\mathrm{imp}}$, obey Maxwell's equations

$$\nabla \times \mathbf{H} = \sigma \mathbf{E} + \mathbf{j}^{\mathrm{imp}}, \tag{3.1}$$

$$\nabla \times \mathbf{E} = i\omega\mu_0 \mathbf{H}. \tag{3.2}$$

Here $\sigma(\mathbf{r})$ stands for a three-dimensional conductivity distribution in a model Earth, $\mathbf{r} = (x, y, z)$ denotes a right-handed Cartesian coordinate system, $i = \sqrt{-1}$, μ_0 is the magnetic permeability of free space, and ω is the angular frequency. Time dependence is accounted for by $e^{-i\omega t}$. This formulation neglects the displacement currents, which are irrelevant in the frequency range of our interest ($10^{-4} - 10^4$ Hz).

An IE approach requires introducing a one-dimensional (1-D; background) conductivity distribution $\sigma_0(z)$, and the background electric and magnetic fields, $\mathbf{E}^0$ and $\mathbf{H}^0$, which are the solutions of Maxwell's equations

$$\nabla \times \mathbf{H}^0 = \sigma_0 \mathbf{E}^0 + \mathbf{j}^{\mathrm{imp}}, \tag{3.3}$$

$$\nabla \times \mathbf{E}^0 = i\omega\mu_0 \mathbf{H}^0. \tag{3.4}$$

The fields $\mathbf{E}^0$ and $\mathbf{H}^0$ can be obtained at any location as

$$\mathbf{E}^0(\mathbf{r}) = \int\limits_{\mathrm{V^{imp}}} \widehat{G}^{ej}(\mathbf{r}, \mathbf{r}') \mathbf{j}^{\mathrm{imp}}(\mathbf{r}') d\mathrm{V}, \quad \mathbf{r} \in \mathbf{R}^3, \tag{3.5}$$

$$\mathbf{H}^0(\mathbf{r}) = \int\limits_{\mathrm{V^{imp}}} \widehat{G}^{hj}(\mathbf{r}, \mathbf{r}') \mathbf{j}^{\mathrm{imp}}(\mathbf{r}') d\mathrm{V}, \quad \mathbf{r} \in \mathbf{R}^3, \tag{3.6}$$

where, $\mathrm{V^{imp}}$ is the volume occupied by $\mathbf{j}^{\mathrm{imp}}$, and $\widehat{G}^{ej}$, $\widehat{G}^{hj}$ are the current-to-electric and current-to-magnetic Green's tensors, respectively (cf. Avdeev et al., 2002a; Kruglyakov & Bloshanskaya, 2017). Note that the fields and the current depend on ω, and Green's tensors depend on ω and $\sigma_0(z)$, however, hereafter I will omit but imply these dependencies.

By knowing $\widehat{G}^{ej}$ and $\widehat{G}^{hj}$, the electric and magnetic field solutions of eqs (3.1)-(3.2) can be written as

$$\mathbf{E}(\mathbf{r}) = \mathbf{E}^0(\mathbf{r}) + \int\limits_{\mathrm{V}} \widehat{G}^{ej}(\mathbf{r}, \mathbf{r}') \Delta\sigma(\mathbf{r}') \mathbf{E}(\mathbf{r}') d\mathrm{V}, \quad \mathbf{r} \in \mathbf{R}^3, \tag{3.7}$$

$$\mathbf{H}(\mathbf{r}) = \mathbf{H}^0(\mathbf{r}) + \int\limits_{\mathrm{V}} \widehat{G}^{hj}(\mathbf{r}, \mathbf{r}') \Delta\sigma(\mathbf{r}') \mathbf{E}(\mathbf{r}') d\mathrm{V}, \quad \mathbf{r} \in \mathbf{R}^3, \tag{3.8}$$

where V is the region where $\Delta\sigma = \sigma - \sigma_0 \neq 0$. If one finds $\mathbf{E}$ in V, one can then compute $\mathbf{E}$ and $\mathbf{H}$ at any location in space using appropriate Green's tensors. In order not to overload the narration, from now on I will discuss the computation of $\mathbf{E}$ only; $\mathbf{H}$ is computed in a similar way.

To find $\mathbf{E}(\mathbf{r})$ in V, one has to numerically solve the integral equation

$$\mathbf{E}(\mathbf{r}) - \int\limits_{\mathrm{V}} \widehat{G}^{ej}(\mathbf{r}, \mathbf{r}') \Delta\sigma(\mathbf{r}') \mathbf{E}(\mathbf{r}') d\mathrm{V} = \mathbf{E}^0(\mathbf{r}), \quad \mathbf{r} \in \mathrm{V}. \tag{3.9}$$

As mentioned in the introduction, after discretization of the above equation the resulting system matrix is dense. Hence, in the general case, the computational load (time and memory) to compute the system matrix and to solve the corresponding system with N unknowns is $\mathcal{O}(N^2)$, meaning that with realistic (large) N the problem becomes computationally demanding.

The conventional way to deal with this challenge is to exploit the fact that $\widehat{G}^{ej}$ has

convolution properties in lateral directions (Avdeev et al., 1997; Kruglyakov & Bloshanskaya, 2017)

$$\widehat{G}^{ej}(\mathbf{r}, \mathbf{r}') = \widehat{G}^{ej}(x - x', y - y', z, z').$$ (3.10)

Making use of the above convolution property and employing laterally-uniform discretization, the system matrix becomes block-Toeplitz which allows to decrease memory requirements down to $\mathcal{O}(N_\tau)$ (cf. Kruglyakov & Bloshanskaya, 2017), where N_τ is the number of unknowns in lateral directions. Moreover, the usage of 2-D FFT for performing matrix-vector multiplications – which are needed to (iteratively) solve the resulting system of linear equations – leads to computational time reduction with respect to N_τ unknowns to $\mathcal{O}(N_\tau \ln N_\tau)$. However, using laterally uniform discretization might still require large computational resources, when, for example, the problem setup dictates a large size of V and fine spatial resolution locally. In the next section, I present an approach to efficiently tackle such problem setups.

3.2.2   Nested IE (NIE) approach
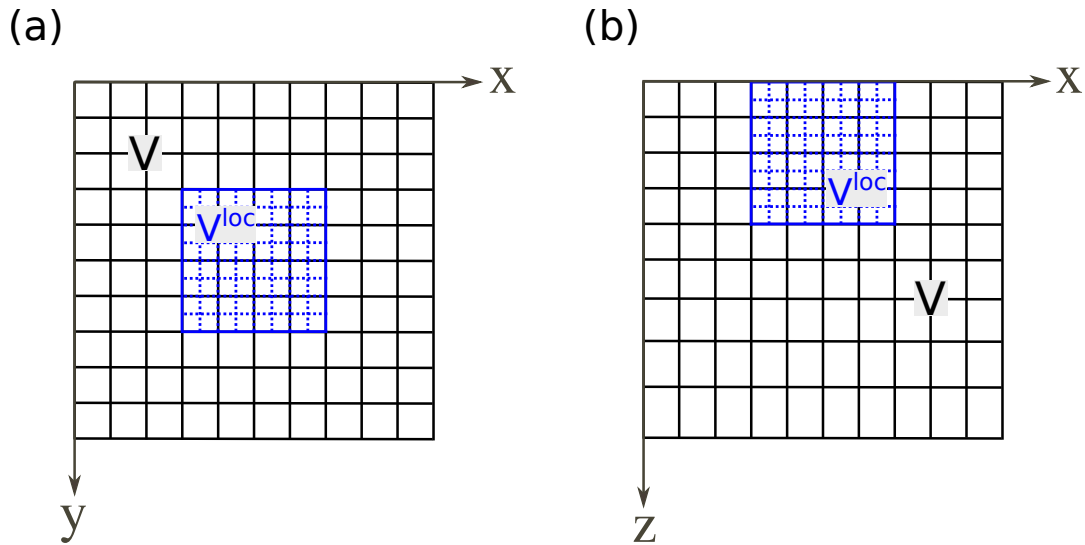
Figure 3.1: Illustration of the nested IE approach on an example of two-step realization: (a) a top view and (b) the cross section. The whole modeling domain V is divided into two parts: the local domain $\mathrm{V^{loc}}$ and it's complement $\mathrm{V^{out}}$.

Let us split the modeling domain V onto $\mathrm{V^{loc}}$ and $\mathrm{V^{out}}$ (see Figure 3.1), where $\mathrm{V^{out}}$

is the complement of V^{loc} to V, i.e.

$$V^{out} = V \setminus V^{loc}. \tag{3.11}$$

Then, for $\mathbf{r} \in V^{loc}$, we can rewrite eq. (3.9) as

$$\mathbf{E}(\mathbf{r}) - \int\limits_{V^{loc}} \widehat{G}^{ej}(\mathbf{r}, \mathbf{r}') \Delta\sigma(\mathbf{r}') \mathbf{E}(\mathbf{r}') dV = \mathbf{E}^0(\mathbf{r}) + \mathbf{E}^{add}(\mathbf{r}), \quad \mathbf{r} \in V^{loc}, \tag{3.12}$$

where

$$\mathbf{E}^{add}(\mathbf{r}) = \int\limits_{V^{out}} \widehat{G}^{ej}(\mathbf{r}, \mathbf{r}') \Delta\sigma(\mathbf{r}') \mathbf{E}(\mathbf{r}') dV, \quad \mathbf{r} \in V^{loc}. \tag{3.13}$$

The key idea of the nested IE approach (cf. Avdeev et al., 2002; Kuvshinov et al., 2005; Chen et al., 2020) is to first solve the conventional IE at a coarse grid in the whole domain V

$$\mathbf{E}^{(c)}(\mathbf{r}) - \int\limits_{V} \widehat{G}^{ej}(\mathbf{r}, \mathbf{r}') \Delta\sigma^{(c)}(\mathbf{r}') \mathbf{E}^{(c)}(\mathbf{r}') dV = \mathbf{E}^0(\mathbf{r}), \quad \mathbf{r} \in V, \tag{3.14}$$

then calculate $\mathbf{E}^{add}(\mathbf{r})$ at a finer grid in V^{loc} using $\mathbf{E}^{(c)}(\mathbf{r})$ calculated at a coarse grid in V^{out}

$$\mathbf{E}^{add\,(c)}(\mathbf{r}) = \int\limits_{V^{out}} \widehat{G}^{ej}(\mathbf{r}, \mathbf{r}') \Delta\sigma^{(c)}(\mathbf{r}') \mathbf{E}^{(c)}(\mathbf{r}') dV, \quad \mathbf{r} \in V^{loc}, \tag{3.15}$$

and eventually solve IE at a finer grid in V^{loc}

$$\mathbf{E}^{(f)}(\mathbf{r}) - \int\limits_{V^{loc}} \widehat{G}^{ej}(\mathbf{r}, \mathbf{r}') \Delta\sigma^{(f)}(\mathbf{r}') \mathbf{E}^{(f)}(\mathbf{r}') dV = \mathbf{E}^0(\mathbf{r}) + \mathbf{E}^{add\,(c)}(\mathbf{r}), \quad \mathbf{r} \in V^{loc}. \tag{3.16}$$

Here, superscripts $^{(c)}$ and $^{(f)}$ mean that coarse and fine spatial resolutions are applied to obtain the corresponding quantities.

Once eq. (3.16) is solved, the electric field, $\mathbf{E}$, can be calculated at any point as

$$\mathbf{E}(\mathbf{r}) = \mathbf{E}^0(\mathbf{r}) + \int\limits_{\mathrm{V}^{\mathrm{loc}}} \widehat{G}^{ej}(\mathbf{r}, \mathbf{r}')\Delta\sigma^{(f)}(\mathbf{r}')\mathbf{E}^{(f)}(\mathbf{r}')d\mathrm{V} + \mathbf{E}^{add\,(c)}(\mathbf{r}), \quad \mathbf{r} \in \mathbf{R}^3, \qquad (3.17)$$

where

$$\mathbf{E}^{add\,(c)}(\mathbf{r}) = \int\limits_{\mathrm{V}^{\mathrm{out}}} \widehat{G}^{ej}(\mathbf{r}, \mathbf{r}')\Delta\sigma^{(c)}(\mathbf{r}')\mathbf{E}^{(c)}(\mathbf{r}')d\mathrm{V}, \quad \mathbf{r} \in \mathbf{R}^3. \qquad (3.18)$$

Note that the nested approach is discussed above in a two-step version for the sake of simplicity; one can, however, apply it recursively by exploiting a sequence of local domains $\mathrm{V}_1^{\mathrm{loc}} \subset \mathrm{V}_2^{\mathrm{loc}} \subset \ldots \mathrm{V}$. Later in this chapter, I will present the results of multi-step realization of the approach.

As evident, the nested approach requires solving IE numerically which is done by means of the Galerkin method. An outline of the method as applied to this problem is presented in the next section; the detailed description can be found in Kruglyakov & Bloshanskaya (2017) and Kruglyakov & Kuvshinov (2018).

3.2.3   Galerkin method in a nutshell

Let $\mathcal{L}_2[\mathrm{V}]$ be a vector Hilbert functional space equipped with the dot product

$$(\mathbf{W}, \mathbf{U}) = \int\limits_{\mathrm{V}} \left(W_x(\mathbf{r})\overline{U}_x(\mathbf{r}) + W_y(\mathbf{r})\overline{U}_y(\mathbf{r}) + W_z(\mathbf{r})\overline{U}_z(\mathbf{r}) \right) d\mathrm{V}, \qquad (3.19)$$

where $\overline{U}$ denotes the complex conjugation of U. Let the set of vector real-valued functions $\boldsymbol{\Psi}_n$, $n = 1, 2, \ldots, N$ form the orthonormal basis in $\mathcal{L}_2[\mathrm{V}]$. Then, denote the linear span of this basis as Q^N and define the projection operator $\mathrm{P_N}$ from $\mathcal{L}_2[\mathrm{V}]$ to Q^N as

$$\mathbf{W}^N = \mathrm{P_N}\,\mathbf{W} = \sum_{n=1}^{N} a_n \boldsymbol{\Psi}_n, \quad \mathbf{W} \in \mathcal{L}_2[\mathrm{V}], \quad \mathbf{W}^N \in Q^N, \qquad (3.20)$$

where

$$a_n = (\mathbf{W}, \boldsymbol{\Psi}_n). \qquad (3.21)$$

The Galerkin method as applied to eq. (3.9) is based on an approximation of the

function $\mathbf{E}$ inside V by the function $\mathbf{U} \in Q^N$ which satisfies the equations

$$((I - G_E \Delta\sigma)\, \mathbf{U}, \boldsymbol{\Psi}_n) = (\mathbf{E}^0, \boldsymbol{\Psi}_n), \quad n = 1, 2, \ldots, N, \tag{3.22}$$

where I is the identity operator, and G_E is the integral operator from eq. (3.9). Using the expansion

$$\mathbf{U} = \sum_{n=1}^{N} u_n \boldsymbol{\Psi}_n, \tag{3.23}$$

eq. (3.22) is transformed into the system of linear equations for coefficients u_n

$$u_n - \sum_{m=1}^{N} u_m (G_E \Delta\sigma \boldsymbol{\Psi}_m, \boldsymbol{\Psi}_n) = (\mathbf{E}^0, \boldsymbol{\Psi}_n), \quad n = 1, 2, \ldots, N. \tag{3.24}$$

After solving the system (3.24) (see Kruglyakov & Bloshanskaya (2017) and Kruglyakov & Kuvshinov (2018) for details of efficient numerical implementation), one substitutes $\mathbf{U}$ instead of $\mathbf{E}$ into the integrands in eq. (3.7) to obtain the (approximation of) electric field, $\widetilde{\mathbf{E}}$, at any point as

$$\widetilde{\mathbf{E}}(\mathbf{r}) = \mathbf{E}^0(\mathbf{r}) + \sum_{n=1}^{N} u_n \int_V \widehat{G}^{ej}(\mathbf{r}, \mathbf{r}') \Delta\sigma(\mathbf{r}') \boldsymbol{\Psi}_n(\mathbf{r}')\, dV', \quad \mathbf{r} \in \mathbf{R}^3. \tag{3.25}$$

The system matrix in eq. (3.24) is dense. Thus, as I mentioned above, probably the only way to solve it efficiently when N is large is to use the basis $\{\boldsymbol{\Psi}_n\}$ which allows for exploiting the convolution properties (3.10). Following Kruglyakov & Kuvshinov (2018), I use the piece-wise polynomial basis which is described in Appendix B.2.

3.3   Implementation details

3.3.1   NIE discretization

Let V be divided into N_c rectangular volume cells, that is

$$V = \bigcup_{n=1}^{N_c} V_n^{(c)}, \tag{3.26}$$

and let V^{loc} be divided into N_f rectangular volume cells, that is

$$V^{\mathrm{loc}} = \bigcup_{n=1}^{N_f} V_n^{(f),\,\mathrm{loc}}. \tag{3.27}$$

Assume that these cells are uniform in lateral directions and the size of $V_n^{(f),\,\mathrm{loc}}$ is smaller than that of $V_n^{(c)}$. Also, assume that conductivity distributions in both domains are piece-wise constant functions.

Let further $\left\{ \boldsymbol{\Psi}_{n,k}^{(c)} \right\}$, $n = 1, 2, \ldots, N_c$, $k = 1, 2, \ldots, K_c$ and $\left\{ \boldsymbol{\Psi}_{n,k}^{(f),\,\mathrm{loc}} \right\}$, $n = 1, 2, \ldots, N_f$, $k = 1, 2, \ldots, K_f$ be the piece-wise polynomial bases in V and V^{loc}, respectively (see Appendix B.2 for details). In this section (and in the appendices), the double index n, k for basis functions are used to stress the fact that

$$
\begin{aligned}
\mathrm{supp}\,\boldsymbol{\Psi}_{n,k}^{(c)} &= V_n^{(c)} \quad n = 1, 2, \ldots, N_c, \ k = 1, 2, \ldots, K_c, \\
\mathrm{supp}\,\boldsymbol{\Psi}_{m,l}^{(f),\,\mathrm{loc}} &= V_m^{(f),\,\mathrm{loc}} \quad m = 1, 2, \ldots, N_f, \quad l = 1, 2, \ldots, K_f.
\end{aligned}
\tag{3.28}
$$

Thus, the first index refers to the space localization of the basis functions, whereas the second one is used to distinguish the basis functions which share the same support.

Then, the electric fields in V and V^{loc} can be expressed as

$$\mathbf{E}^{(c)}(\mathbf{r}) = \sum_{n=1}^{N_c} \sum_{k=1}^{K_c} u_{n,k}^{(c)} \boldsymbol{\Psi}_{n,k}^{(c)}(\mathbf{r}), \quad \mathbf{r} \in V, \tag{3.29}$$

$$\mathbf{E}^{(f)}(\mathbf{r}) = \sum_{n=1}^{N_f} \sum_{k=1}^{K_f} u_{n,k}^{(f),\,\mathrm{loc}} \boldsymbol{\Psi}_{n,k}^{(f),\,\mathrm{loc}}(\mathbf{r}), \quad \mathbf{r} \in V^{\mathrm{loc}}. \tag{3.30}$$

Using the formalism discussed in the previous section and exploiting representation (3.29), eq. (3.14) is transformed into the system of linear equations for coefficients $u_{n,k}^{(c)}$

$$u_{n,k}^{(c)} - \sum_{m=1}^{N_c} \sum_{l=1}^{K_c} u_{m,l}^{(c)} \left(G_{\mathrm{E}}\, \Delta\sigma^{(c)} \boldsymbol{\Psi}_{m,l}^{(c)}, \boldsymbol{\Psi}_{n,k}^{(c)} \right) = \left(\mathbf{E}^0, \boldsymbol{\Psi}_{n,k}^{(c)} \right), \tag{3.31}$$

$$n = 1, 2, \ldots, N_c, \quad k = 1, 2, \ldots, K_c.$$

Similarly, using representation (3.30), eq. (3.16) is transformed into the system for

coefficients $u_{n,k}^{(f)}$

$$u_{n,k}^{(f),\,\mathrm{loc}} - \sum_{m=1}^{N_f} \sum_{l=1}^{K_f} u_{m,l}^{(f),\,\mathrm{loc}} \left(\mathrm{G_E}\, \Delta\sigma^{(f)} \boldsymbol{\Psi}_{m,l}^{(f),\,\mathrm{loc}}, \boldsymbol{\Psi}_{n,k}^{(f),\,\mathrm{loc}} \right) = \left(\mathbf{E}^0, \boldsymbol{\Psi}_{n,k}^{(f),\,\mathrm{loc}} \right) + \left(\mathbf{E}^{add\,(c)}, \boldsymbol{\Psi}_{n,k}^{(f),\,\mathrm{loc}} \right),$$

$$n = 1, 2, \ldots, N_f, \quad k = 1, 2, \ldots, K_f. \tag{3.32}$$

Comparing eqs (3.31) and (3.32), one can notice that the second term in the right-hand side (RHS) of the equation is a new term. According to eqs (3.15) and (3.29), one writes

$$\mathbf{E}^{add\,(c)}(\mathbf{r}) = \sum_{\mathrm{V}_m^{(c)} \subset \mathrm{V}^{out}} \sum_{l=1}^{K_c} \Delta\sigma_m^{(c)} u_{m,l}^{(c)} \int_{\mathrm{V}_m^{(c)}} \widehat{G}^{ej}(\mathbf{r}, \mathbf{r}') \boldsymbol{\Psi}_{m,l}^{(c)}(\mathbf{r}') d\mathrm{V}_m^{(c)}, \quad \mathbf{r} \in \mathrm{V}^{\mathrm{loc}}. \tag{3.33}$$

Then, the second term of the RHS in eq. (3.32) becomes

$$\left(\mathbf{E}^{add\,(c)}, \boldsymbol{\Psi}_{n,k}^{(f),\,\mathrm{loc}} \right) = \sum_{\mathrm{V}_m^{(c)} \subset \mathrm{V}^{out}} \sum_{l=1}^{K_c} \Delta\sigma_m^{(c)} u_{m,l}^{(c)} \int_{\mathrm{V}_n^{(f),\mathrm{loc}}} \int_{\mathrm{V}_m^{(c)}} \boldsymbol{\Psi}_{n,k}^{(f),\,\mathrm{loc}}(\mathbf{r}) \widehat{G}^{ej}(\mathbf{r}, \mathbf{r}') \boldsymbol{\Psi}_{m,l}^{(c)}(\mathbf{r}') d\mathrm{V}_m^{(c)}\, d\mathrm{V}_n^{(f),\mathrm{loc}},$$

$$n = 1, 2, \ldots, N_f, \quad k = 1, 2, \ldots, K_f. \tag{3.34}$$

Now, recall that the sizes of $\mathrm{V}_m^{(c)}$ and $\mathrm{V}_n^{(f),\,\mathrm{loc}}$ are different due to the main idea of the nested approach. Thus, in order to calculate the RHS of (3.34), one has to compute $\mathcal{O}(N_c N_f)$ integrals. This could be computationally very expensive provided N_c and N_f are large. I discuss below how this challenge can be mitigated.

The simplest way to address the problem is to approximate $\mathbf{E}^{add\,(c)}(\mathbf{r})$ in $\mathrm{V}^{\mathrm{loc}}$ as

$$\mathbf{E}^{add\,(c)}(\mathbf{r}) \approx \mathbf{E}_{(c)}^{add\,(c)}(\mathbf{r}) = P_{N^{(c)}} \mathbf{E}^{add\,(c)}(\mathbf{r}) = \sum_{n=1}^{N_c} \sum_{k=1}^{K_c} u_{n,k}^{add\,(c)} \boldsymbol{\Psi}_{n,k}^{(c)}(\mathbf{r}), \quad \mathbf{r} \in \mathrm{V}^{\mathrm{loc}}, \tag{3.35}$$

where the coefficients $u_{n,k}^{add\,(c)}$ are calculated – using eq. (3.33) – as

$$
\begin{aligned}
u_{n,k}^{add\,(c)} &= \left(\mathbf{E}_{(c)}^{add\,(c)}, \mathbf{\Psi}_{n,k}^{(c)} \right) \\
&= \sum_{V_m^{(c)} \subset V^{\mathrm{out}}} \sum_{l=1}^{K_c} \Delta\sigma_m^{(c)} u_{m,l}^{(c)} \int\limits_{V_n^{(c)}} \int\limits_{V_m^{(c)}} \mathbf{\Psi}_{n,k}^{(c)}(\mathbf{r}) \widehat{G}^{ej}(\mathbf{r}, \mathbf{r}') \mathbf{\Psi}_{m,l}^{(c)}(\mathbf{r}') dV_m^{(c)} \, dV_n^{(c)}, \qquad (3.36) \\
&\qquad V_n^{(c)} \subset V^{\mathrm{loc}}, k = 1, 2, \ldots, K_c.
\end{aligned}
$$

Since in the above equation only the coarse discretization is involved (which we assume to be laterally-uniform), the coefficients $u_n^{add\,(c)}$ can be efficiently computed by using 2-D FFT. Once these coefficients are calculated, the second term in the RHS of eq. (3.32) is approximated as

$$
\left(\mathbf{E}^{add\,(c)}, \mathbf{\Psi}_{n,k}^{(f),\,\mathrm{loc}} \right) \approx \sum_{V_m^{(c)} \subset V^{\mathrm{loc}}} \sum_{l=1}^{K_c} u_{m,l}^{add\,(c)} \int\limits_{V_n^{(f),\mathrm{loc}}} \mathbf{\Psi}_{n,k}^{(f),\,\mathrm{loc}}(\mathbf{r}) \mathbf{\Psi}_{m,l}^{(c)}(\mathbf{r}) dV_n^{(f),\mathrm{loc}}, \tag{3.37}
$$

$$
n = 1, 2, \ldots, N_f, \quad k = 1, 2, \ldots, K_f.
$$

Note that integrals in the latter equation (which are just the projection coefficients from one basis to another) can be computed analytically (see Appendix B.3).

However, the numerical experiments (see Section 3.4.1) show that such an approach to calculating $\left(\mathbf{E}^{add\,(c)}, \mathbf{\Psi}_n^{(f),\,\mathrm{loc}} \right)$ leads to large artifacts in the IE solution in V^{loc}. These artifacts come from the following phenomenon. As seen, for instance, from eq. (3.15), $\mathbf{E}^{add\,(c)}$ is a field induced by a current occupied the domain V^{out}. This, in particular, means that $\mathbf{E}^{add\,(c)}$ changes abruptly when $\mathbf{r}$ is close to $\mathbf{r}'$, i.e. near the boundaries of the domain V^{loc}. This is due to the "singular" behavior of tensor $\widehat{G}^{ej}$ when $\mathbf{r}$ tends to $\mathbf{r}'$. Hence, the "coarse" approximation of $\mathbf{E}^{add\,(c)}$ by $\mathbf{E}_{(c)}^{add\,(c)}$ introduces substantial errors in $\mathbf{E}^{add\,(c)}$, which in turn leads to the errors in the final results. Below, I explain the numerical recipe which allows us to overcome this problems, while still exploiting the (efficient) scheme of estimating $\mathbf{E}^{add\,(c)}$ described above.

3.3.2 Rim domain concept (RDC)

Let me introduce domain $V^{\mathrm{loc}+}$ such that $V^{\mathrm{loc}} \subset V^{\mathrm{loc}+} \subset V$, as shown in Figure 3.2. I denote this domain as $V^{\mathrm{loc}+}$ to emphasize the fact that it is insignificantly larger than
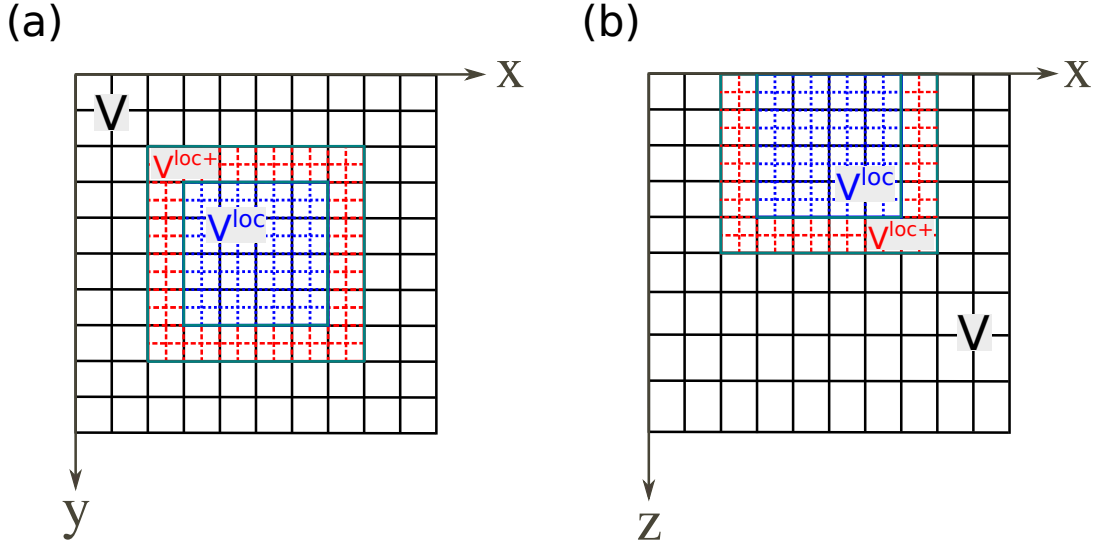
Figure 3.2: Illustration of the rim domain concept, which is introduced to avoid the boundary effect in the nested IE approach: (a) a top view, and (b) the cross section. V^{loc+} comprises V^{loc} and an additional "narrow" rim (a few coarse grid cells in width), i.e. $V^{loc+} = V^{loc} \bigcup V^{rim}$. See details in the text.

V^{loc}. How large this domain has to be taken will be explained below. I also denote as V^{rim} the complement of V^{loc} to V^{loc+}, i.e.

$$V^{rim} = V^{loc+} \setminus V^{loc}, \tag{3.38}$$

and denote as V^{ext} the complement of V^{loc+} to V, i.e.

$$V^{ext} = V \setminus V^{loc+}. \tag{3.39}$$

Then, $\mathbf{E}^{add\,(c)}$ can be written as

$$\mathbf{E}^{add\,(c)}(\mathbf{r}) = \mathbf{E}^{add\,(c)}_{ext}(\mathbf{r}) + \mathbf{E}^{add\,(c)}_{rim}(\mathbf{r}), \quad \mathbf{r} \in V^{loc}, \tag{3.40}$$

where, in accordance with (3.15), $\mathbf{E}^{add\,(c)}_{ext}$ and $\mathbf{E}^{add\,(c)}_{rim}$ read

$$\mathbf{E}^{add\,(c)}_{ext}(\mathbf{r}) = \int_{V^{ext}} \widehat{G}^{ej}(\mathbf{r}, \mathbf{r}') \Delta\sigma^{(c)}(\mathbf{r}') \mathbf{E}^{(c)}(\mathbf{r}') dV, \quad \mathbf{r} \in V^{loc}, \tag{3.41}$$

$$\mathbf{E}^{add\,(c)}_{rim}(\mathbf{r}) = \int_{V^{rim}} \widehat{G}^{ej}(\mathbf{r}, \mathbf{r}') \Delta\sigma^{(c)}(\mathbf{r}') \mathbf{E}^{(c)}(\mathbf{r}') dV, \quad \mathbf{r} \in V^{loc}. \tag{3.42}$$

The idea behind splitting the integral over domain V^{out} onto integrals over "rim domain" V^{rim} and "external" domain V^{ext} is as follows. If the distance between boundaries of the V^{ext} and V^{loc} (i.e. distance between $\mathbf{r}$ and $\mathbf{r}'$ in integral (3.41)) is large enough, then function $\mathbf{E}_{ext}^{add\,(c)}(\mathbf{r}), \mathbf{r} \in V^{loc}$ can be approximated by using the "coarse" basis $\mathbf{\Psi}^{(c)}$ as described above, because in this case $\mathbf{E}_{ext}^{add\,(c)}(\mathbf{r})$ does not undergo abrupt changes. Note, that the numerical experiments (to be discussed in the next section) demonstrate that a "large enough" distance between boundaries of V^{ext} and V^{loc} (i.e. the distance between external boundaries of V^{loc+} and V^{loc}) is achieved when they are separated by one or two coarse cells in the corresponding direction.

Ultimately, one has to solve the system (3.32) and thus calculate

$$\left(\mathbf{E}^{add\,(c)}, \mathbf{\Psi}_{n,k}^{(f),\,loc} \right) = \left(\mathbf{E}_{ext}^{add\,(c)}, \mathbf{\Psi}_{n,k}^{(f),\,loc} \right) + \left(\mathbf{E}_{rim}^{add\,(c)}, \mathbf{\Psi}_{n,k}^{(f),\,loc} \right),$$

$$n = 1, 2, \ldots, N_f, \quad k = 1, 2, \ldots, K_f. \tag{3.43}$$

As I already mentioned above, to calculate the first term in the RHS of the latter equation, I make use of eq. (3.37), namely

$$\left(\mathbf{E}_{ext}^{add\,(c)}, \mathbf{\Psi}_{n,k}^{(f),\,loc} \right) \approx \sum_{V_m^{(c)} \subset V^{ext}} \sum_{l=1}^{K_c} u_{m,l}^{add\,(c)} \int_{V_n^{(f),\,loc}} \mathbf{\Psi}_{n,k}^{(f),\,loc}(\mathbf{r}) \mathbf{\Psi}_{m,l}^{(c)}(\mathbf{r}) dV_n^{(f),\,loc},$$

$$n = 1, 2, ..., N_f, \quad k = 1, 2, \ldots, K_f. \tag{3.44}$$

To calculate the second term in the RHS of (3.43), I propagate our "fine" basis $\left\{ \mathbf{\Psi}_{n,k}^{(f),\,loc} \right\}$ from domain V^{loc} to domain V^{loc+}. This can be done by using the same (fine) discretization in V^{loc+} as in V^{loc} and taking into account that local basis functions are the same for different cells (see Appendix B.2). Now, one can project $\mathbf{E}^{(c)}(\mathbf{r}), \mathbf{r} \in V^{loc+}$ from the coarse $\left\{ \mathbf{\Psi}_{n,k}^{(c)} \right\}$ to the fine $\left\{ \mathbf{\Psi}_{m,l}^{(f),\,loc} \right\}$ basis (see Appendix B.3 for details) as

$$\mathbf{E}^{(c)}(\mathbf{r}) \approx \sum_{n=1}^{N_{loc+}} \sum_{k=1}^{K_f} u_{n,k}^{loc+} \mathbf{\Psi}_{n,k}^{(f),\,loc}(\mathbf{r}), \tag{3.45}$$

substitute it into eq. (3.42), and then into the second term of eq. (3.43) thus obtaining

$$
\left(\mathbf{E}_{rim}^{add\,(c)}, \mathbf{\Psi}_{n,k}^{(f),\,\mathrm{loc}}\right)
$$

$$
\approx \sum_{\mathrm{V}_m^{(f),\,\mathrm{loc}} \subset \mathrm{V}^{\mathrm{rim}}} \sum_{l=1}^{K_f} \Delta\sigma_m^{(f)} u_{m,l}^{loc+} \int\limits_{\mathrm{V}_n^{(f),\,\mathrm{loc}}} \int\limits_{\mathrm{V}_m^{(f),\,\mathrm{loc}}} \mathbf{\Psi}_{n,k}^{(f),\,\mathrm{loc}}(\mathbf{r})\widehat{G}^{ej}(\mathbf{r},\mathbf{r}')\mathbf{\Psi}_{m,l}^{(f),\,\mathrm{loc}}(\mathbf{r}')d\mathrm{V}_m^{(f),\,\mathrm{loc}}\,d\mathrm{V}_n^{(f),\,\mathrm{loc}},
$$

$$
n = 1, 2, ..., N_f, \quad k = 1, 2, \ldots, K_f. \tag{3.46}
$$

One can see that to obtain the RHS of the latter equation, one has to compute only $\mathcal{O}(N_f)$ integrals, since $\mathrm{V}^{\mathrm{rim}}$ is small compared to $\mathrm{V}^{\mathrm{loc}}$.

3.4   Numerical tests

To verify the developed nested IE tool, I performed the tests in two 3-D conductivity models.

3.4.1   3D-2 model

The first (3D-2) model comes from COMMEMI project (Zhdanov et al., 1997), which is widely used to validate the newly developed EM modeling solvers (Mitsuhata & Uchida, 2004; Ren et al., 2014; Grayver & Bürg, 2014; Kruglyakov et al., 2016; Kruglyakov & Kuvshinov, 2018, among others). The model comprises two – relatively resistive and relatively conductive – blocks embedded in the three-layered background. The side and plane views of the model, as well as the resistivities assigned to the different structures, are shown in Figure 3.3.

The reference ("true") results are computed by using the IE-based solver PGIEM2G developed by Kruglyakov & Kuvshinov (2018) on a "fine grid" in the whole domain V (which is depicted as a black rectangle in Figure 3.3). Three comments are relevant at this point: a) the presented nested IE tool uses the core modules of the PGIEM2G solver; b) the PGIEM2G solver itself was successfully verified against the FEM-based solver by Grayver & Kolev (2015); c) as in Kruglyakov & Kuvshinov (2018) (where the same model was also used for the testing purpose), in all model experiments of this section the same (3rd) order of polynomial basis was used in both lateral and vertical
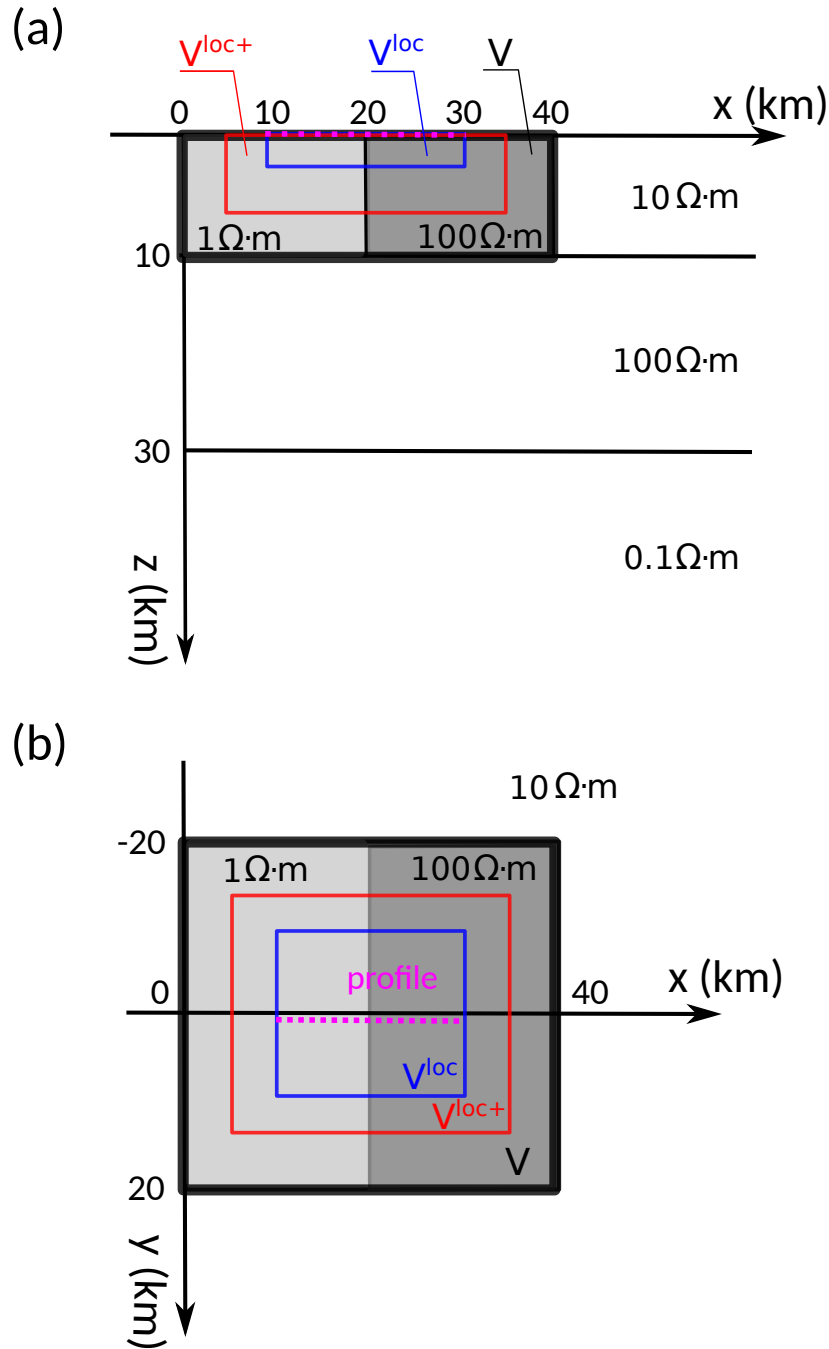
Figure 3.3: The 3D-2 model from the COMMEMI project (Zhdanov et al., 1997): (a) a side view of the model and (b) a plan view. V represents the whole modeling domain, V^{loc} denotes the local domain, and domain V^{loc+} comprises V^{loc} and the additional (narrow) rim (of width of a few coarse grid cells), i.e. $V^{loc+} = V^{loc} \bigcup V^{rim}$. Dashed pink line denotes the profile at the Earth's surface at which the modeling results are presented.

directions. Table 3.1 presents the number of cells and their sizes for the reference IE modeling, and for two numerical experiments using the two-step nested IE approach. Note that the goal of these two numerical experiments is two-fold: first, to validate the

nested approach, and second, to show that one indeed has to use the rim domain concept (RDC) in order to obtain the correct results.

For the "nested" computations, I take the central, shallow part of the model V^{loc} as a local domain; it is depicted as a blue rectangle in Figure 3.3. V^{loc} occupies a $20 \times 15 \times 0.5$ km^3 volume. The domain $V^{loc+} \equiv V^{loc} \cup V^{rim}$ is depicted by the red line in Figure 3.3; the rim's width is taken as one coarse cell in y-direction and two coarse cells in both x- and z-directions.

Table 3.1: Number of cells and their sizes for the reference IE calculations, and for the numerical experiments using the two-step nested NIE approach.

	$N_x \times N_y \times N_z$	$dx \times dy$ (km^2)	dz (km)
Reference (conventional) IE (at V)	$64 \times 16 \times 4$	0.625×2.5	$0.5, 0.5, 4, 5$
1st step of NIE (at V)	$16 \times 16 \times 4$	2.5×2.5	$0.5, 0.5, 4, 5$
2nd step of NIE (at V^{loc}, using RDC)	$24 \times 8 \times 3$	1.25×2.5	$0.5, 0.5, 4$
2nd step of NIE (at V^{loc}, not using RDC)	$16 \times 6 \times 1$	1.25×2.5	0.5

The results of the model experiments are summarized in Figures 3.4 - 3.7. The figures present the computed apparent resistivities and phases of MT impedances (Chave & Jones, 2012) at periods of 10 and 1000 sec along the profile shown in Figure 3.3. One can see that the responses calculated by using the nested approach using RDC (red stars) match well with the "true" responses (black line). The relative differences for the off-diagonal apparent resistivities are smaller than $3\,\%$, and the differences in the phases are smaller than 0.25 degree (cf. Figures 3.8 - 3.9).

At the same time, the responses computed by the nested approach, but without considering RDC (blue circles) noticeably differ from the "true" responses (see again Figures 3.4 -3.7). These results clearly demonstrate the importance of using the RDC.

However, invoking the RDC makes the implementation of the nested approach more complicated. In this context, the natural question arises whether one can avoid using the RDC by just increasing the size of the local domain? This seems feasible, especially when the modeler is interested in the results only in the central part of the local domain, i.e. far from its boundaries. Indeed, it is quite obvious that if the local domain is taken large enough, there is no need to use the RDC. However, the usage of a large local domain contradicts the idea of the nested approach, namely, minimization of the computational loads by making the local domain as small as practicable.
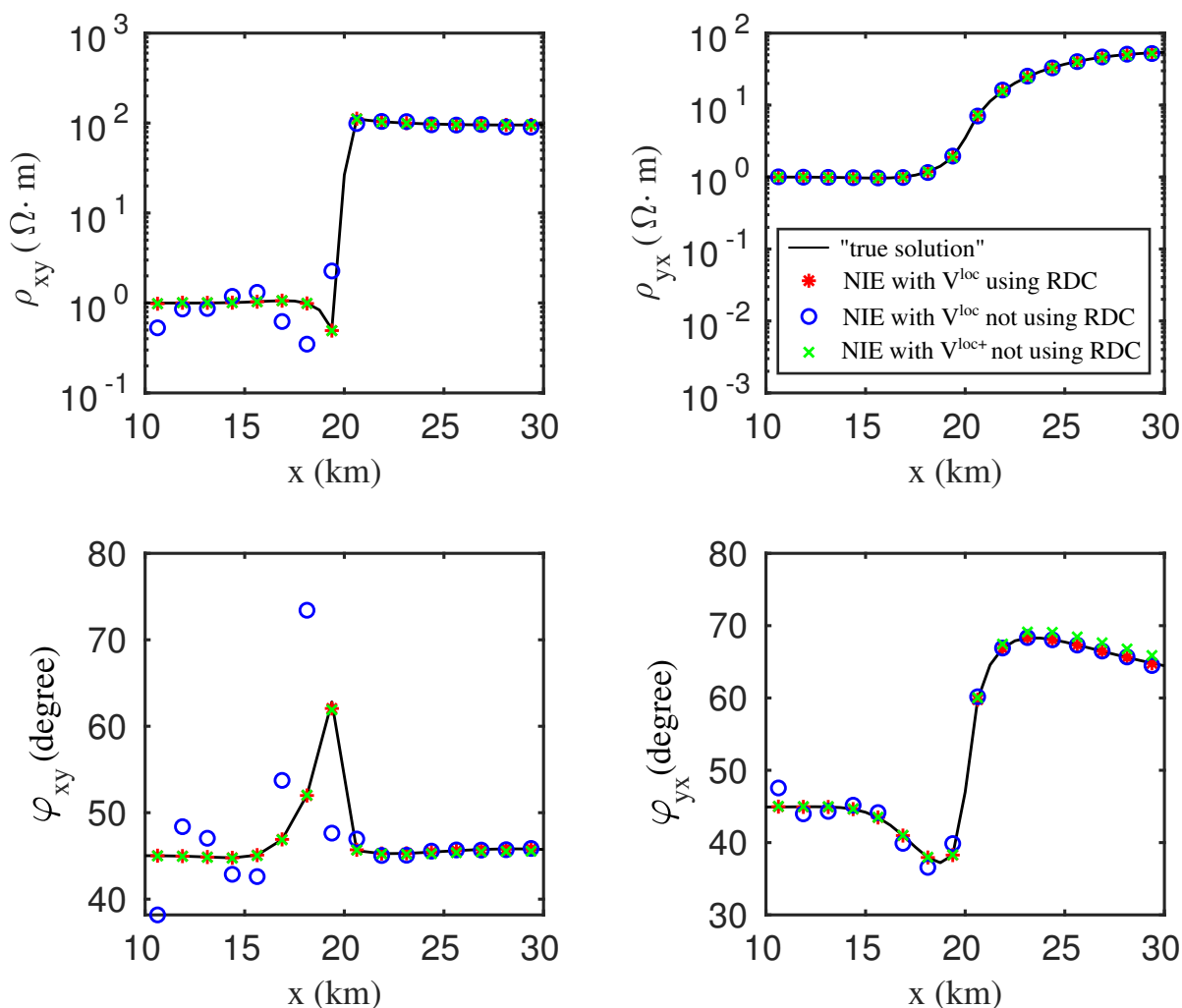
Figure 3.4: Apparent resistivities (ρ_{xy} and ρ_{yx}) and phases (φ_{xy} and φ_{yx}) of MT impedance at the period of 10 sec along the profile shown in Figure 3.3. The results are for the reference modeling and for three scenarios of two-step NIE. See details in the text.

To explore further the importance of using the RDC, I performed the nested modeling in which the local domain is extended to V^{loc+} (and no rim domain is invoked). The results are shown in Figures 3.4 - 3.7 by green crosses. One can see a good agreement of the obtained responses with "true" responses in the off-diagonal components (Figures 3.4 and 3.6). However, the agreement in the diagonal components (Figures 3.5 and 3.7) appeared to be poor.

Next, two model experiments further advocate using the RDC. The first experiment involves three-step nested IE modeling without considering the rim domain. The number of cells and their sizes for the performed computations are listed in Table 3.2. The first-
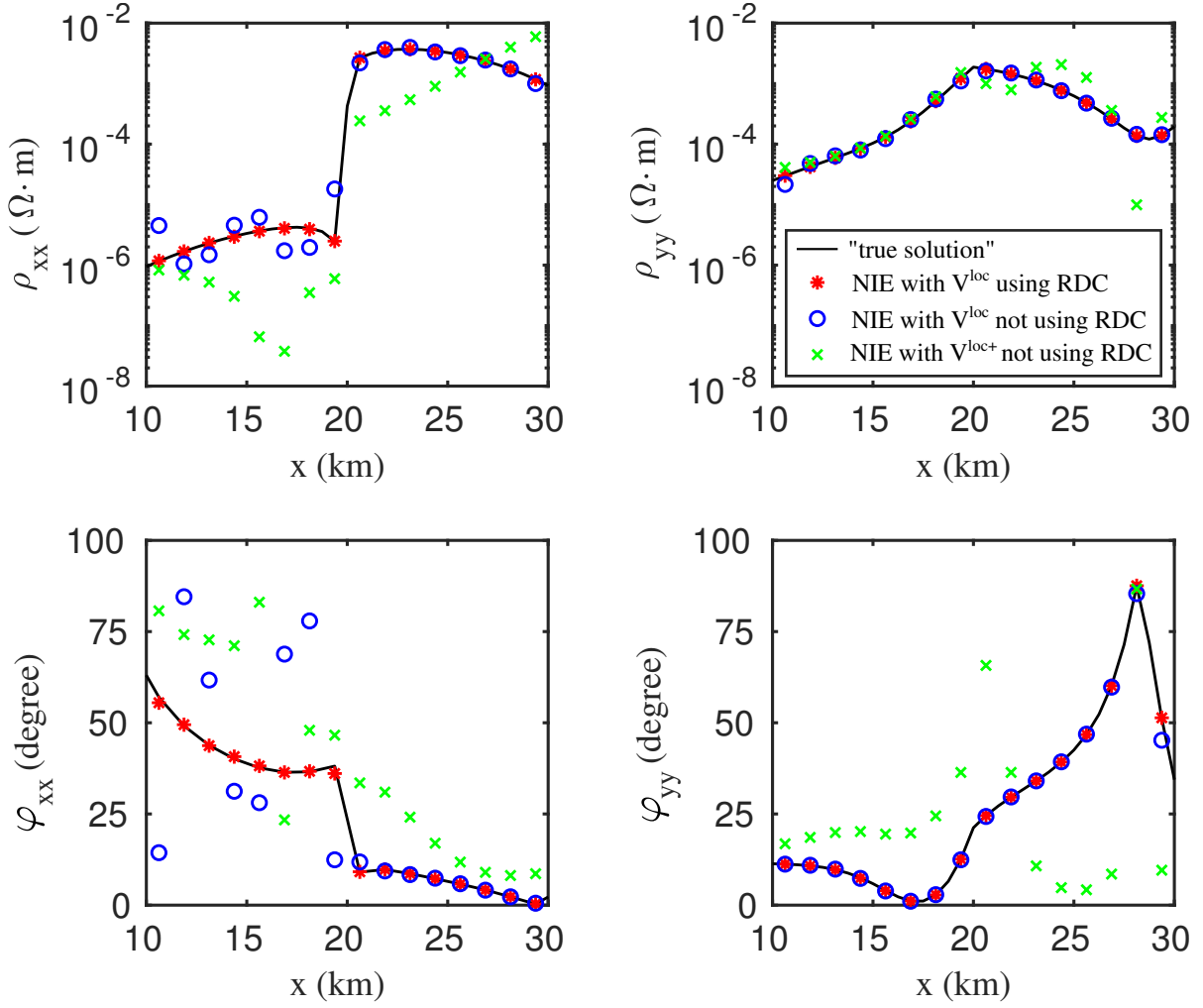
Figure 3.5: As in Figure 3.4, but for apparent resistivities (ρ_{xx} and ρ_{yy}) and phases (φ_{xx} and φ_{yy}).

step IE modeling is the same as that in the two-step implementation discussed above. In the second and the third steps, the regions V^{loc+} and V^{loc} were chosen as the local domains.

Table 3.2: Number of cells and their sizes for the numerical experiment using a three-step NIE approach without invoking RDC.

|	$N_x \times N_y \times N_z$	$dx \times dy$	dz
1st step of NIE (at V)	$16 \times 16 \times 4$	$2.5 \times 2.5 \,\text{km}^2$	$0.5, 0.5, 4, 5\,\text{km}$
2nd step of NIE (at V^{loc+})	$24 \times 8 \times 3$	$1.25 \times 2.5 \,\text{km}^2$	$0.5, 0.5, 4\,\text{km}$
3rd step of NIE (at V^{loc})	$32 \times 6 \times 1$	$0.625 \times 2.5 \,\text{km}^2$	$0.5\,\text{km}$

As is seen from Figure 3.10, the off-diagonal components in the local domain computed at the second-step IE modeling match well with the "true" solutions – as expected,
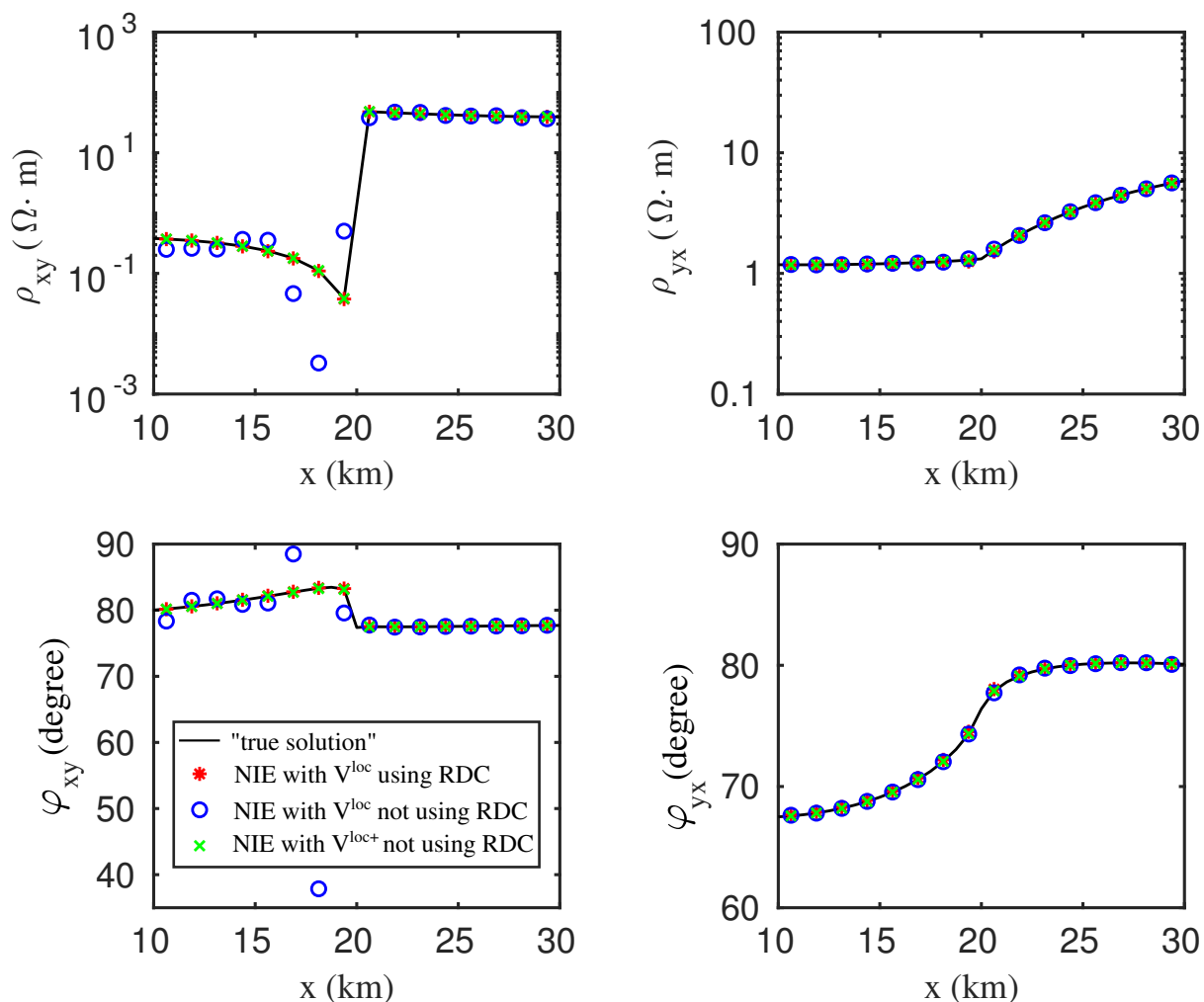
Figure 3.6: As in Figure 3.4, but at the period of 1000 sec.

according to the previous results. However, the third step destroys this agreement for ρ_{xy} and φ_{xy}, especially at the interface of two anomalous blocks and the boundary of the local domain. The reason for this is that the RHS at the third step is an integral over the $V^{loc+} \setminus V^{loc}$ i.e. over the domain where the solution at the second step has the largest errors.

As a final model experiment, I performed the three-step RDC-based nested modeling. At the second step, one coarse cell in the y, z-directions and two coarse cells in the x-direction were considered as the rim domain, while one coarse cell in the y-direction and two coarse cells were considered in the x, z-directions at the third step. The lateral discretization used in this experiment is exactly the same as the one in the three-step nested modeling without considering RDC. Very good agreement between the responses
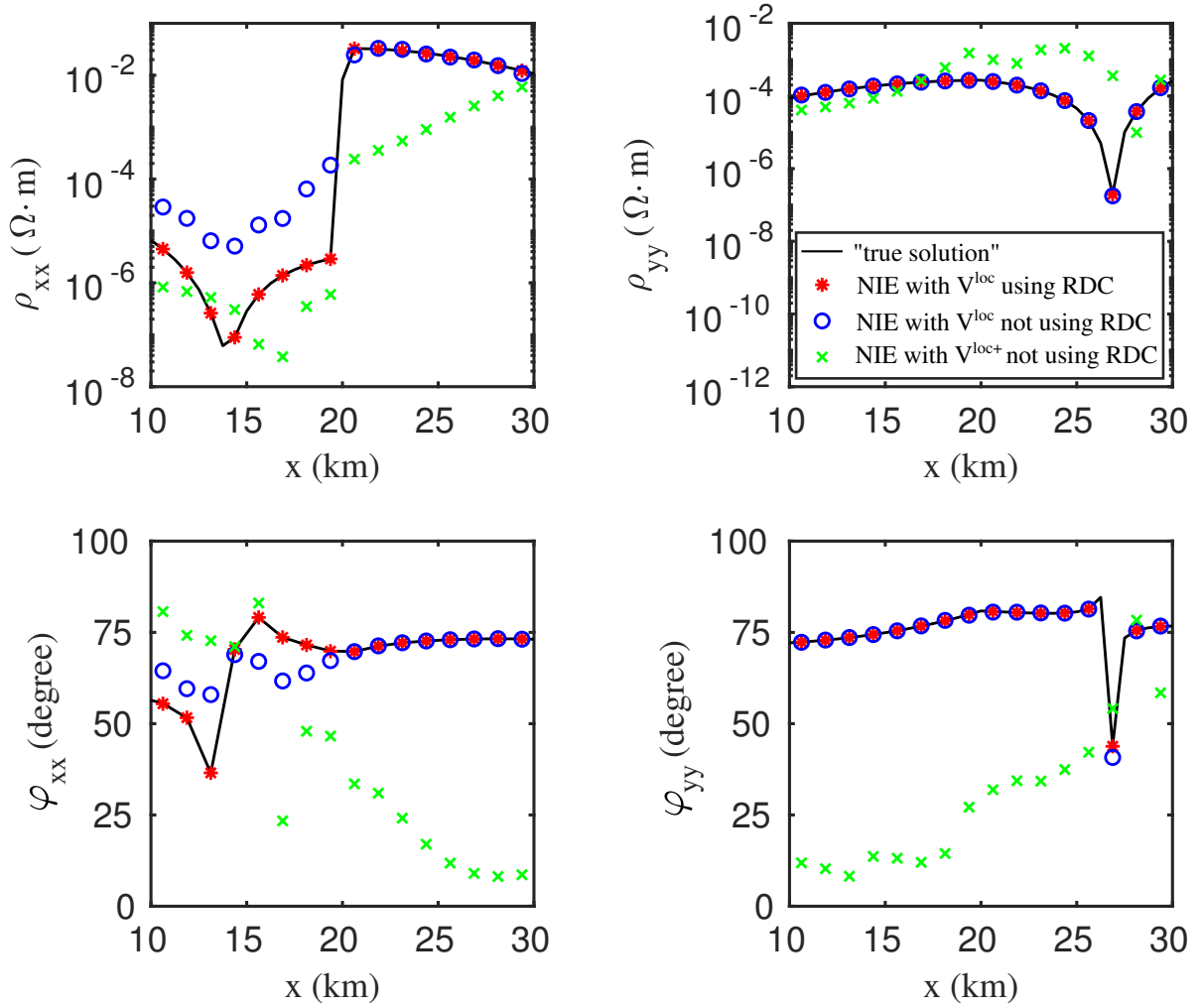
Figure 3.7: As in Figure 3.5, but at the period of 1000 sec.

based on the three-step nested IE (red stars in the Figure 3.10) and the "true" responses
is now observed. This demonstrates again that the usage of the RDC is essential for
obtaining accurate results in the local domain, especially for the multi-step realization
of the nested IE approach.

3.4.2 Realistic conductivity model around Gan geomagnetic observatory

The second test aims to illustrate the ability of the nested tool to deal with the realistic conductivity models, where both the distant non-uniform structures and the local
bathymetry have to be taken into account. The previous study (Chen et al., 2020)
shows that the responses of islands at periods longer than a few days (Banks, 1969) are
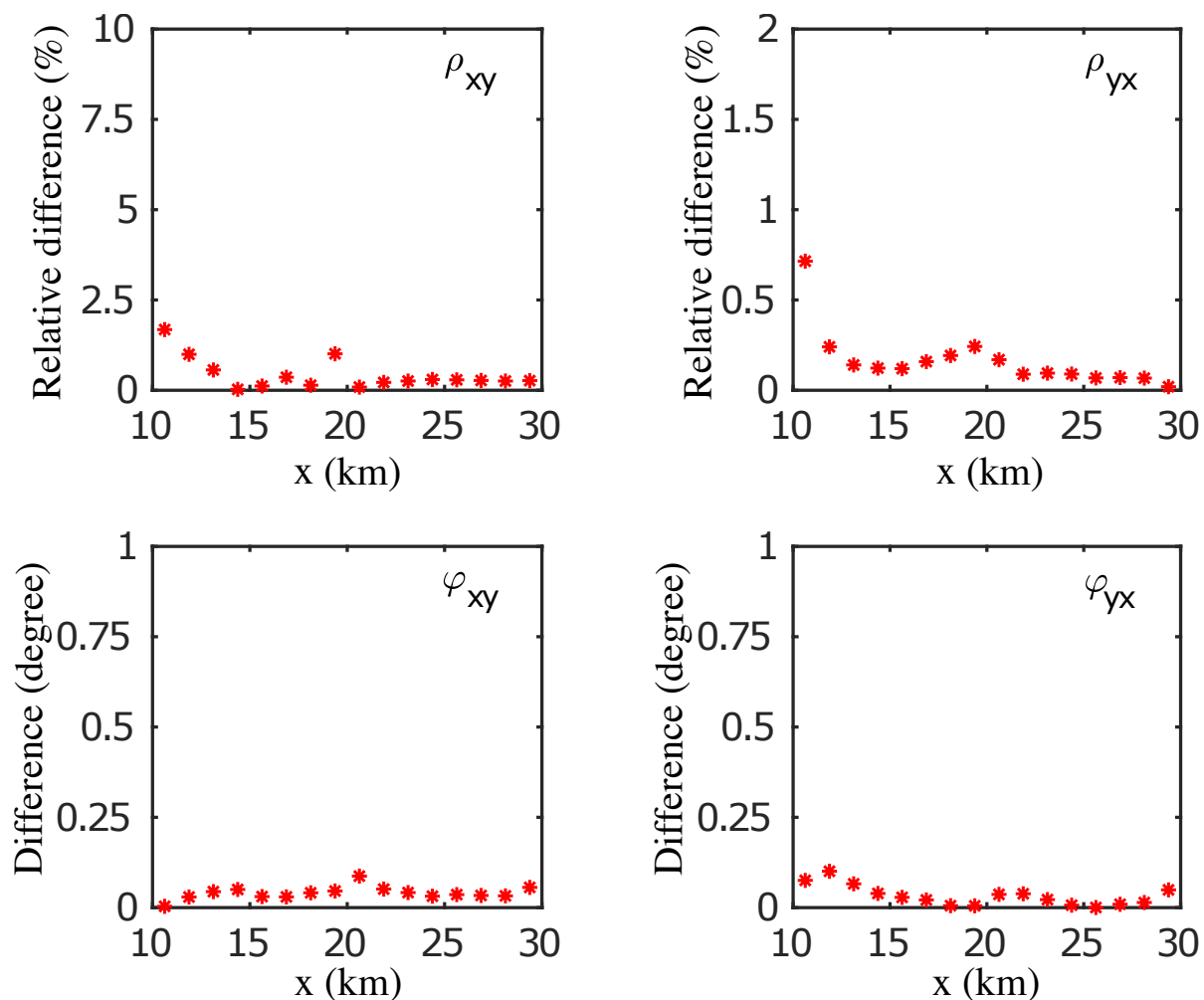
Figure 3.8: Top row: relative differences between "true" off-diagonal apparent resistivities and those calculated using NIE. Bottom row: differences in the off-diagonal phases of impedance. The results are for a period of 10 sec.

strongly affected by the ocean induction effect, which can be accounted for by using the high-resolution bathymetry and a nested approach. Here, I look at the shorter-period island responses, namely, magnetic MT transfer functions (tippers) that relate the vertical magnetic field, H_z, with the horizontal magnetic field, $\mathbf{H}_\tau$

$$H_z(\mathbf{r}_s, \omega) = T(\mathbf{r}_s, \omega)\mathbf{H}_\tau(\mathbf{r}_s, \omega), \quad T = [T_{zx} \quad T_{zy}]. \tag{3.47}$$

As an island geomagnetic observatory, I consider the observatory Gan located at the southernmost island of the Maldives archipelago (longitude: 73.1537° E; latitude: 0.6946° S; INTERMAGNET code: GAN). The realistic conductivity model consists of a 1-D Earth's conductivity overlaid by an oceanic layer with a 3-D conductivity distribu-
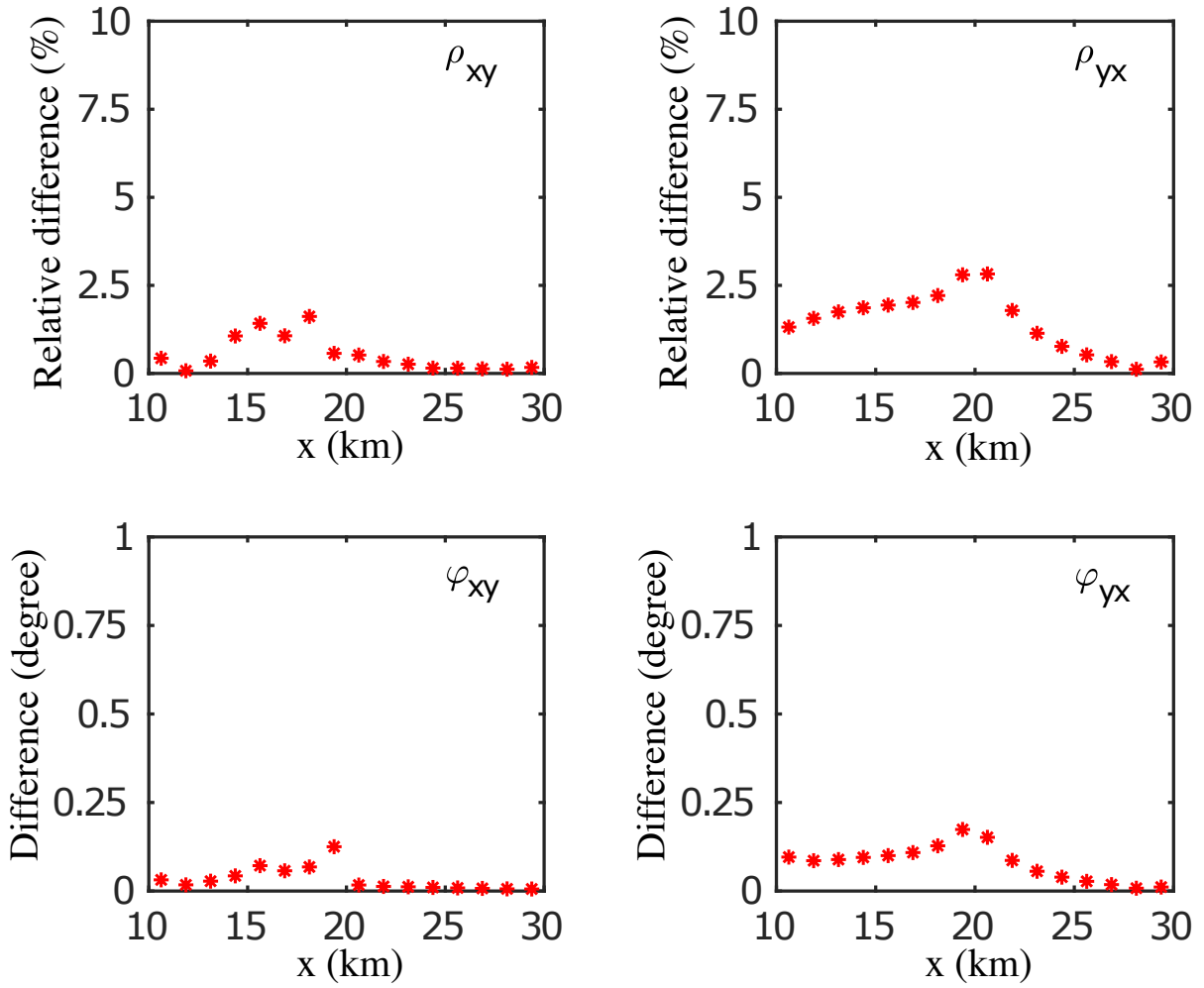
Figure 3.9: As in Figure 3.8, but for the period of 1000 sec.

tion. The 1-D conductivity (shown in Figure 3.11a) is taken from Morschhauser et al. (2019), whereas the 3-D conductivity distribution is constructed by using the $30'' \times 30''$ bathymetry data from the General Bathymetry Chart of the Oceans (GEBCO; Becker et al. (2009)); note that $30'' \times 30''$ (spherical) resolution corresponds to $\approx 0.9 \times 0.9$ km² resolution at the equator. Laterally, the domain V is confined to $70.66° - 75.66°$ longitudes and $-3.20° - 1.80°$ latitudes. Bathymetry in this region is shown in Figure 3.11b. In order to obtain the bathymetry distribution in Cartesian coordinates, the Mercator map projection as described in Snyder (1982) is employed. Eventually, the modeling domain V occupies the volume of $555 \times 555 \times 5.5$ $(x \times y \times z)$ km³. Furthermore, the obtained bathymetry is used for the construction of 3-D conductivity distribution in the model. I also used a (much) higher-resolution coastline database (of resolution of $\approx 60 \times 60$ m² in GAN region) from the Global Self-consistent, Hierarchical, High-resolution Geography
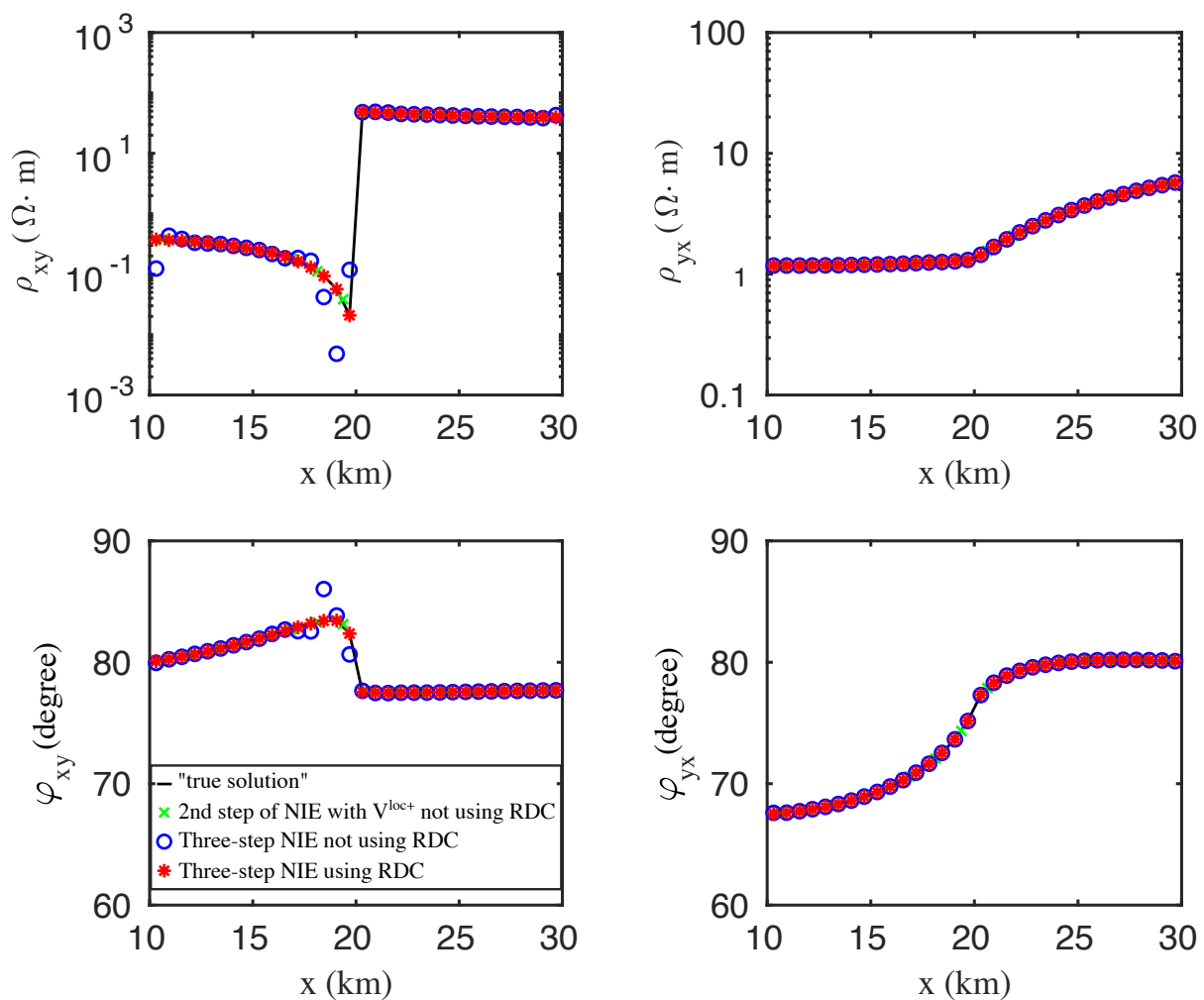
Figure 3.10: Apparent resistivities (ρ_{xy} and ρ_{yx}) and phases (φ_{xy} and φ_{yx}) of MT impedance at the period of 1000 sec along the profile shown in Figure 3.3. The results are for the reference modeling and for three scenarios of three-step NIE. See details in the text.

Database (GSHHG) (Wessel & Smith, 1996; Bohlander & Scambos, 2007) in order to correct the bathymetry-based model when constructing a high resolution 3-D conductivity model in the local domain. The conductivities of seawater are obtained from the World Ocean Atlas at the $1° \times 1°$ resolution and are available in the supplementary material of Grayver et al. (2016). The conductivity within the cells that contain the land-seawater interface is computed as the depth-integrated average. Gan island is very flat, thus the topography is not included in the model. The constructed 3-D conductivity model is shown in Figure 3.12.

In this model experiment, I compare tippers computed using the NIE and FEM solvers. The FEM results are from Morschhauser et al. (2019); in that paper the authors

(a)

(b)
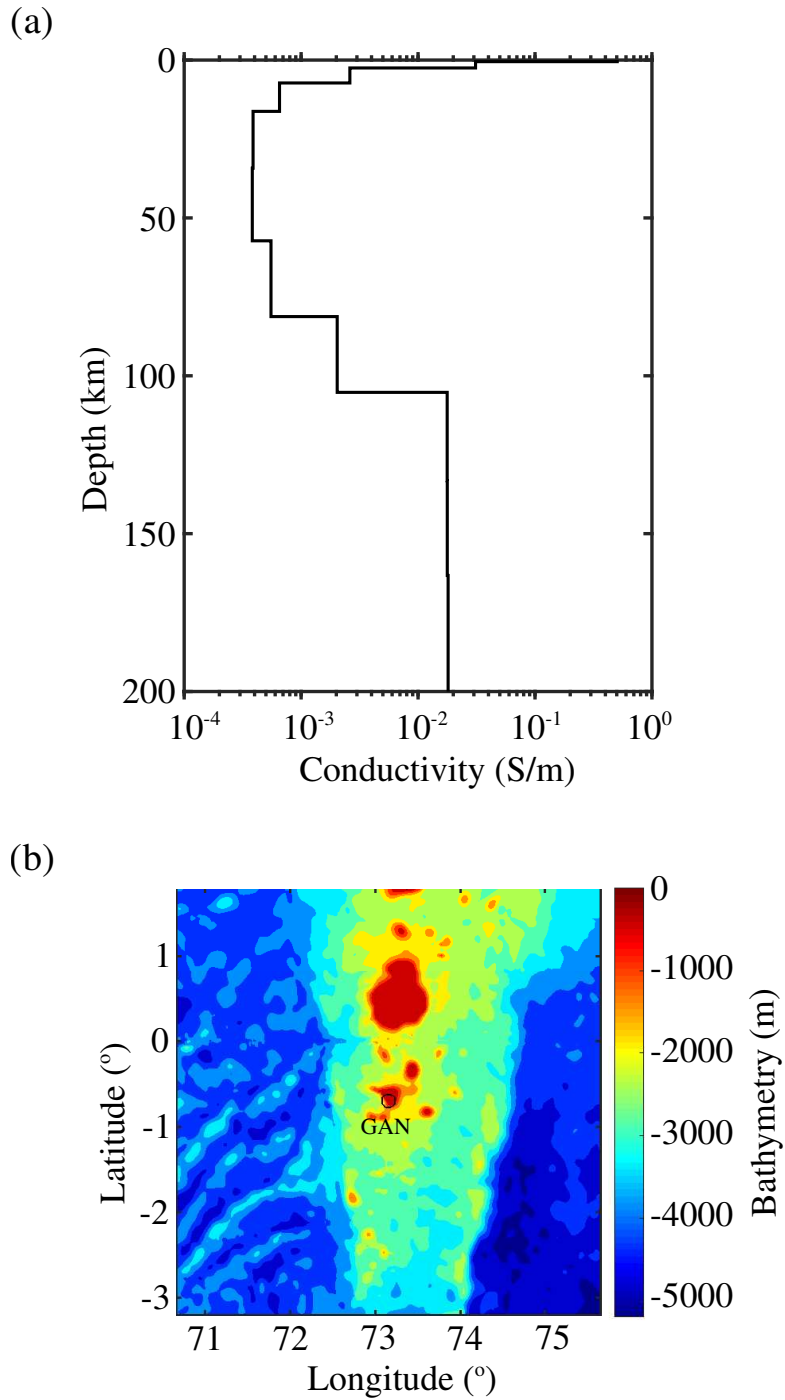
Figure 3.11: (a) 1-D conductivity profile beneath GAN observatory; (b) Bathymetry distribution in the vicinity of the GAN geomagnetic observatory.

used the FEM solver of Grayver & Kolev (2015) to model the GAN tippers.

NIE modeling was performed using the three-step scheme. Table 3.3 summarizes the details (number and sizes of cells) for each NIE step. Note here that the highest NIE resolution ($61.7 \times 61.7 \times 15$ m^3 at the third step) was made comparable with the highest

resolution of FEM modeling ($62.5 \times 62.5 \times 15.6$ m^3). I also notice that the rim domain at the second and third steps of NIE had a width of two cells (from the previous step) in all directions. Final comment on the NIE modeling set up is that I adopted the first order polynomial basis for all steps, assuming that the cell's sizes (at least at the second and the third steps) are small enough not to consider a higher-order polynomial basis.

Figure 3.13 presents the modeled tippers at 16 periods from 10 to 10000 sec. In addition, the figure demonstrates the observed (i.e. estimated from the data) tippers and their uncertainties.
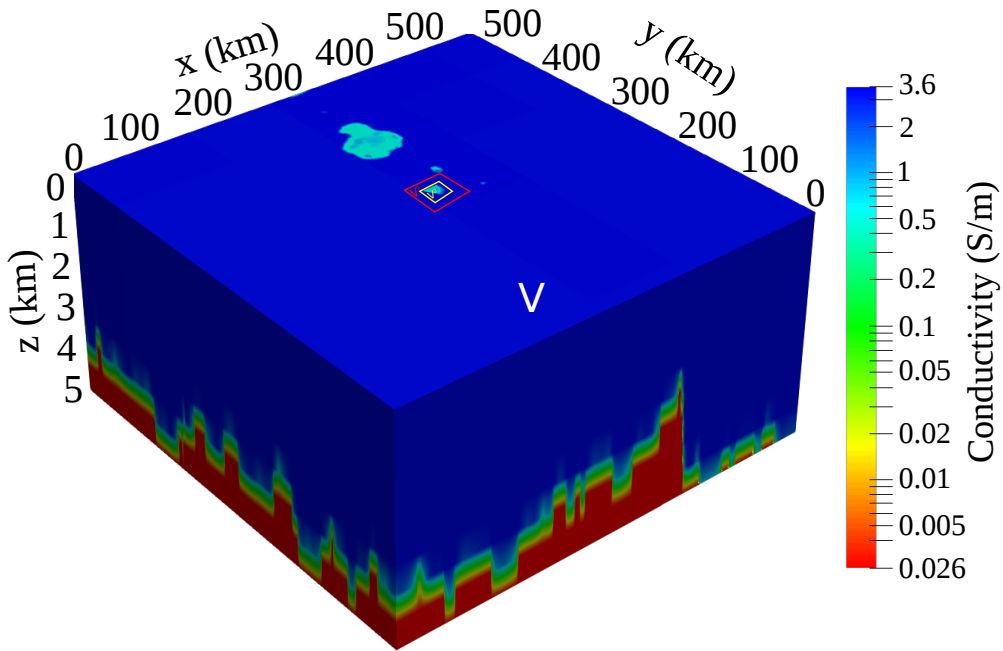
Figure 3.12: 3-D view of conductivity distribution in the domain V of the GAN model. Red and yellow rectangles depict lateral size of the V^1 and V^2 domains, respectively.

Table 3.3: Number of cells and their sizes in three-step NIE modeling in the GAN model.

	$N_x \times N_y \times N_z$	$dx \times dy$	dz
1st step of NIE (at V)	$600 \times 600 \times 10$	926×926 m^2	5×500, 5×600 m
2nd step of NIE (at V^1)	$380 \times 380 \times 4$	185×185 m^2	15, 35, 150, 300 m
3rd step of NIE (at V^2)	$588 \times 588 \times 4$	61.7×61.7 m^2	15, 35, 150, 300 m

It is seen from the figure that NIE- and FEM-based tippers agree (within experimental uncertainties) at all periods in both components and in both real and imaginary parts. It is important to stress that I did not expect an "ideal" fit, since I cannot make the

Table 3.4: Computational loads (memory and CPU time) used for three-step NIE modeling in the GAN model. The computational time is the averaged time for the simulation at one period and for one plane wave excitation. Computations are performed using 600 CPUs. Computational loads for the conventional IE method (at V, and a fine grid corresponding to the NIE 3rd step resolution) are estimated without actual computations; this is due to the fact that such modeling would require enormous computational resources.

	RAM (GB)	Wall time (sec)
Nested IE approach	146	543
Conventional IE, fine	5.6×10^4	1.6×10^5

conductivity distributions identical due to the substantially different grids used by NIE and FE solvers.

It is noteworthy that both NIE- and FEM-based results for the real part of T_{zy} differ from the observed tippers. As pointed out by Morschhauser et al. (2019), the noticeable disagreement may result from the 3-D conductivity structures that are incompatible with the assumed 1-D model beneath the ocean, for example, due to conductive seafloor sediments at some distance from the station, or due to inaccuracies of the bathymetry model that is adopted in the study.

Lastly, Table 3.4 illustrates one of the most significant results of the approach: remarkable computational efficiency of the developed nested IE. As is seen from the table, the nested IE modeling significantly outperforms the modeling based on the most advanced conventional IE solver (Kruglyakov & Kuvshinov, 2018) in terms of memory and CPU time.

3.5 Concluding remarks

I have developed an efficient and accurate 3-D EM modeling tool based on an IE approach with multi-nested domains. I successfully verify the workability and accuracy of the developed nested IE tool by performing modelings in both idealized and realistic 3-D conductivity models. I demonstrate that the new tool is two orders of magnitude more efficient – in terms of both memory and CPU time – than one of the most advanced conventional IE solvers (Kruglyakov & Kuvshinov, 2018).

In addition, I proposed a "rim domain" concept which further improves the efficiency
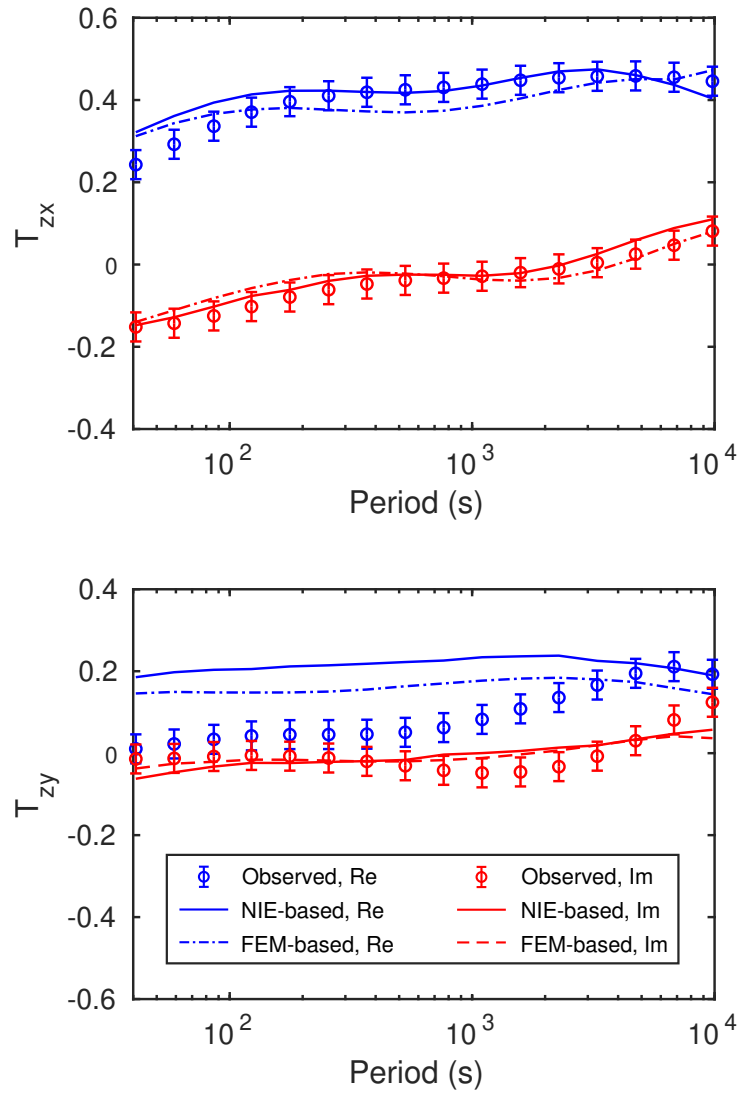
Figure 3.13: Modeled and observed tippers at the GAN observatory. The observed and FEM-based tippers are taken from (Morschhauser et al., 2019). Uncertainties of the observed responses are indicated by error bars.

of the multi-nested IE approach.

The developed tool, in combination with the global-to-Cartesian EM modeling tool (Chen et al., 2020), which aims to efficiently model longer-period responses, gives us an opportunity to invert EM responses in as wide a range of periods as practicable, and thus to constrain the electrical structure of the Earth's interior from the crust to the middle mantle, which will be presented in Chapter 4.

Chapter 4

Joint inversion of MT tippers and GDS transfer functions constrains crustal and upper mantle conductivity structures beneath islands

The content of this chapter is submitted to *Journal of Geophysical Research: Solid Earth* as: Chen, C., Kuvshinov, A., Kruglyakov, M., Munch, F., & Rigaud, R. Constraining the crustal and mantle conductivity structures beneath islands by a joint inversion of multi-source magnetic transfer functions. *Journal of Geophysical Research: Solid Earth*, under revision.

Summary

In this chapter, I present a quasi 1-D tool to simultaneously invert multi-source magnetic transfer functions (TFs), including magnetotelluric (MT) tippers (with period ranging from a few minutes to 3 hours), solar quiet (Sq) global-to-local (G2L) transfer functions (TFs; with period ranging from 6 hours to 24 hours) of ionospheric origin, and magnetospheric global Q-responses (with period ranging from a few days to a few months). I further jointly invert the aforementioned multi-source TFs to constrain the local conductivity structures beneath three islands located in South Atlantic, Indian Ocean and

North Pacific. The recovered conductivity profiles suggest upper mantle plumes beneath Tristan da Cunha and Oahu islands. Besides, results indicate resistive lithosphere of different thicknesses beneath these three islands, showing a progressive thickening of oceanic lithosphere with age.

4.1   Introduction

Electrical conductivity provides a wealth of information on the thermal and compositional state of the Earth's interior, being highly sensitive to fractions of conductive phases, such as fluids, and partial melts (cf. Khan, 2016; Karato, 2011; Yoshino & Katsura, 2013). The relatively shallow electrical structures of the Earth are conventionally studied with magnetotelluric (MT) sounding technique, whereas deeper structures are probed with geomagnetic depth sounding (GDS) method. Both methods use the transfer functions (TFs) concept to analyse and interpret the data, thus implying the work in the frequency domain. MT TFs are either impedances, relating horizontal electric to the horizontal magnetic field or/and tippers, relating vertical to the horizontal magnetic field (Berdichevsky & Dmitriev, 2008). GDS TFs are more diverse (cf. Banks, 1969; Olsen, 1998; Schmucker, 1999a; Püthe & Kuvshinov, 2014; Kuvshinov et al., 2021) and mostly rely on magnetic field data.

In general, continents are explored by MT and GDS methods significantly better than the oceans for two obvious reasons: a) surface observations are tied to islands that are sparsely scattered; b) seafloor observations are usually logistically as well instrumentally demanding. Despite the latter challenge, more and more seafloor MT studies are conducted (cf. Suetsugu et al., 2012; Baba et al., 2013, 2017a; Key et al., 2013; Naif et al., 2013; Matsuno et al., 2020), thus stepwise filling the substantial gap in our knowledge about the Earth's electric conductivity structure in the vast oceanic regions. However, the coverage with EM observations in the oceans remains poor. In this context, the magnetic field data from island geomagnetic observatories is considered a valuable source of information about marine electric structures. Due to the very irregular distribution of the island observatories, at most, one can constrain the local one-dimensional (1-D) conductivity structures beneath each observatory and explore the lateral variability of the recovered 1-D structures.

Previously, EM induction studies at islands primarily relied on the GDS technique being applied to either magnetic signals of magnetospheric (cf. Khan et al., 2011; Munch et al., 2018; Chen et al., 2020) or ionospheric (cf. Simpson et al., 2000; Guzavina et al., 2019) origin; recall that under "ionospheric" signals, we understand variations due to solar quiet (Sq) current system (with periods ranging from a few hours to one day), and under "magnetospheric" signals – variations due to ring current (with periods ranging from a few days to a few months). With TFs estimated from these data, one can obtain 1-D conductivity profiles (beneath specific locations) in depth range of $\sim 200 - 1500\,\text{km}$.

Samrock & Kuvshinov (2013) demonstrated that island MT tippers (estimated from magnetic field variations with periods ranging from a few minutes to 3 hours) are sensitive to 1-D conductivity distributions beneath islands at depths $\sim 0 - 200\,\text{km}$. Morschhauser et al. (2019) performed "quasi" 1-D inversion of MT tippers estimated from the data at two island geomagnetic observatories and found significant lateral variability of the recovered 1-D conductivity profiles. Note that the term "quasi" is used to stress the fact that during 1-D inversions, the three-dimensional (3-D) forward modelling operator is invoked to calculate tippers which are large due to the ocean induction effect (OIE), originated from large lateral conductivity contrasts between ocean and land (Parkinson & Jones, 1979; Kuvshinov et al., 2002).

So far, island GDS and MT TFs were analyzed/inverted separately, resulting in a reduced vertical resolution of the recovered conductivity structures outside the target depths. Therefore, it is tempting to invert them jointly to improve the resolution and diminish uncertainties in the recovered conductivity models.

Note that the idea of joint inversion of multi-source electromagnetic (EM) TFs is not completely new. For instance, Egbert & Booker (1992) and Bahr et al. (1993) inverted GDS TFs (in the form of conventional C-responses; (Banks, 1969; Olsen, 1998)), and MT impedances to constrain 1-D conductivity models beneath two continental sites in North America and Europe, respectively. Grayver et al. (2017) and Kuvshinov et al. (2021) obtained a globally averaged 1-D oceanic conductivity structure based on a joint analysis of satellite-detected tidal signals (in the form of tidally-induced radial magnetic field component at satellite altitude) and the signals of magnetospheric origin (in the form of global C/Q-responses). Munch et al. (2020) jointly inverted new GDS global-to-

local (G2L) TFs (Püthe et al., 2015), of both ionospheric and magnetospheric origins (to be called henceforth as Sq and Dst G2L TFs, respectively). They estimated the G2L TFs at several continental observatories and performed their 1-D inversions to detect lateral variability in the recovered 1-D conductivity profiles.

In this study, I develop a methodology to jointly invert island GDS and MT TFs for local 1-D conductivity distributions in the presence of known laterally-variable bathymetry, which controls the strength and spatial structure of OIE. Note that our previous numerical studies suggest that the proper account for the OIE requires 3-D forward modellings at fine grids, which I perform using nested domains formalism (Chen et al., 2020, 2021).

I implemented the developed methodology to invert GDS and MT TFs estimated at three island geomagnetic observatories. I have chosen islands to locate in different tectonic environments, specifically, in the Indian Ocean (Cocos (West) island), in South Atlantic (Tristan da Cunha island), and North Pacific (Oahu island). I point out that since I work with island geomagnetic observatory data, the only MT TFs we can estimate are tippers. As for GDS TFs, I exploit new Sq G2L TFs (Guzavina et al., 2019), which allow us to account for the complex spatiotemporal structure of the Sq current system. I omitted longer-period, Dst G2L TFs since they appeared to be of questionable quality (non-smooth behaviour, significant uncertainties) at considered islands; recall that estimating Dst TFs requires a very long time series of observations with accurate control of the baseline, which is often not the case when one deals with island data. Due to the period range of the considered TFs – from a few minutes to one day – I constrain conductivity structures in the depth range from the surface down to approximately mantle transition zone (~ 500 km). To avoid ambiguity in conductivity distribution at larger depths, I also include into the joint inversion longer-period global Q-responses estimated by Kuvshinov et al. (2021).

Finally, I interpret the recovered local 1-D conductivity profiles in terms of lithosphere thickness and the presence/absence of mantle plume beneath the considered islands.

4.2 Multi-source magnetic transfer functions

4.2.1 Magnetotelluric tippers

The source of geomagnetic field variations with periods shorter than 3 hours can be approximated by a vertically incident plane wave. This allows to relate the vertical magnetic field component, Z, with the horizontal magnetic field, $\mathbf{H}_\tau = (H_x \, H_y)$, via the tipper $T = (T_{xy} \, T_{zy})$ (Berdichevsky & Dmitriev, 2008)

$$Z(\mathbf{r}_s, \omega) = T_{zx}(\mathbf{r}_s, \omega)H_x(\mathbf{r}_s, \omega) + T_{zy}(\mathbf{r}_s, \omega)H_y(\mathbf{r}_s, \omega) \tag{4.1}$$

where $\mathbf{r}_s$ is an observation site, and $\omega = 2\pi/T$ is the angular frequency, and T is the period. Tippers were estimated in period range 5 min - 3 hours. Details on the island data to estimate tippers, and their estimation are discussed in the paper of Rigaud et al. (2021), seeing their section "Estimating tippers from the data". Circles with error bars in Figure 4.3 depict the estimated tippers.

4.2.2 Sq global-to-local transfer functions

The source of daily Sq variations is the ionospheric current system, which has a complex spatio-temporal structure (Yamazaki et al., 2016; Finlay et al., 2017). Despite this, there were several studies that analyzed Sq variations and utilized a variant of local C-response concept, which represents the source via a single spherical harmonic (SH) which is specific for each Sq period (cf. Schmucker, 1964; Simpson et al., 2000; Bahr & Filloux, 1989). However, presently there exists a consensus that the description of the ionospheric source by a single SH is too simplistic. Alternatively, local C-responses can be estimated without prior assumptions about the source geometry (cf. Olsen, 1998). The prerequisite for the successful implementation of this approach is a relatively dense regional grid of observations in the region of interest, which is not the case with island observations.

To account for the complex spatio-temporal structure of the Sq source, I resort to (non-conventional) global-to-local transfer functions, T_n^m, that relates a set of SH expansion coefficients describing the source to a locally measured vertical magnetic field

component (Püthe et al., 2015; Guzavina et al., 2019)

$$Z(\mathbf{r}_s, \omega) = \sum_{n,m \in L(\omega)} \epsilon_n^m(\omega) T_n^m(\mathbf{r}_s, \omega), \tag{4.2}$$

where $L(\omega)$ specifies a subset of SH for each Sq period ($T_p = 24/p$ hours, $p = 1, 2, 3, 4$). For details on the estimation and fundaments underlying the Sq G2L TFs, the reader is referred to the paper of Guzavina et al. (2019) (see their Sections 2–4). In short, for each period T_p, I first determine the external (inducing) SH coefficients, ϵ_n^m, describing the source from horizontal magnetic field components measured at global net of observatories assuming a prior 3-D conductivity Earth. Then, the corresponding T_n^m are estimated by relating the local (island) vertical magnetic field component with the determined source coefficients. Only data from geomagnetic quiet days (with 48-hr average aa index smaller than 7 nT) and from equinoctial months available from 1997 until 2021 were used for Sq G2L TFs estimation. I estimated Sq G2L TFs using magnetic data measured at Cocos-Keeling Islands (CKI), Honolulu (HON) and Tristan da Cunha (TDC) geomagnetic observatories during 128, 370 and 139 magnetically quiet days, respectively. As terms with $n = p + 1$ and $m = p$ are expected to be dominant (Schmucker, 1999b), I analyze T_{p+1}^p only. Circles with error bars in Figure 4.4 represent the estimated Sq G2L TFs. It is also important to stress that the Sq data were corrected for ocean tidal signals (Guzavina et al., 2018).

4.2.3   Global Q-responses

The source of geomagnetic field variations with periods longer than one day is primarily the magnetospheric ring current. At the Earth's surface, this source is well approximated by the $n = 1$ and $m = 0$ term, and this fact allows us to estimate global Q-responses relating the induced and inducing SH coefficients, ϵ_1^0 and ι_1^0

$$\iota_1^0(\omega) = Q_{11}^{00}(\omega)\epsilon_1^0(\omega). \tag{4.3}$$

Details on the data to estimate global Q-responses and on their estimation can be found in the paper of Kuvshinov et al. (2021), seeing their section "Estimating dominant Q-response". Circles with error bars in Figure 4.5 depict the estimated global Q-responses.

4.3 Forward modeling and quasi-1D inversion

4.3.1 Forward modeling
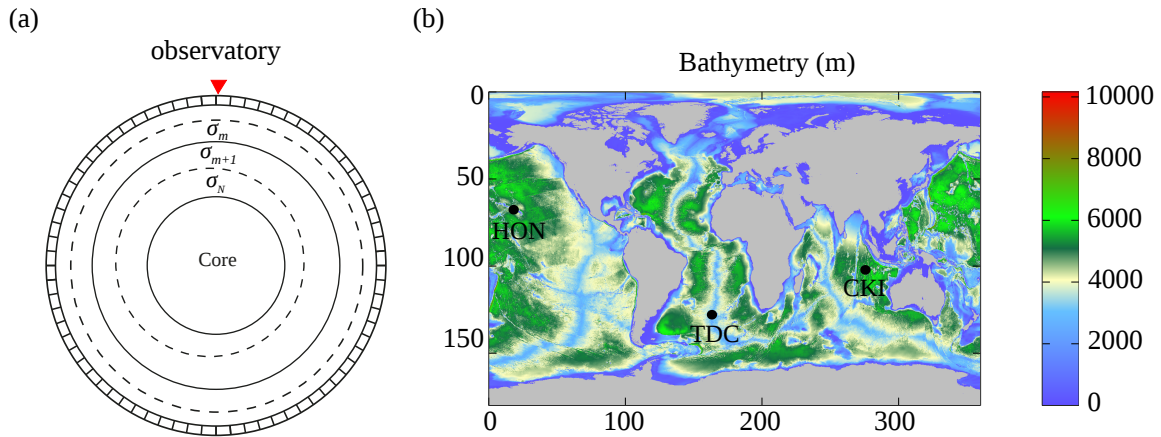
Figure 4.1: Left: model parameterization adopted in this study. The conductivity models consist of a 1-D layered Earth overlaid by a surface layer (or several layers) representing nonuniform conductivity distributions in the oceans and landmasses. Conductivity distributions in the surface layers(s) are constructed by using bathymetry data (right); by black dots are shown locations of island geomagnetic observatories data from which are used in this paper.

In this study, I aim to reveal 1-D conductivity structures beneath islands. As I already discussed in the introduction, island EM TFs are substantially distorted by the ocean induction effect (OIE). To account for the OIE, we exploit a conductivity model which includes nonuniform oceanic layer(s) and 1-D mantle underneath (cf. Figure 4.1). Calculation of electric and magnetic fields, **E** and **H**, in models with 3-D conductivity distribution, σ, requires numerically solving Maxwell's equations

$$\nabla \times \mathbf{H}(\mathbf{r}) = \sigma(\mathbf{r})\mathbf{E}(\mathbf{r}) + \mathbf{j}^{ext}(\mathbf{r}),$$
$$\nabla \times \mathbf{E}(\mathbf{r}) = i\omega\mu_0\mathbf{H}(\mathbf{r}),$$

(4.4)

where $i = \sqrt{-1}$, μ_0 is the magnetic permeability of the free space, and $\mathbf{j}^{ext}$ is the extraneous current. $\mathbf{r} = (r, \theta, \phi)$ and $\mathbf{r} = (x, y, z)$ for global and Cartesian problem setups, respectively.

Previous studies (Chen et al., 2020, 2021) show that the OIE in island EM responses can be accurately accounted for by using a nested integral equation (IE) approach and

invoking high-resolution bathymetry. Within the nested domain approach, the modeling is first performed at a large domain and on a coarse grid. Then the results are refined in the region of interest by performing modeling at a smaller domain and on a denser grid. In this study, I adopt the "nested" Cartesian-to-Cartesian tool (Chen et al., 2021) to compute tippers and the "nested" global-to-Cartesian tool (Chen et al., 2020) to compute Sq G2L TFs. In both tools, the core modules of Cartesian solver PGIEM2G (Kruglyakov & Kuvshinov, 2018) are used. As for the calculation of global Q-responses, I exploit the conventional IE solver by Kuvshinov (2008). Different TFs – depending on their periods and spatial scale of the source – may require different discretization of the corresponding 3-D models. Specifically, for tippers calculation, I first performed modeling at a large domain and coarse lateral grid (with 180×180 cells of 2×2 km^2 size), and then at a smaller domain and finer lateral grid (with 60×60 cells of 1×1 km^2 size). As for vertical discretization, for both simulations, the 3-D modeling domain was discretized by six layers of $0.5, 0.5, 1, 1, 1.5$ and 1.5 km thicknesses. Note that since I exploit IE-based solvers, the vertical extent of the modeling domain goes down to 6 km – the maximum depth column around considered islands. To calculate Sq G2L TFs, I first performed modeling at a global (spherical) grid with lateral resolution of $1° \times 1°$, and then at smaller (Cartesian) domain and finer lateral grid with 80×80 cells of 10×10 km^2 size, corresponding to $\sim 0.09° \times 0.09°$ resolution. Finally, global Q-responses are calculated at a global grid with a lateral resolution of $1° \times 1°$. A thin shell set-up was invoked to calculate both Sq G2L TFs and global Q-responses, meaning that the 6-km layer is substituted by a thin shell of laterally-variable conductance where the conductance is obtained as a product of bathymetry and globally averaged sea-water conductivity (3.2 S/m). Note that I performed systematic model studies to justify the parameters describing the models, namely, cell, grid and domain sizes. 3-D conductivity (or 2-D conductance) distributions in the considered models are constructed by using the $30'' \times 30''$ bathymetry data from the General Bathymetry Chart of the Oceans (GEBCO; Becker et al. (2009)).

4.3.2 Joint quasi 1-D inversion

The inverse problem is treated as an optimization problem such that

$$\phi_d(\mathbf{m}) + \lambda\phi_m(\mathbf{m}) \underset{\mathbf{m}}{\longrightarrow} \min, \tag{4.5}$$

where $\phi_d(\mathbf{m})$ is the data misfit, λ and $\phi_m(\mathbf{m})$ are the regularization parameter and regularization term, respectively. $\mathbf{m} = [\beta(\sigma_1), \beta(\sigma_2), \cdots, \beta(\sigma_N)]$ denotes the vector of model parameters, where $\beta(\cdot)$ is a log-based transformation ensuring the positivity of the arguments, and N is the number of parameters.

The data misfit term $\phi_d(\mathbf{m})$ reads

$$\phi_d(\mathbf{m}) = \sum_{k\in\chi}\left(\frac{1}{N_k}\sum_{i=1}^{N_k}\left|w_i^k(f_i^k(\mathbf{m}) - d_i^k)\right|^2\right), \tag{4.6}$$

where χ is a set of TFs from different methods, and w^k, f^k and d^k are the corresponding data weights, 3-D forward operator and observed (i.e. estimated from the data) TFs, respectively. Normalizing with the numbers of actual entries (N_k) aims to equate the contribution from each method in joint inversion (Key, 2016).

The regularization term $\phi_m(\mathbf{m})$ reads

$$\phi_m(\mathbf{m}) = \frac{1}{p_m}\sum_{j=1}^{N}|\mathbf{l}_j\mathbf{m}|^{p_m}, \tag{4.7}$$

where $\mathbf{l}_j$ is the regularization operator of the j-th model parameter. In the implementation, it is the first derivative with respect to the model parameters. The scalar p_m is set to 1.5, which provides a balance between sharp conductivity contrast and smooth models (Grayver & Kuvshinov, 2016). The trade-off between data fit and regularization terms in the course of inversion is determined by means of the L-curve analysis (Hansen, 1992).

I solve the optimization problem (4.5) using a stochastic algorithm, which is called Covariance Matrix Adaptation Evolution Strategy (CMAES) method (Hansen & Ostermeier, 2001). It is relevant to note here that CMAES is a global optimization method, and it finds a global minimum for a moderate number of iterations. More details on

CMAES method are given in Appendix D.

4.4   Results

4.4.1   Conductivity models

I use the methodology presented in the previous section to simultaneously invert tippers, Sq G2L TFs and global Q-responses to obtain the local 1-D conductivity profiles beneath three island geomagnetic observatories (cf. their locations in Figure 4.1).

In the course of inversion, the 1-D part of the model is parameterized by 45 layers with thicknesses ranging from 500 meters near the surface to 200 km at the core-mantle boundary (CMB). Below CMB the conductivity is fixed to a high conductivity value – 10^5 S/m. Note that topography is not included in the model, as it has a negligible effect on the TFs in the considered period range. The starting model was taken as a homogeneous 0.01 S/m conductor down to CMB.

Figure 4.2 shows the recovered 1-D conductivity profiles beneath TDC, HON and CKI – coloured by red, black and blue, respectively – along with the corresponding 95% confidence intervals. The details on the recovered layered models – namely, the depths to the top of the layers, thicknesses of the layers, conductivities and their upper and lower bounds in the layers – are given in Appendix C. The figure also demonstrates – coloured by green – 1-D section (and corresponding confidence interval) from Kuvshinov et al. (2021). This model was obtained by a joint inversion of satellite-detected radial magnetic field component due to M2 oceanic tide and global Q-responses; the model is believed to represent the globally averaged 1-D mantle structure beneath oceans.

One can see from the figure that 1-D profiles beneath each observatory differ from the globally averaged oceanic 1-D conductivity structure in the depth range from the surface down to ~ 500 km. The difference is especially noticeable in the first 100 km, i.e. at the lithospheric depths. Here the global profile appears to be much less conductive than the local profiles, thus better resolving the expected high resistance ($\sim 10^8 - 10^9 \ \Omega \cdot m^2$) of the rigid lithosphere. The reason for the higher (less plausible) values of conductivities in the local profiles at lithospheric depths is as follows. Local profiles are obtained from the inversion of TFs, which are estimated from the magnetic field variations of iono-
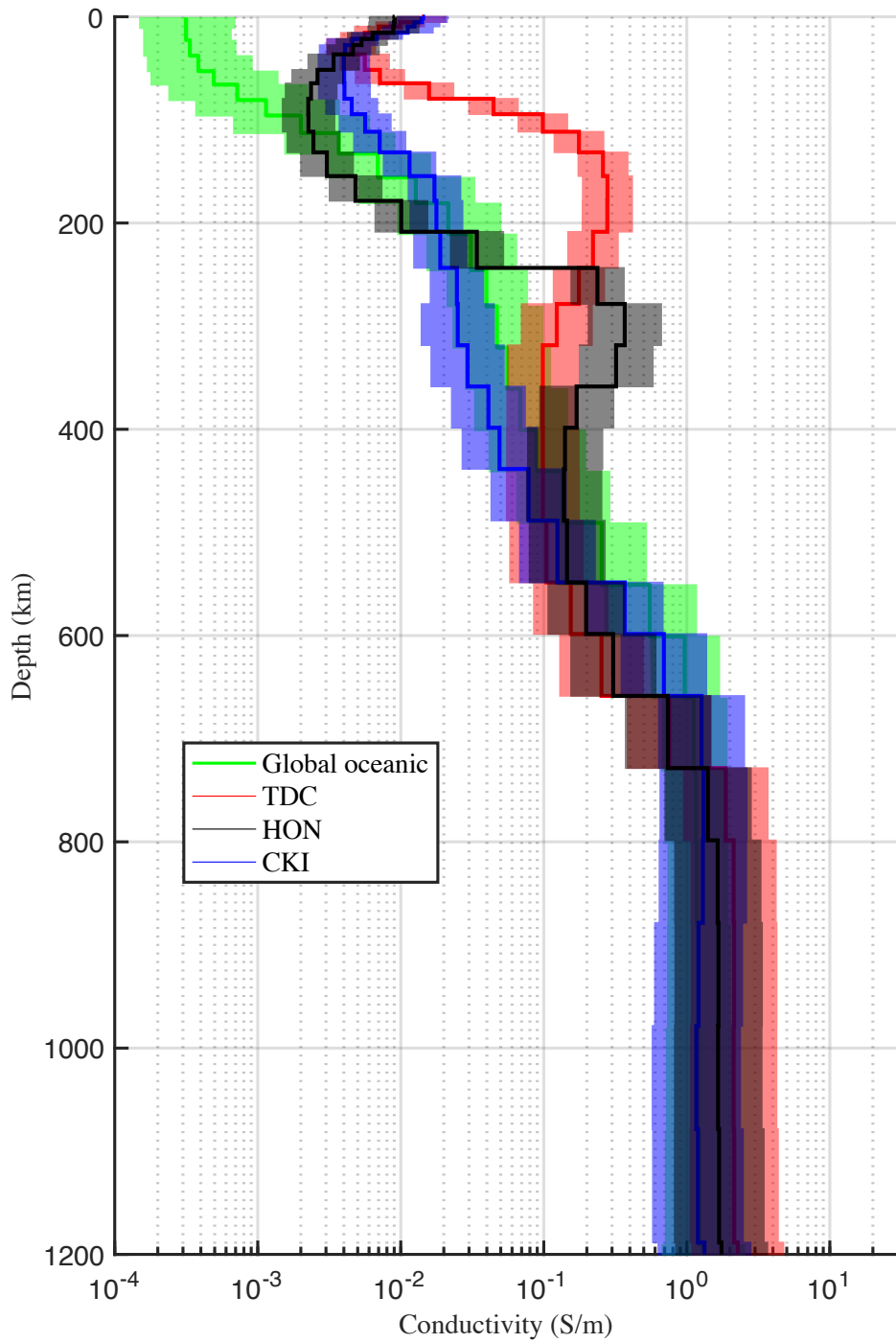
Figure 4.2: Recovered 1-D conductivity models along with 95 % confidence intervals beneath TDC, HON and CKI observatories by jointly inverting MT tippers, Sq G2L TFs and global Q-responses. 1-D section (and corresponding confidence interval) in green is from Kuvshinov et al. (2021). This model was obtained by a joint inversion of satellite-detected tidal signals and global Q-response and it is believed to represent the globally averaged 1-D mantle structure beneath oceans.

spheric and magnetospheric origin. Due to the purely inductive excitation mechanism of these variations, and because the magnetic field on the surface of the Earth is purely poloidal, the corresponding TFs are weakly sensitive to the resistive structures in the subsurface (Fainberg et al., 1990). In contrast to these TFs, tidal magnetic fields used to constrain global oceanic conductivity at lithospheric depths are excited by motionally-driven ocean electric currents that have a unique characteristic – galvanic coupling of these currents with the Earth's subsurface. This enhances the sensitivity of the analysed magnetic fields to the Earth's resistive structures since these fields (even observed above the Earth and hence being purely poloidal) are influenced by the toroidal (galvanic) part of the primary tidal EM field. Despite less reliable values of conductivity in the local profiles at the lithospheric depths, one can interpret the results in terms of the lithosphere thickness: we will discuss this topic in Section 4.4.3.

As for lateral variability of the local profiles, they are – in the same (0 – 500 km) depth range – also markedly different from each other. Note that the sameness of the profiles below 500 km depth is not surprising since I used global – thus laterally-uniform – Q-responses to constrain conductivity in the lower mantle. Beneath Oahu and Tristan da Cunha islands, where mantle plumes are hypothesized (Rychert et al., 2013; Schlömer et al., 2017), I observe an apparent feature – an enhanced conductivity zone in the recovered profiles. However, the depth to the high-conducting zone is noticeably different in HON and TDC profiles. Beneath Tristan da Cunha island, this zone is centred at a depth of $\sim$ 180 km, which agrees with a depth where the velocity of the conduit/plume is revealed by a finite-frequency tomography (Schlömer et al., 2017, cf. their Figure 9) is minimal; recall that the researchers usually associate the lower velocity zones with higher conductivity regions. The high-conducting zone beneath HON is revealed, however, at a larger depth (of $\sim$ 300 km) which is also in accordance with seismic results in that region (Wolfe et al., 2009, cf. their Figure 2).

Figures 4.3-4.5 present experimental (i.e. estimated from the data) TFs and TFs computed in the local 3-D models with the recovered 1-D mantle profiles. One can observe good general agreement between the modelled and experimental TFs. The remaining (rather small, however) discrepancy could be attributed to the hypothetical 3-D conductivity structures beneath islands, which are incompatible with an assumption I

made, namely, that underlying crust and mantle are 1-D. Another cause of the difference could be a potential inaccuracy of the bathymetry data that is used in the study.
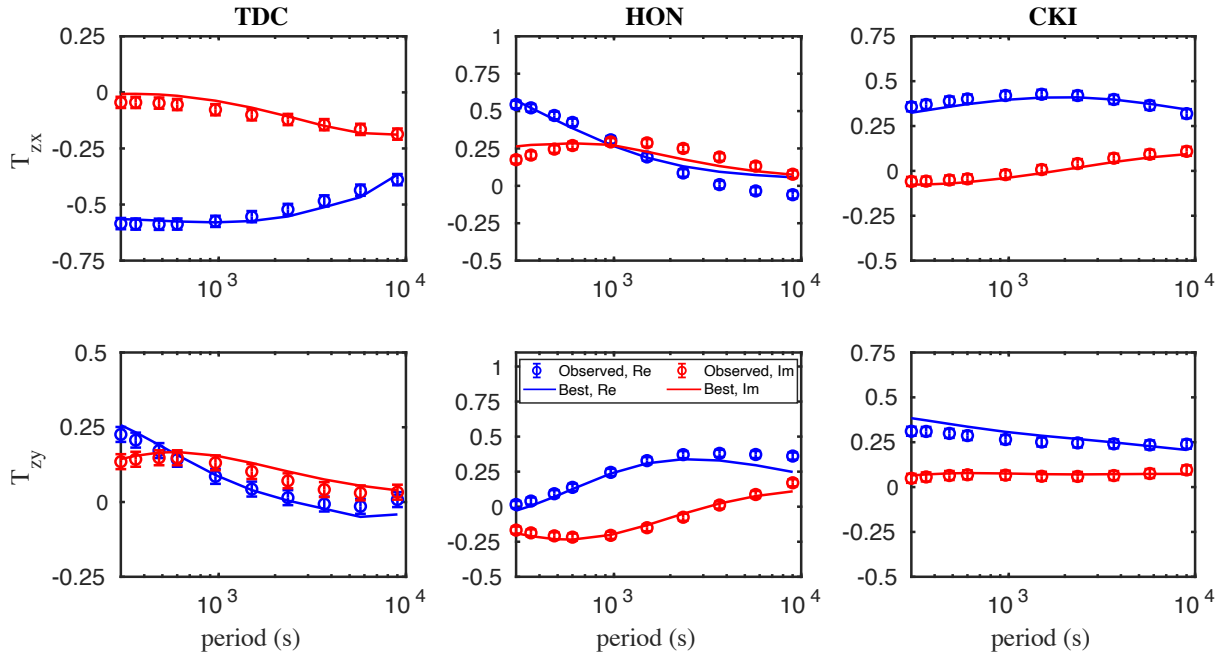
Figure 4.3: Comparison of the observed and modeled best-fitting MT tippers at TDC, HON and CKI observatories, respectively. Uncertainties of the observed MT tippers are indicated by the error bars.
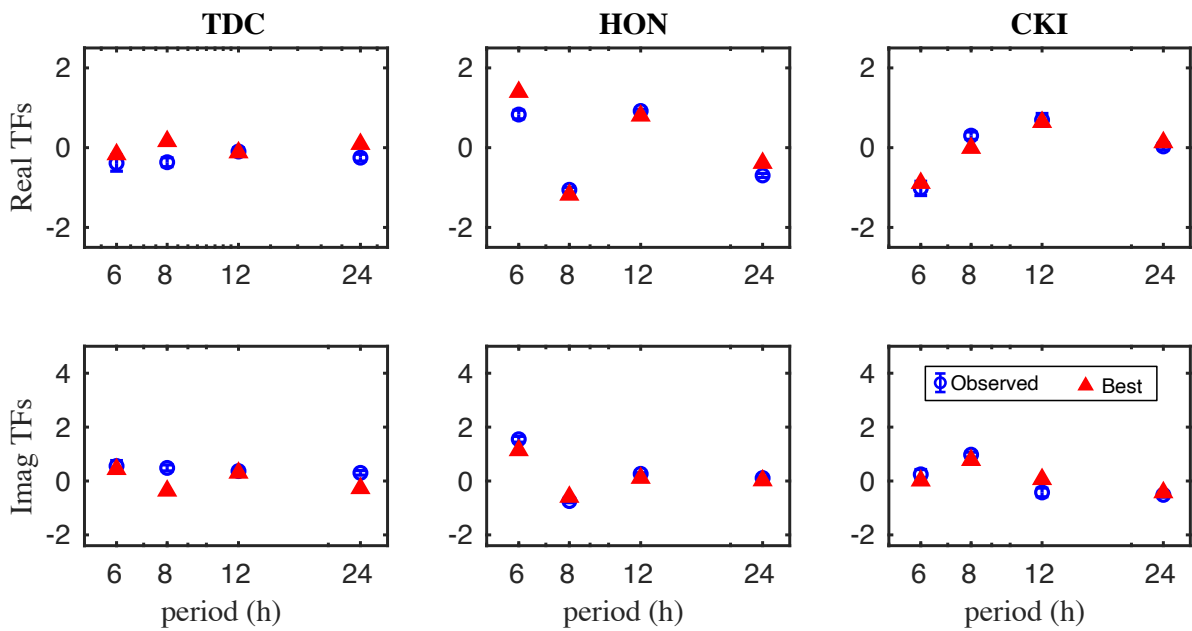
**Figure 4.4:** As in Figure 4.3, but for Sq global-to-local transfer functions at three island geomagnetic observatories.
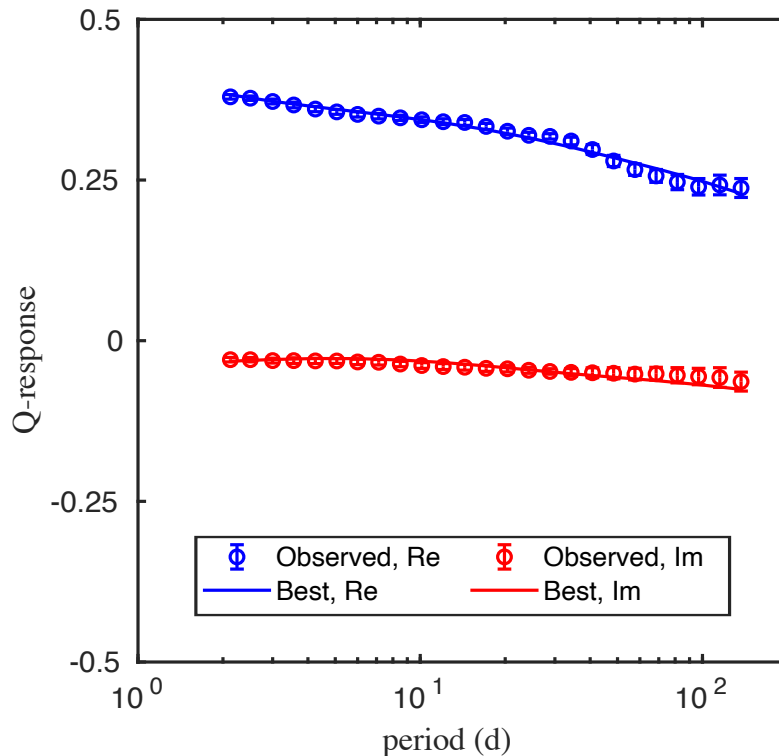
Figure 4.5: Comparison of the observed and modeled best-fitting global Q-responses. Uncertainties of the observed global Q-responses are indicated by the error bars.

In the next section, I compare the results with those of independent EM studies.

4.4.2 Comparison of new 1-D profiles with the models from the independent EM studies

Figure 4.6a compares the revealed 1-D profile (red) with the profiles obtained by Morschhauser et al. (2019) (black) and Baba et al. (2017a) (blue) below TDC observatory. For the reference, a globally averaged 1-D mantle structure beneath oceans from (Kuvshinov et al., 2021) (green) is shown. The 1-D model of Morschhauser et al. (2019) was obtained by inverting the same MT tippers, using the same, quasi 1-D, problem setup and the same, CMAES, inversion technique. The distinct difference between our approaches is that we invert – along with tippers – the longer-period TFs, thus covering the wide period range between 5 minutes and 110 days; this allows to constrain conductivity at larger depths. Bearing this information in mind, I expected to see similar conductivity distributions from the surface down to a depth of ∼ 100 km – which is indeed the case. Note that
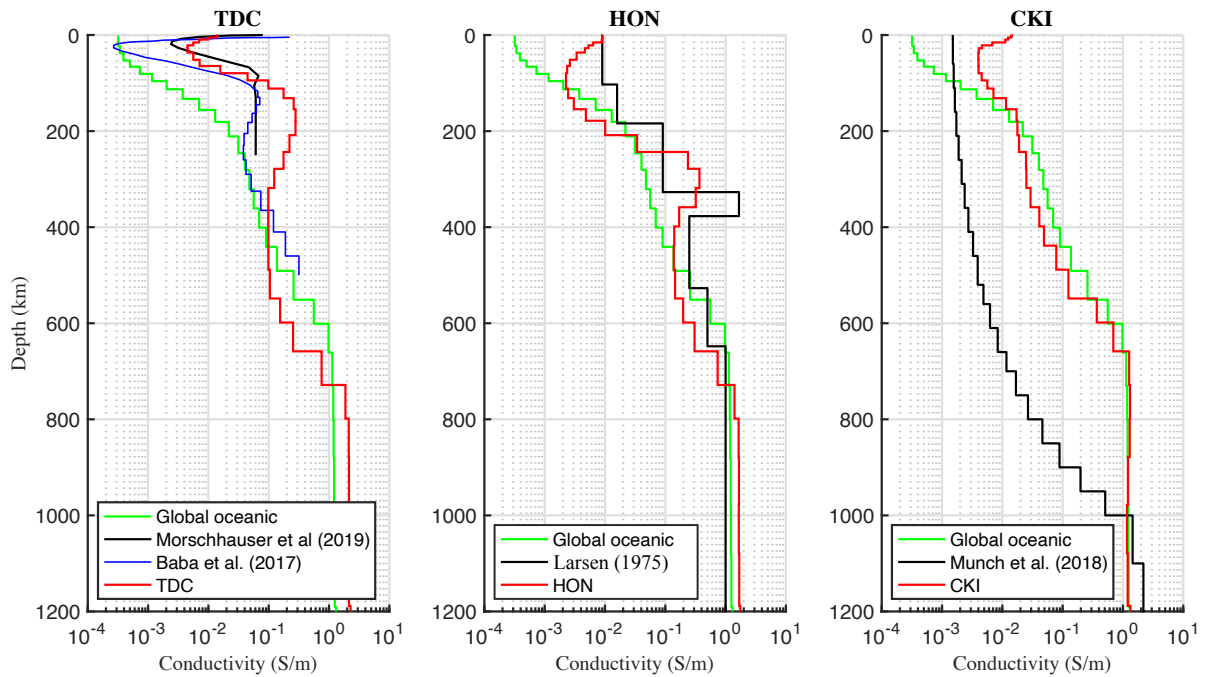
Figure 4.6: Comparison of the revealed 1-D conductivity profiles beneath three island observatories. Plots (a), (b) and (c) present the results for TDC, HON and CKI observatories, respectively.

tippers are TFs with periods shorter than 3 hours; thus, inversion of only tippers, as it is done by Morschhauser et al. (2019), does not permit constraining conductivity structures at upper mantle depths reliably. This is why the profile from Morschhauser et al. (2019) below 100 km does not show any conductivity variations. Very low conductivities seen in a global profile at shallower depths are not reproduced in both this study and Morschhauser et al. (2019)' result. The reason for this disagreement I explained in the previous section. As for the profile from Baba et al. (2017a) it is much closer to a global model at depths smaller than 100 km, in terms of very low values of conductivity. I see the following explanation for that. The profile by Baba et al. (2017a) is obtained by an inversion of sea-bottom impedances estimated in the period range between 500 sec and two days. In contrast to the TFs estimated from the surface (purely poloidal) magnetic field in this study, impedances are evaluated from the plane-wave horizontal electric and magnetic fields. Plane-wave horizontal electric field (in the non-1-D environment, and either at the surface or sea bottom) contains the toroidal/galvanic part, which is sensitive to the resistive lithospheric structures (Fainberg et al., 1990). Moreover, in a non-1-D environment, the sea-bottom horizontal magnetic field also comprises

the toroidal constituent. This, in particular, means that the sea-bottom impedances – along with tidal signals – allow researchers to probe high-resistive/low-conducting lithosphere. Besides, their sea-bottom impedances were estimated at as long as one day; this allowed the authors to likely constrain conductivity distribution down to a depth of ~ 500 km. Interestingly, their profile also contains the enhanced conductivity structure, however, less pronounced and at a slightly shallower depth.

Figure 4.6b compares the HON 1-D profile obtained by this study with that from Larsen (1975). His profile was obtained by inversion of long-period (periods between 4 hours and 10 days) impedances estimated from around two years of HON observatory magnetic data and electric field measurements nearby. As the author stated, there appears to be a unquestionably resolved highly conducting zone in the depth range $330 - 380$ km. Remarkably, I also reveal the enhanced conductivity zone at comparable depths. Since the minimum period in his analysis was 4 hours, it precludes resolving the structures at the shallow, $0 - 200$ km, depths; this explains the difference between our and Larsen's results at these depths.

Figure 4.6c compares the CKI 1-D profile with that from Munch et al. (2018); note that their profile is the only EM result we found in the literature for this region. As in figures for TDC and HON, globally averaged 1-D mantle structure beneath oceans (Kuvshinov et al., 2021) is also shown. One can observe that starting from ~ 150 km depth, our 1-D model closely follows the global profile. In particular, and in contrast to TDC and HON models, the CKI profile does not contain a high-conducting zone in the upper mantle, which agrees with an absence of plume below Cocos Islands. One can also see that profile of Munch et al. (2018) differs much from our and global profiles, at least, down to a depth of 1000 km. This is not completely strange, since long-period (periods longer than one day) local C-responses inverted by Munch et al. (2018) are only sensitive to lower mantle structures of the Earth; moreover, the lateral grid $(1° \times 1°)$ used in their study to account for the OIE during their quasi 1-D inversion seems too coarse to reproduce OIE adequately (see Chen et al. (2020) for more details on this issue).
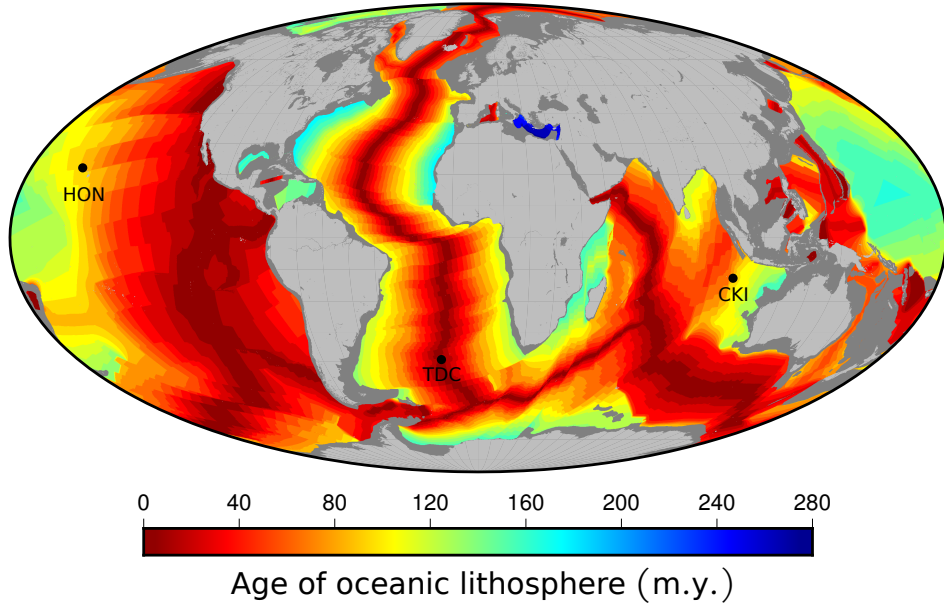
4.4.3 Estimating thickness of the oceanic lithosphere

The lithosphere is the rigid outermost layer of the Earth, and it is the fundamental mechanical unit of the plate tectonics theory (Turcotte & Schubert, 2002). The lithosphere base, which is called a lithosphere-asthenosphere boundary (LAB), divides the rigid lid from the weaker mantle. A variety of physical parameters (seismic velocity, density and electrical conductivity) are adopted to map the thickness of the lithosphere (or depth to LAB) (McAdoo & Sandwell, 1985; Winterbourne et al., 2009; Rychert & Shearer, 2009, 2011; Grayver et al., 2016, among others).

Table 4.1: Thickness of the oceanic lithosphere, T_l, beneath TDC, HON and CKI as estimated in this study and independent studies.

Island	From where estimates of T_l are taken	T_l (km)
TDC	This study	36
	Morschhauser et al. (2019)	30
	Baba et al. (2017b)	35
	Based on eq. (4.8)	58
HON	This study	110
	Woods et al. (1991) and Woods & Okal (1996)	100
	Based on eq. (4.8)	127
CKI	This study	80
	Based on eq. (4.8)	100

I estimated the thickness of the oceanic lithosphere, T_l, beneath TDC, HON and CKI observatories from the recovered local 1-D conductivity profiles as the depth (in the shallow part of the upper mantle) from where conductivity starts to increase, after a gradual decrease at smaller depths. The same procedure was applied to estimate T_l from the conductivity profiles below TDC obtained by Morschhauser et al. (2019) and Baba et al. (2017b). I summarize the results in Table 4.1. Remarkably, the estimates appeared to be rather similar, giving a thin lithosphere of $\sim$ 36 km. As for HON, I obtain the relatively thick lithosphere with $T_l \sim$ 110 km below this region. Interestingly, this value is close to an estimate of $T_l \sim$ 100 km obtained by Woods & Okal (1996) from the seismic data in the region. Finally for CKI, I estimate T_l as $\sim$ 80 km. The results indicate that T_l significantly varies from island to island, but surprisingly enough that by averaging local estimates, I get a value, 75 km, which is very close to the global estimate of T_l (72 km) obtained by Grayver et al. (2016).

Figure 4.7: Global distribution of the oceanic lithosphere age. Data is taken from Müller et al. (2008).

In addition, I estimated oceanic lithosphere thickness beneath the considered islands using the lithosphere age consideration. There is a common consensus that the oceanic lithosphere thickens with age. This thickening occurs by conductive cooling, which converts hot asthenosphere into the lithospheric mantle and causes the oceanic lithosphere to become increasingly thick and dense with age (Turcotte & Schubert, 2002; Lu et al., 2021). Specifically, the age of the lithosphere can be converted into the thickness of the oceanic lithosphere utilizing the following formula (Ranalli, 1995)

$$T_l(\theta, \phi) = 2.32\sqrt{\kappa\, a(\theta, \phi)}, \tag{4.8}$$

where κ is the an average thermal diffusivity for the silicate rocks – taken as $10^{-6} m^2 s^{-1}$, cf. Table 7.4 of Ranalli (1995) – and a is the laterally-variable age of the lithosphere (cf. Figure 4.7). I provide in the table the estimates of T_l based on eq. (4.8) taking lithosphere ages beneath TDC, HON and CKI observatories as 20, 95 and 60 million years (Müller et al., 2008), respectively. As is seen from the table, estimates of T_l based on a joint inversion of EM TFs by this study generally agree with estimates based on eq. (4.8), thus confirming a progressive thickening of oceanic lithosphere with age. It is interesting to notice that – in spite of general agreement – estimates of T_l by this study

are systematically ~ 20 km lower than estimates based on eq. (4.8).

4.5 Conclusions

I developed a tool to simultaneously invert island multi-source transfer functions in terms of 1-D conductivity distribution. Specifically, I jointly invert magnetotelluric tippers (periods from a few minutes to three hours), new global-to-local (G2L) magnetic transfer functions (periods from a few hours to one day), and global Q-responses (periods from a few days to a few months). Inverting TFs in a broad period range allows to constrain the conductivity in a wide depth range – from crust to lower mantle. The critical feature of the tool is a rigorous and accurate account for the ocean induction effect (OIE) which makes the forward problem fully 3-D. OIE is modelled using a nested integral equation approach and invoking high-resolution bathymetry. The inverse problem is solved employing a stochastic algorithm which finds a global minimum and does this for a moderate number of iterations.

I implemented the developed methodology to invert TFs estimated at three islands of different tectonic environments. Beneath two of them – Tristan da Cunha (South Atlantic) and Oahu (North Pacific) – I observe an apparent feature in the recovered profiles – an enhanced conductivity zone, which is in agreement with seismic results suggesting mantle plumes beneath these islands. Besides, the recovered 1-D conductivity profiles indicate oceanic lithosphere of different thicknesses beneath each island, confirming a progressive thickening of oceanic lithosphere with age.

The ongoing work is an implementation of the tool to constrain 1-D conductivity distributions beneath many other islands around the world where long-term magnetic measurements have been performing (Rigaud et al., 2021). I notice that the tool is designed so that it can be easily adapted to include alternative TFs, like impedances and G2L electric TFs, provided long-period electric field data at islands are also available. Noteworthy, using "electric" TFs allows the probing of high-resistive structures in the lithosphere. Moreover, substituting tippers with impedances enables us to apply the multi-source TFs inversion concept to constrain 1-D conductivity distributions (from crust to lower mantle) beneath *inland* geomagnetic observatories. Such inversion is also a topic of future research, which in particular will include a proper treatment (cf.

Püthe et al., 2014) of potential galvanic effects in electric TFs. Finally, I would like to mention that along with TFs originating from the signals of external (either ionospheric or magnetospheric) origin, one can think about adding tidal EM signals (at locations where these signals are reliably detectable) into a joint inversion to further reduce the uncertainties in the recovered 1-D conductivity profiles.

Chapter 5

Conclusions and outlook

5.1 Conclusions

My doctoral project focused on constraining the local 1-D electrical conductivity structures beneath oceans from crust to upper mantle by jointly inverting multi-source electromagnetic transfer functions, including MT tippers and long-period GDS transfer functions of both ionospheric and magnetospheric origins, estimated from island geomagnetic observatory and satellite data. Special attention was paid to efficiently calculate island MT and GDS responses/transfer functions accounting for the ocean induction effect, which originates from the substantial lateral conductivity contrast between land and ocean.

To this end, two forward modelling tools based on a nested IE approach in both Cartesian and spherical geometries were developed to calculate respective MT and GDS responses/transfer functions. Specifically, I developed:

(1) Cartesian-to-Cartesian 3-D electromagnetic forward modelling tool to efficiently calculate magnetotelluric tippers/impedances. The tool allows researchers to account for the effects of non-uniform distant structures and, at the same time, to accurately model the results from local anomalies. The IE modelling is first performed at a large domain and on a (laterally uniform) coarse grid within this approach. Then the results are refined in the region of interest by performing modelling at a smaller domain and on a (laterally-uniform) denser grid. At the latter stage, the modelling results obtained at the previous step are exploited. I

used the developed tool to calculate the MT tippers at observatory Gan, located
on the southernmost island of the Maldives. I obtained a very good agreement
between observed and modelled MT tippers using the developed tool.

(2) Global-to-Cartesian 3-D electromagnetic forward modelling tool to efficiently cal-
culate GDS responses/transfer functions. It, again, allows researchers to effi-
ciently calculate the EM responses in the problem setups requiring highly detailed
bathymetry in the (local) region of interest. The IE modelling in spherical ge-
ometry is first performed on the whole globe using a coarse grid, and then the
results are refined in the region of interest by IE modelling in Cartesian geometry
at a smaller domain and on a denser grid. I computed long-period responses at
two islands (Cocos-Keeling and Honolulu) geomagnetic observatories by exploiting
different – from relatively coarse $1° \times 1°$ to very fine $0.01° \times 0.01°$ – lateral grids,
and demonstrate that very local bathymetry variation substantially influences the
GDS responses at periods as long as 20 days. Using the responses computed at
$0.01° \times 0.01°$ grid, I obtain new 1-D conductivity models beneath considered islands
and observe remarkable agreement between modelled and experimental responses.
In particular, I reproduced the anomalous behaviour of observed responses at the
Cocos-Keeling observatory.

A quasi-1D inverse tool was developed to simultaneously invert multi-source electro-
magnetic (EM) responses in terms of 1-D conductivity distribution based on the above-
mentioned forward modelling solvers. These EM responses include MT tippers (with
periods ranging from a few minutes to 3 hours), solar quiet (Sq), global-to-local transfer
functions (with periods ranging from 6 hours to 24 hours), and magnetospheric global
Q-responses (with periods ranging from a few days to a few months). Inverting TFs in a
broad period range allows us to constrain the conductivity in a wide depth range – from
crust to lower mantle. The critical feature of the inverse tool is a rigorous and accurate
account for the OIE, which makes the forward problem fully 3-D. OIE is modelled using a
nested integral equation approach and invoking high-resolution bathymetry. The inverse
problem is solved by employing a stochastic algorithm that finds a global minimum and
does this for a moderate number of iterations.

I implemented the developed methodology to invert TFs estimated at three islands

in different tectonic environments. As a result, I obtained local 1-D conductivity profiles beneath three island observatories. Beneath two of them – Tristan da Cunha (South Atlantic) and Oahu (North Pacific) – I observe an apparent feature in the recovered profiles – an enhanced conductivity zone, which agrees with seismic results suggesting mantle plumes beneath these islands. The retrieved conductivity profiles indicate a conductive upper mantle beneath Tristan da Cunha and Oahu islands, where mantle plumes are hypothesized (Rychert et al., 2013; Schlömer et al., 2017). Beneath Tristan da Cunha island, the enhanced conductivity zone is centred at a depth of ~ 180 km, which is in agreement with a depth where the velocity of the conduit/plume, revealed by a finite frequency tomography, is minimal (Schlömer et al., 2017). The high-conducting zone beneath HON is detected, however, at a more significant depth (of ~ 300 km), which is also following seismic results in that region (Wolfe et al., 2009). Besides, the recovered 1-D conductivity profiles indicate oceanic lithosphere of different thicknesses beneath each island, confirming a progressive thickening of oceanic lithosphere with age.

5.2 Outlook for future studies

5.2.1 Constraining 1-D conductivity distributions beneath both island and inland geomagnetic observatories

I developed a quasi 1-D tool to invert multi-source electromagnetic transfer functions simultaneously in my PhD project. Then, I applied the developed tool to constrain the local 1-D conductivity structures beneath three island geomagnetic observatories. The ongoing work is an implementation of the tool to constrain 1-D conductivity distributions beneath many other island geomagnetic observatories around the world where long-term magnetic measurements have been performing (Rigaud et al., 2021). It is worth noting that the tool is designed to be easily adapted to include alternative TFs, like impedances and G2L electric TFs, provided long-period electric field data at geomagnetic observatories are also available. Also noteworthy, using "electric" TFs allows researchers to probe high-resistive structures in the lithosphere.

Moreover, substituting tippers with impedances enables us to apply the multi-source TFs inversion concept to constrain the local 1-D conductivity distributions (from crust to

lower mantle) beneath *inland* geomagnetic observatories. Such inversion is also a topic of future research, which in particular will include a proper treatment (cf. Püthe et al., 2014) of potential galvanic effects in electric TFs. Finally, along with TFs originating from the signals of external (either ionospheric or magnetospheric) origin, one can add tidal EM signals (at locations where these signals are reliably detectable) into a joint inversion to further reduce the uncertainties in the recovered 1-D conductivity profiles.

Further, I would like to explore the lateral variability of the recovered 1-D conductivity models and constrain the hydrogen/melt content in the mantle by invoking laboratory conductivity measurements and using the approach described in Munch et al. (2018) and Munch et al. (2020).

5.2.2   Constraining the regional 3-D conductivity structures beneath regions with good spatial coverage by observations

As mentioned in Chapter 1, although significant efforts have been made to constrain the Earth's conductivity structures by MT and GDS studies, the family of global 3-D models produced to date is yet to reach a consensus. The present discrepancy is primarily due to the inherent strong non-uniqueness of the inverse problem arising from spatial sparsity and irregularity of data distribution. Hence, at most, one can constrain the conductivity structure reliably beneath the regions with good spatial coverage by observations (for instance, beneath China, the United States, Europe, and Australia).

In this context, my future goal is to develop a semi-global 3-D inversion tool to jointly invert MT and GDS transfer functions in spherical geometry, using a gradient-type optimization method and exploiting novel efficient IE-based 3-D forward modelling solver GEMMIE (Kruglyakov & Kuvshinov, 2022). Then, I plan to use this 3-D inversion tool to constrain the 3-D electrical conductivity distributions – from crust to mantle – beneath China and Europe. Furthermore, the recovered 3-D conductivity models could be integrated with laboratory conductivity measurements to constrain the hydrogen content in the mantle and coupled with seismic and geodynamic models to better understand the lithosphere's thinning and related fluid-melt activities.

5.2.3 Compiling a global 3-D electrical conductivity model

So far, several global 3-D electrical conductivity models of the relatively shallow (down to the depth of approximately 100 km) layers of the Earth have been built (Everett et al., 2003; Alekseev et al., 2015; Grayver, 2021). However, there is no global 3-D electrical conductivity model from crust to mantle, as far as I know. A long-term and profound goal is to build a global multi-resolution 3-D electrical conductivity model in a depth range of 0 - 1500 km, including seawater, sediments, the Earth's crust, lithosphere/asthenosphere, and mantle.

Compilation of such a global 3-D model could follow the approach used in Alekseev et al. (2015). First, the Earth can be divided into several spherical layers. The vertical and lateral boundaries of the layers are established based on the available data sets (e.g., the global maps of high-resolution bathymetry, sedimentary, crustal and lithosphere thicknesses). Then, each element of the structure is assigned either a specific conductivity value or conductivity versus depth distribution, according to available laboratory data and generalized models (cf. Jones, 1999; Palshin, 1996). Then, the global model could be refined by incorporating conductivity models obtained in regional MT studies and/or other disciplines. Many existing conductivity models could be compiled into this global 3-D model, including:

- Global 3-D electrical conductivity model of the ocean and marine sediments built by Grayver (2021);

- Regional 3-D conductivity models revealed by large-scale MT studies, for instance, crustal 3D conductivity models beneath China (Wei et al., 2001; Bai et al., 2010; Xu et al., 2019; Dong et al., 2020; Xu et al., 2020), Australia (Robertson et al., 2016), Central Mongolia (Käufl et al., 2020), northwest Pacific (Tada et al., 2014; Utada & Baba, 2014), and the United States (Patro & Egbert, 2008; Meqbel et al., 2014; Yang et al., 2021);

- Mantle 3-D conductivity models beneath, for instance, China and Europe, as described in Section 5.2.2; I note that such models are still to be built;

- Local 1-D conductivity models beneath globally-distributed geomagnetic observatories (in the regions where the spatial distribution of the data is poor), as described

in Section 5.2.1.

5.2.4   Implementation of alternative approaches to 3-D EM forward modeling

A robust and efficient 3-D EM forward modelling tool is vital for EM inversion. In this Ph.D. project, I developed two forward modelling tools based on a nested integral equation approach in Cartesian and spherical geometries to calculate MT and GDS responses/transfer functions efficiently. The FFT method is applied to accelerate the computation and reduce the memory consumption, which requires a uniform discretization in the corresponding direction. The developed tools allow accounting for the effects of distant structures correctly and, at the same time, to model the results from local anomalies accurately. However, these forward modelling tools have two shortcomings: (a) a regular grid is adopted to discretize the modelling domain, which has difficulty in approximating the complicated models, for instance, the coastal line and topography; and (b) if more than one region is of practical interest, one needs to perform the modellings several times to obtain the accurate results in multiple regions of interest; this is especially true for G2C tool. Alternative methods to perform fast and accurate 3-D large-scale EM forward modelling are as follows:

- Fast multipole method (FMM). FMM has already been successfully applied to accelerate IE-based 3-D EM modellings (Gumerov & Duraiswami, 2005; Ren et al., 2013b, among others), but no literature reports the FMM application to global 3-D EM forward modelling. Noteworthy, FMM allows for using nonuniform and irregular grids (tetrahedrons) for discretization.

- Hybrid integral equation-finite element (IE-FE) method. Within the approach, the IE modelling is first performed in a large domain and on a coarse (regular) grid. Then the results are refined in the region of interest by performing FE modelling at a smaller domain and on a denser grid using the IE modelling results obtained in the previous step. This method allows tetrahedral grids to discretize the local domain and accurately approximate the complex structures.

5.2.5   Simultaneous inversion of source and conductivity models

Estimating GDS global-to-local (G2L) transfer functions (TFs) and their subsequent inversion rely on an estimation of the expansion coefficients describing the source (Guzavina et al., 2019; Munch et al., 2020, among others). Such estimation requires knowledge of the Earth's background conductivity model. Guzavina (2020) compared the G2L TFs estimated using two different background models and found a non-negligible difference between them. This result advocates iterative updating of the source coefficients and conductivity models during estimation and inversion of G2L TFs. Alternatively, one can think about estimating the source coefficients and recovery of the conductivity model simultaneously.

Appendices

Appendix A

Numerical tests to verify the global-to-Cartesian 3-D EM forward modelling tool

A.1 Introduction

Here, I present the results of two numerical tests, which aim to verify the proposed global-to-Cartesian (G2C) three-dimensional (3-D) electromagnetic (EM) forward modeling tool described in Chapter 2.

A.2 1-D layered Earth model

First, I consider a 1-D layered Earth's model, excited by the external source described by the first zonal spherical harmonic (Y_1^0). 1-D conductivity profile is taken from (Grayver et al., 2017). The electric and magnetic fields at period of 1 day are calculated analytically (Kuvshinov & Semenov, 2012) and by G2C approach. Within G2C approach, the whole modeling domain is divided into two, global and local, domains, where the local domain is confined by $82\,^\circ - 90\,^\circ$ colatitudes and $0\,^\circ - 8\,^\circ$ longitudes. At both, global and local, modeling stages, the lateral resolution of the model is taken as $1° \times 1°$. At global modeling and local stage the fields are calculated by "spherical" X3DG code (Kuvshinov, 2008) and "Cartesian" PGIEM2G code (Kruglyakov & Kuvshinov, 2018), respectively.
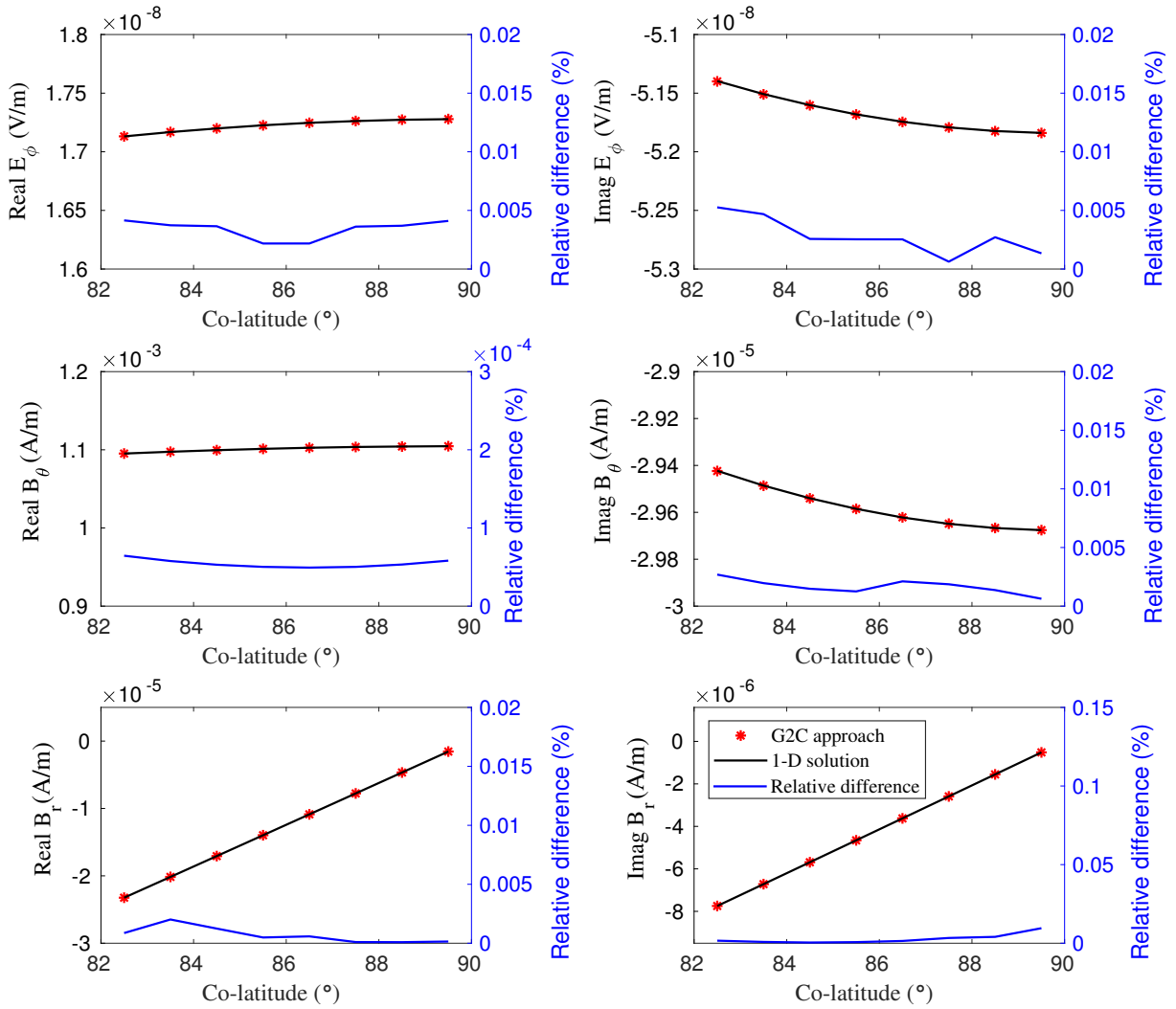
Figure A.1: Analytical and G2C fields calculated at the surface of the Earth along colatitudinal profile in 1-D conductivity model of the Earth. Period is 1 day, the source is described by the first zonal spherical harmonic. See further details in the text.

Figure A.1 shows the analytical and G2C E_ϕ, B_θ and B_r calculated at the surface of the Earth along colatitudinal profile which crosses the local domain. Note, that since the source of excitation is described by Y_1^0 spherical harmonic, and the Earth's conductivity model is 1-D, there is no dependence of the results on longitude and only E_ϕ, B_θ and B_r components of EM field are non-zero. Excellent agreement between analytic and G2C results is observed, with the relative difference between them being less than $0.01\,\%$ for all components.
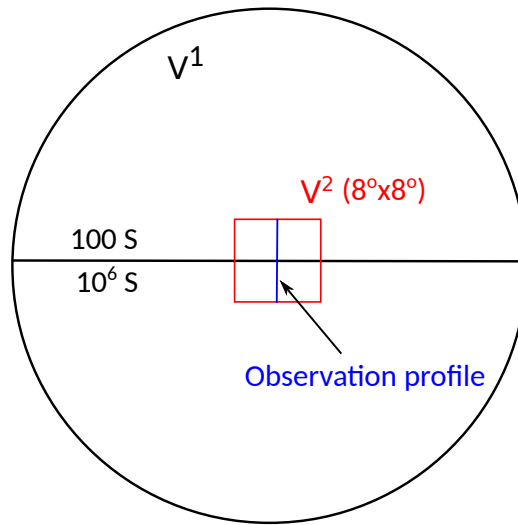
Figure A.2: A sketch of the North-South hemisphere model.

A.3 North-South (N-S) hemisphere model

The second test is performed using the so-called North-South (N-S) hemisphere model. It consists of surface thin shell with hemispherical distribution of conductance and 1-D mantle underneath. The same 1-D conductivity profile as in the first test is used for the conductivity distribution in the mantle. The conductances in northern (colatitudes $0° - 90°$) and southern (colatitudes $90° - 180°$) hemisphere are taken as $100\,\text{S}$ and $10^6\,\text{S}$, respectively (cf. Figure A.2). Note that G2C is validated against X3DG solver only, since the latter code was thoroughly and systematically benchmarked in a number of publications (Yoshimura & Oshiman, 2002; Kelbert et al., 2014; Velímský et al., 2018, among others). I also notice that recently introduced FEM-based global solver (Grayver et al., 2019) was also validated against the X3DG code. The model is again excited by Y_1^0 source, and again I calculate the fields at period of 1 day. The following four modeling scenarios are considered: (1) The fields are calculated globally on a "fine", $0.5° \times 0.5°$, grid using X3DG code, and these fields are referred as the "true" fields; (2) the fields are calculated globally on a coarser, $0.5° \times 1°$, grid using again X3DG code; (3) the fields are calculated using G2C approach. At global and local modeling stages, $0.5° \times 1°$ and $0.5° \times 0.5°$ grids are invoked, respectively. The local domain is confined by $86°$- $94°$ colatitudes and $0°$- $8°$ longitudes; (4) the fields are calculated by PGIEM2G code on a grid of $0.5° \times 0.5°$ resolution, considering the local domain only. Note that in the latter scenario the background 1-D section was chosen to include uniform surface thin

shell of 10^6 S conductance. As in the first test, there is no dependence of the results on a longitude and only E_ϕ, B_θ and B_r components of EM field are non-zero.
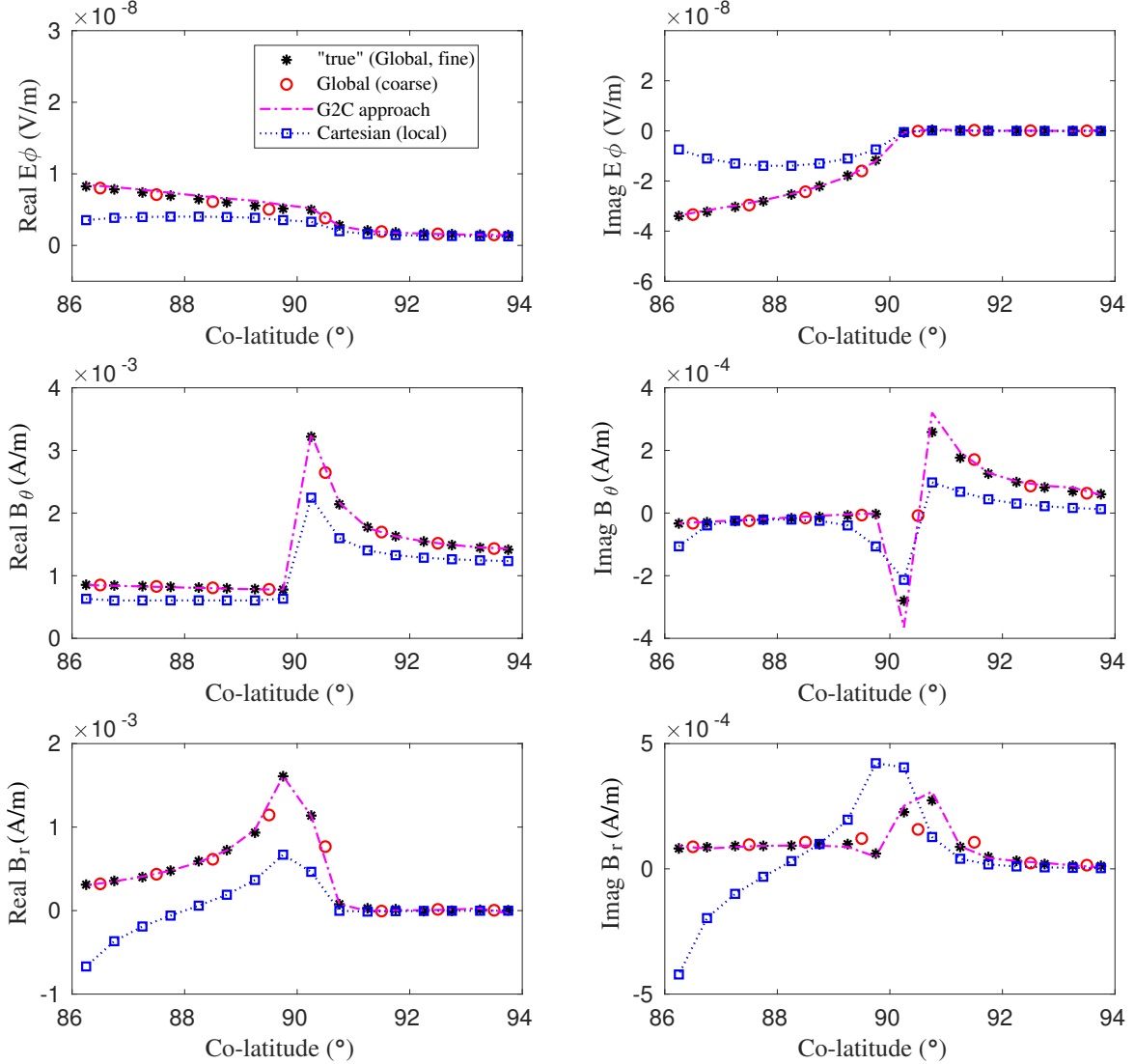
Figure A.3: The fields calculated in the N-S hemisphere model using four different modeling scenarios. Period is 1 day, the source is described by the first zonal spherical harmonic. See further details in the text.

As seen from Figure A.3, the fields calculated during the fourth modeling scenario, i.e. when only local domain is considered, differ from other three solutions. It is noteworthy that imaginary parts of B_r component obtained by X3DG using a coarser grid ($0.5° \times 1°$) differ from the "true" imaginary parts. Remarkably, the fields calculated by G2C approach matches very well with the "true" solution, in spite of the fact that global calculations were performed using a grid of $0.5° \times 1°$. Also note that there is a small discrepancy between "true" X3DG and G2C results which can be attributed to the fact

that different – collocation and Galerkin – methods are used in X3DG and PGIEM2G codes to numerically solve the corresponding IE.

Appendix B

Details of numerical implementation of C2C approach

B.1 Introduction

In this Appendix, I present some details on the numerical implementation of the nested integral equation approach described in Chapter 3.

B.2 Basis functions construction

Let domain $\widetilde{V}$ be divided into $N^{\text{cells}} = N_x N_y N_z$ rectangular cells

$$\widetilde{V}_n = [x_n \ x_n + h_x^n] \times [y_n \ y_n + h_y^n] \times [z_n \ z_n + h_z^n], \quad n = 1, 2, \ldots, N^{\text{cells}}. \tag{B.1}$$

Then, the local scalar basis functions $\Psi_n^{n_x, n_y, n_z}(x, y, z)$ for each cell $\widetilde{V}_n$ are expressed as

$$\Psi_n^{n_x, n_y, n_z}(x, y, z) = \frac{2\sqrt{2}}{\sqrt{h_x^n h_y^n h_z^n}} L_{n_x}\left(2\frac{x - x_n}{h_x^n} - 1\right) \times L_{n_y}\left(2\frac{y - y_n}{h_y^n} - 1\right) \times L_{n_z}\left(2\frac{z - z_n}{h_z^n} - 1\right). \tag{B.2}$$

Here, $L_n = \sqrt{\frac{2n+1}{2}} P_n$, P_n is the Legendre polynomial of n-th order, and $n_{x(y,z)} = 0, 1, \ldots, N_{x(y,z)}^P$, where $N_{x(y,z)}^P$ are the maximum polynomial orders along x-, y- and z-directions.

Then, the vector basis functions $\boldsymbol{\Psi}_n$, $n = 1, 2, \ldots, N$, $N = 3N^{\text{cells}}\left(N_x^P + 1\right)\left(N_y^P + 1\right)\left(N_z^P + 1\right)$ are assembled as $\boldsymbol{\Psi} = (\Psi_x, \Psi_y, \Psi_z)$, where $\Psi_{x,y,z}$ stand for $\Psi_n^{n_x, n_y, n_z}$ in eq. (B.2). Note that $\boldsymbol{\Psi}_n$ are orthonormal at $\widetilde{V}_n$ due to the orthonormality of the L_n. To obtain the orthonormality of $\boldsymbol{\Psi}_n$ at the whole domain $\widetilde{V}$, one just needs to define $\boldsymbol{\Psi}_n(\mathbf{r}) = 0, \mathbf{r} \notin \widetilde{V}_n$.

B.3   Calculating integrals of the basis functions products

As explained in Chapter 3, the realization of the nested approach requires computation of the following expression

$$\left(\mathbf{E}^{add\,(c)}, \boldsymbol{\Psi}_{n,k}^{(f),\,\text{loc}}\right) \approx \sum_{V_m^{(c)} \subset V^{\text{loc}}} \sum_{l=1}^{K_c} u_{m,l}^{add\,(c)} \int\limits_{V_n^{(f),\,\text{loc}}} \boldsymbol{\Psi}_{n,k}^{(f),\,\text{loc}}(\mathbf{r}) \boldsymbol{\Psi}_{m,l}^{(c)}(\mathbf{r}) dV_n^{(f),\,\text{loc}},$$

$$n = 1, 2, \ldots, N_f, \quad k = 1, 2, \ldots, K_f.$$

(B.3)

or, in other words, one has to calculate the integral over $V_n^{(f),\,\text{loc}}$ in eq. (B.3). Below, I show how this integral can be calculated analytically.

To do this, let me first substitute the basis functions introduced in Appendix B.2 into the integral in eq. (B.3). As a result, we have

$$
\int\limits_{V_m^{(f),\mathrm{loc}}} \Psi_m^{(f),\mathrm{loc}}(\mathbf{r})\Psi_n^{(c)}(\mathbf{r})d V_m^{(f),\mathrm{loc}} = \sqrt{\frac{2n_x^{(c)}+1}{h_x^{n(c)}}\frac{2n_y^{(c)}+1}{h_y^{n(c)}}\frac{2n_z^{(c)}+1}{h_z^{n(c)}}\frac{2n_x^{(f)}+1}{h_x^{m(f)}}\frac{2n_y^{(f)}+1}{h_y^{m(f)}}\frac{2n_z^{(f)}+1}{h_z^{n(f)}}}
$$

$$
\times \int\limits_{x_m^{(f)}}^{x_m^{(f)}+h_x^{m(f)}} P_{n_x}^{(c)}\left(2\frac{x-x_n^{(c)}}{h_x^{n(c)}}-1\right) P_{n_x}^{(f),\mathrm{loc}}\left(2\frac{x-x_m^{(f)}}{h_x^{m(f)}}-1\right) dx
$$

$$
\times \int\limits_{y_m^{(f)}}^{y_m^{(f)}+h_y^{m(f)}} P_{n_y}^{(c)}\left(2\frac{y-y_n^{(c)}}{h_y^{n(c)}}-1\right) P_{n_y}^{(f),\mathrm{loc}}\left(2\frac{y-y_m^{(f)}}{h_y^{m(f)}}-1\right) dy
$$

$$
\times \int\limits_{z_m^{(f)}}^{z_m^{(f)}+h_z^{m(f)}} P_{n_z}^{(c)}\left(2\frac{z-z_n^{(c)}}{h_z^{n(c)}}-1\right) P_{n_z}^{(f),\mathrm{loc}}\left(2\frac{z-z_m^{(f)}}{h_z^{m(f)}}-1\right) dz.
$$

$$(B.4)$$

As is seen from eq. (B.4), it is sufficient to show how to compute one, for instance, the first integral; other integrals can be computed in a similar way. Let me introduce the following notations

$$
s = x, \ s_1 = x_m^{(f)}, \ s_2 = x_m^{(f)}+h_x^{m(f)}, \ q_1 = x_n^{(c)}, \ q_2 = x_n^{(c)}+h_x^{m(c)}, \ l = n_x^{(c)}, \ k = n_x^{(f)}.
$$

$$(B.5)$$

Then, the first integral in eq. (B.4), with the corresponding prefactor, can be rewritten as

$$
\frac{2n_x^{(f)}+1}{h_x^{m(f)}}\int\limits_{x_m^{(f)}}^{x_m^{(f)}+h_x^{m(f)}} P_{n_x}^{(c)}\left(2\frac{x-x_n^{(c)}}{h_x^{n(c)}}-1\right) P_{n_x}^{(f),\mathrm{loc}}\left(2\frac{x-x_{m1}^{(f)}}{h_x^{m(f)}}-1\right) dx
$$

$$
= \frac{2k+1}{s_2-s_1}\int\limits_{s_1}^{s_2} P_l\left(2\frac{s-q_1}{q_2-q_1}-1\right) P_k\left(2\frac{s-s_1}{s_2-s_1}-1\right) ds
$$

$$
= \frac{2k+1}{t_2-t_1}\int\limits_{t_1}^{t_2} P_l(t)P_k\left(2\frac{t-t_1}{t_2-t_1}-1\right) dt
$$

$$
= C_l^k(t_1,t_2),
$$

$$(B.6)$$

where

$$t_1 = 2\frac{s_1 - \frac{q_2+q_1}{2}}{q_2 - q_1}, \quad t_2 = 2\frac{s_2 - \frac{q_2+q_1}{2}}{q_2 - q_1}. \tag{B.7}$$

Let further introduce an auxiliary integral

$$\dot{C}_l^k(t_1, t_2) = \frac{2k+1}{t_2 - t_1}\frac{1}{l}\int\limits_{t_1}^{t_2} \dot{P}_l(t) P_k\left(2\frac{t-t_1}{t_2-t_1} - 1\right) dt, \tag{B.8}$$

where $\dot{P}_l(t) = \frac{d}{dt}P_l(t)$. Finally, using recursion formulas for Legendre's polynomials and their derivatives, after some algebra we obtain a set of recursion formulas that allows us to calculate $C_l^k(t_1, t_2)$, i.e., the required integral

$$C_l^k(t_1, t_2) = \frac{1}{1 + \frac{k+1}{l}}\left(\frac{t_2 - t_1}{2}\frac{2k+1}{2k-1}\dot{C}_l^{k-1}(t_1, t_2) + \frac{t_2 + t_1}{2}\dot{C}_l^k(t_1, t_2) - \left(1 - \frac{1}{l}\right)\dot{C}_{l-1}^k(t_1, t_2)\right),$$

$$\dot{C}_l^k(t_1, t_2) = \left(2 - \frac{1}{l}\right)C_{l-1}^k(t_1, t_2) + \left(1 - \frac{2}{l}\right)\dot{C}_{l-2}^k(t_1, t_2),$$

$$C_l^0(t_1, t_2) = \frac{P_{l+1}(t) - P_{l-1}(t)}{(2l+1)(t_2 - t_1)}\bigg|_{t=t_1}^{t=t_2},$$

$$\dot{C}_l^0(t_1, t_2) = \frac{1}{l}\frac{P_l(t_2) - P_l(t_1)}{t_2 - t_1},$$

$$C_k^k(t_1, t_2) = \left(\frac{t_2 - t_1}{2}\right)^k,$$

$$C_l^k(t_1, t_2) = 0, l < k,$$

$$\dot{C}_l^k(t_1, t_2) = 0, l \leq k.$$

$$\tag{B.9}$$

Appendix C

Description of 1-D conductivity models

C.1   Introduction

In this Appendix, I present the actual values of the recovered layered 1-D conductivity profiles beneath three island geomagnetic observatories, located at Tristan da Cunha (INTERMAGNET code of observatory: TDC), Oahu (INTERMAGNET code of observatory: HON) and Cocos-Keeling (INTERMAGNET code of observatory: CKI) islands, and the globally averaged 1-D mantle structure beneath oceans, which was obtained by a joint inversion of satellite-detected tidal signals and global Q-response, taken from by (Kuvshinov et al., 2021). The results are presented in the form of the tables which contain the depths to the top of each layer, thicknesses, conductivities and 95 % confidence intervals.

Table C.1: The recovered 1-D conductivity profile beneath TDC observatory.

Depth (km)	Thickness (km)	Conductivity (S/m)	Lower bound (S/m)	Upper bound (S/m)
0	0.5	0.01403	0.01144	0.01719
0.5	1.5	0.01404	0.01144	0.01722
2	3	0.01394	0.01134	0.01713
5	5	0.00990	0.00804	0.01217
10	6	0.00701	0.00569	0.00865
16	6	0.00561	0.00454	0.00692
22	6	0.00451	0.00365	0.00557
28	9	0.00449	0.00363	0.00555
37	15	0.00560	0.00452	0.00693
52	13	0.00714	0.00576	0.00886
65	15	0.01576	0.01268	0.01958
80	15	0.04450	0.03579	0.05533
95	17	0.09847	0.07913	0.12253
112	20	0.17615	0.14138	0.21946
132	23	0.25925	0.20742	0.32404
155	24	0.27873	0.22250	0.34916
179	30	0.27810	0.22165	0.34895
209	35	0.22083	0.17562	0.27767
244	35	0.17605	0.13955	0.22209
279	40	0.12329	0.08095	0.18776
319	40	0.09837	0.06447	0.15010
359	40	0.09814	0.06399	0.15054
399	40	0.09849	0.06365	0.15238
439	50	0.09857	0.06334	0.15340
489	60	0.10444	0.06687	0.16309
549	50	0.15447	0.09811	0.24322
599	60	0.25323	0.14766	0.43425
659	70	0.75293	0.43688	1.29763
729	70	1.86950	1.07415	3.25374
799	80	2.12491	1.21693	3.71036
879	100	2.14192	1.22092	3.75766
979	100	2.12568	1.20757	3.74183
1079	110	2.14315	1.18981	3.86037
1189	110	2.27498	1.23640	4.18595
1299	100	2.52767	1.30442	4.89806
1399	100	2.71445	1.33330	5.52629
1499	100	2.94001	1.39553	6.19381
1599	100	3.04248	1.40695	6.57923
1699	100	3.02830	1.36903	6.69859
1799	100	2.92633	1.28666	6.65553
1899	100	2.98552	1.26892	7.02431
1999	200	3.13723	1.31696	7.47340
2199	400	3.21232	1.33728	7.71641
2599	380	3.27468	1.30373	8.22528

Table C.2: The same as in Table C.1, but for HON observatory.

Depth (km)	Thickness (km)	Conductivity (S/m)	Lower bound (S/m)	Upper bound (S/m)
0	0.5	0.00905	0.00452	0.01812
0.5	1.5	0.00904	0.00439	0.01864
2	4	0.00903	0.00433	0.01883
6	4	0.00896	0.00427	0.01882
10	6	0.00885	0.00421	0.01862
16	6	0.00635	0.00300	0.01343
22	6	0.00531	0.00250	0.01127
28	9	0.00463	0.00218	0.00985
37	15	0.00338	0.00159	0.00720
52	13	0.00261	0.00122	0.00559
65	15	0.00235	0.00109	0.00505
80	15	0.00225	0.00104	0.00485
95	17	0.00226	0.00104	0.00487
112	20	0.00245	0.00113	0.00528
132	23	0.00304	0.00140	0.00657
155	24	0.00482	0.00222	0.01043
179	30	0.01007	0.00464	0.02184
209	35	0.03404	0.01567	0.07394
244	35	0.23713	0.10894	0.51615
279	40	0.36807	0.16864	0.80330
319	40	0.32013	0.14600	0.70192
359	40	0.16966	0.07721	0.37280
399	40	0.14067	0.06393	0.30954
439	50	0.13840	0.06259	0.30601
489	60	0.14543	0.06576	0.32161
549	50	0.19770	0.08923	0.43798
599	60	0.30574	0.13739	0.68036
659	70	0.73736	0.33047	1.64524
729	70	1.40478	0.62739	3.14543
799	80	1.64414	0.73345	3.68559
879	100	1.66532	0.74237	3.73574
979	100	1.65531	0.73540	3.72591
1079	110	1.68211	0.74484	3.79876
1189	110	1.74794	0.77328	3.95106
1299	100	1.88636	0.83041	4.28506
1399	100	1.96692	0.86204	4.48790
1499	100	2.04410	0.89528	4.66710
1599	100	2.12305	0.92573	4.86897
1699	100	2.15514	0.92724	5.00909
1799	100	2.28091	0.97720	5.32398
1899	100	2.35821	0.99541	5.58675
1999	200	2.43701	1.00616	5.90264
2199	400	2.51836	1.03493	6.12805
2599	380	2.61724	0.98076	6.98431

Table C.3: The same as in Table C.1, but for CKI observatory.

Depth (km)	Thickness (km)	Conductivity (S/m)	Lower bound (S/m)	Upper bound (S/m)
0	0.5	0.01427	0.01035	0.01969
0.5	1.5	0.01433	0.01038	0.01979
2	5	0.01405	0.01017	0.01943
7	3	0.01247	0.00899	0.01729
10	6	0.01117	0.00802	0.01556
16	6	0.00680	0.00487	0.00949
22	6	0.00459	0.00328	0.00641
28	9	0.00407	0.00290	0.00571
37	15	0.00399	0.00285	0.00561
52	13	0.00401	0.00286	0.00564
65	15	0.00403	0.00286	0.00568
80	15	0.00453	0.00322	0.00639
95	17	0.00563	0.00399	0.00795
112	20	0.00712	0.00504	0.01007
132	23	0.01151	0.00811	0.01634
155	24	0.01720	0.01208	0.02447
179	30	0.01775	0.01247	0.02527
209	35	0.01888	0.01321	0.02699
244	35	0.02468	0.01717	0.03549
279	40	0.02503	0.01723	0.03634
319	40	0.02933	0.02009	0.04281
359	40	0.04100	0.02768	0.06073
399	40	0.04903	0.03281	0.07327
439	50	0.07839	0.04718	0.13024
489	60	0.12457	0.06633	0.23395
549	50	0.36838	0.19526	0.69502
599	60	0.69163	0.36422	1.31335
659	70	1.26771	0.65743	2.44448
729	70	1.30902	0.67567	2.53605
799	80	1.29507	0.66549	2.52026
879	100	1.20896	0.61146	2.39033
979	100	1.16538	0.57384	2.36671
1079	110	1.19633	0.55647	2.57194
1189	110	1.32890	0.60870	2.90120
1299	100	1.64871	0.74525	3.64741
1399	100	2.12515	0.95584	4.72491
1499	100	2.91024	1.28144	6.60935
1599	100	3.02197	1.16164	7.86158
1699	100	3.13449	1.10200	8.91564
1799	100	3.19303	1.11351	9.15608
1899	100	3.17794	1.08345	9.32147
1999	200	3.19564	0.99065	10.3085
2199	400	3.30158	1.00638	10.8313
2599	380	3.29942	0.98375	11.0660

Table C.4: The same as in Table C.1, but for globally averaged 1-D mantle structure beneath oceans taken from by Kuvshinov et al. (2021).

Depth (km)	Thickness (km)	Conductivity (S/m)	Lower bound (S/m)	Upper bound (S/m)
1	10	0.00032	0.00015	0.00069
11	12	0.00032	0.00016	0.00065
23	15	0.00034	0.00016	0.00070
38	15	0.00039	0.00017	0.00091
53	13	0.00050	0.00018	0.00138
66	15	0.00073	0.00024	0.00223
81	15	0.00116	0.00037	0.00370
96	17	0.00203	0.00068	0.00602
113	20	0.00374	0.00155	0.00905
133	23	0.00701	0.00306	0.01606
156	25	0.01293	0.00511	0.03273
181	30	0.02182	0.00956	0.04978
211	35	0.03137	0.01531	0.06429
246	35	0.04030	0.02118	0.07668
281	40	0.04775	0.02331	0.09783
321	40	0.05626	0.02849	0.11108
361	40	0.06939	0.03300	0.14594
401	40	0.09014	0.04158	0.19539
441	50	0.13698	0.06509	0.28830
491	60	0.25818	0.12804	0.52059
551	50	0.55871	0.26782	1.16554
601	60	0.98034	0.56960	1.68726
661	70	1.13267	0.67351	1.90487
731	70	1.17502	0.71936	1.91933
801	80	1.19377	0.74119	1.92270
881	100	1.21470	0.73511	2.00719
981	100	1.22527	0.72305	2.07633
1081	110	1.24674	0.71139	2.18497
1191	110	1.30836	0.67681	2.52924
1301	100	1.49968	0.76569	2.93726
1401	100	1.89385	0.86980	4.12354
1501	100	2.46800	1.12520	5.41326
1601	100	3.18402	1.48421	6.83058
1701	100	3.84989	1.80636	8.20526
1801	100	4.19080	1.90199	9.23387
1901	100	4.32177	1.92951	9.68005
2001	100	4.37388	1.91005	10.01588
2101	100	4.38075	1.74362	11.00642
2201	100	4.36998	1.53189	12.46614
2301	100	4.37026	1.41580	13.49000
2401	100	4.38499	1.26547	15.19443
2501	100	4.38851	1.13948	16.90154
2601	100	4.37654	1.04112	18.39754
2701	100	4.37371	0.99958	19.13727
2801	90	4.37127	0.99070	19.28740

Appendix D

Description of CMAES algorithm

D.1 Introduction

In this Appendix, the $(\mu/\mu_w, \lambda)$-CMAES method adopted in Chapter 4 is summarized. Details on its derivation can be found in Hansen & Ostermeier (2001) and Hansen (2006). A corresponding CMAES algorithm is presented in the next section.

D.2 CMAES algotithm

The algorithm of CMAES is presented in Algorithm 1.

Algorithm 1 $(\mu/\mu_w, \lambda)$-CMAES algorithm

Input: λ, $\mathbf{v}$, s
Initialize: $\mathbf{p}_c^{(0)} = \mathbf{0}$, $\mathbf{p}_s^{(0)} = \mathbf{0}$, $\mathbf{C} = \mathbf{I}$
Set: c_c, c_s, c_μ, d_s, $w_{i,\dots,\lambda}$
while not terminate **do**
    Sample $\mathbf{m}_{i=1,\dots\lambda}$ in eq. D.2
    Update $\mathbf{v}$ using eq. D.3
    Update $\mathbf{p}_c$ using eq. D.5
    Update $\mathbf{p}_s$ using eq. D.7
    Update $\mathbf{C}$ using eq. D.4
    Update s using eq. D.6
end while

Let $\mathbf{m} = [\beta(\sigma_1), \beta(\sigma_2), \cdots, \beta(\sigma_N)]$ denotes the vector of model parameters, where $\beta(\cdot)$ is a log-based transformation ensuring the positivity of the arguments, $\sigma_{i=1,\dots,N}$ are the conductivities of each layer and N is the number of parameters. Users can specify

the values of λ and μ, and the default values are set as

$$\lambda = 4 + \lfloor 3 \log N \rfloor, \quad \mu = \lfloor \lambda/2 \rfloor, \tag{D.1}$$

where $\lfloor \cdot \rfloor$ is the floor function.

CMAES algorithm starts by initializing a number of parameters, including the evolution path ($\mathbf{p}$) and covariance matrix ($\mathbf{C}$), which are

$$\mathbf{p}_c^{(0)} = \mathbf{p}_s^{(0)} = \mathbf{0}, \mathbf{C}^{(0)} = \mathbf{I},$$

where $\mathbf{p}_c$ is the evolution path and $\mathbf{p}_s$ is a "conjugate" evolution path, which will be described later. $\mathbf{I}$ is the unity matrix.

Then, the new object parameter vector $\mathbf{m}_k^{(g+1)}$ is generated by sampling a multivariate normal distribution. The basic equation for sampling the object parameter vector from generation g to $g+1$ reads

$$\mathbf{m}_k^{(g+1)} = \mathbf{v}^{(g)} + s^{(g)} \underbrace{\mathbf{B}^{(g)} \mathbf{D}^{(g)} \mathbf{z}_k^{(g+1)}}_{\sim \mathcal{N}(\mathbf{0}, \mathbf{C}^{(\mathbf{g})})}, \quad k = 1, ..., \lambda, \tag{D.2}$$

where $\mathbf{m}_k^{(g+1)}$ is the object parameter of k-th individual in generation $g+1$. $\mathbf{v}^{(g)}$ is the weighted mean of the μ best individuals of the generation g. $s^{(g)}$ is the step size in generation g. $\mathbf{z}_k^{(g+1)}$ are independent realizations of a $(\mathbf{0}, \mathbf{I})$-normally distributed random vector. $\mathbf{D}^{(g)}$ is a step size matrix. $d_{ij}^{(g)} = 0$ for $i \neq j$ and diagonal elements $d_{ii}^{(g)}$ of $\mathbf{D}^{(g)}$ are square roots of eigenvalues of the covariance matrix $\mathbf{C}^{(g)}$. $\mathbf{B}^{(g)}$ is a rotation matrix. It determines the coordinate system, where the scaling with $\mathbf{D}^{(g)}$ takes place. Columns of $\mathbf{B}^{(g)}$ are defined as the normalized eigenvectors of the covariance matrix $\mathbf{C}^{(g)}$. $\mathbf{C}^{(g)}$ is the covariance matrix of the normally distributed random vector $\mathbf{B}^{(g)} \mathbf{D}^{(g)} \mathcal{N}(\mathbf{0}, \mathbf{I})$. $\mathcal{N}(\mathbf{0}, \mathbf{C}^{(\mathbf{g})}$, a multivariate normal distribution with zero mean and covariance matrix $\mathbf{C}^{(g)}$.

To define the complete iteration step, one needs to calculate $\mathbf{v}^{(g+1)}$, $\mathbf{C}^{(g+1)}$ and $s^{(g+1)}$ for the next generation $g+1$.

The new mean $\mathbf{v}^{(g+1)}$ is the weighted average of μ selected object parameters from

samples $\mathbf{m}_{1,...,\lambda}^{(g+1)}$,

$$\mathbf{v}^{(g+1)} = \mathbf{v}^{(g)} + c_m \sum_{i=1}^{\mu} w_i(\mathbf{m}_{i:\lambda}^{(g+1)} - \mathbf{v}^{(g)}), \tag{D.3}$$

where c_m is a learning rate and $w_{i=1...\mu}$ are positive weight coefficients for recombination. $\mathbf{m}_{i:\lambda}^{(g+1)}$ is the i-th best individual out of $\mathbf{m}_1^{(g+1)}, ..., \mathbf{m}_\lambda^{(g+1)}$. Index $i : \lambda$ represents the i-th best individual and $\phi(\mathbf{m}_{1:\lambda}^{(g+1)}) \leq \phi(\mathbf{m}_{2:\lambda}^{(g+1)}) \leq \cdots \leq \phi(\mathbf{m}_{\lambda:\lambda}^{(g+1)})$, where ϕ is the objective function to be minimized.

Covariance matrix $\mathbf{C}^{(g)}$ is adapted by means of the evolution path $\mathbf{p}_c^{(g+1)}$, which is expressed as

$$\mathbf{C}^{(g+1)} = (1 - c_{cov}) \cdot \mathbf{C}^{(g)} + c_{cov} \cdot \mathbf{p}_c^{(g+1)}(\mathbf{p}_c^{(g+1)})^T, \tag{D.4}$$

where c_{cov} changes the rate of covariance matrix $\mathbf{C}$, $\mathbf{p}_c^{(g+1)}$ is the evolution path at generation $g+1$. For the construction of $\mathbf{p}_c^{(g+1)}$, the "weighted mean selected mutation step" $\mathbf{B}^{(g)}\mathbf{D}^{(g)}\langle\mathbf{z}\rangle_w^{(g+1)}$ is used, which reads

$$\mathbf{p}_c^{(g+1)} = (1 - c_c) \cdot \mathbf{p}_c^{(g)} + c_c^u \cdot \underbrace{c_w\mathbf{B}^{(g)}\mathbf{D}^{(g)}\langle\mathbf{z}\rangle_w^{(g+1)}}_{= \frac{c_w}{s^{(g)}}(\mathbf{v}_w^{(g+1)} - \mathbf{v}_w^{(g)})}, \tag{D.5}$$

where c_c determines the cumulation time for $\mathbf{p}_c$. $c_c^u = \sqrt{c_c(2 - c_c)}$ normalizes the variance of $\mathbf{p}_c$. $c_w = \frac{\sum_{i=1}^u w_i}{\sqrt{\sum_{i=1}^u w_i^2}}$ is chosen under random selection. $\langle\mathbf{z}\rangle_w^{(g+1)} = \frac{1}{\sum_{i=1}^\mu w_i} \sum_{i=1}^\mu w_i\mathbf{z}_{i:\lambda}^{(g+1)}$. The index $i : \lambda$ denotes the index of the i-th best individual from $\mathbf{m}_1^{(g+1)}, ..., \mathbf{m}_\lambda^{(g+1)}$.

The global step size $s^{(g+1)}$ is updated by

$$s^{(g+1)} = s^{(g)} \cdot \exp(\frac{1}{d_s} \cdot \frac{\|\mathbf{p}_s^{(g+1)} - \widehat{\chi}_n\|}{\widehat{\chi}_n}), \tag{D.6}$$

where $d_s \geq 1$ is the damping parameter, which determines the possible change rate of $s^{(g)}$ in the generation sequence. $\widehat{\chi}_n = \mathbb{E}[\|\mathcal{N}(\mathbf{0}, \mathbf{I})\|] = \sqrt{2} \cdot \Gamma(\frac{n+1}{2})/\Gamma(\frac{n}{2})$ is the expectation of the length of a $(\mathbf{0}, \mathbf{I})$-normally distributed random vector. $\mathbf{p}_s^{(g+1)}$ is a "conjugate" evolution path, which reads

$$\mathbf{p}_s^{(g+1)} = (1 - c_s) \cdot \mathbf{p}_s^{(g)} + c_s^u \cdot \underbrace{c_w\mathbf{B}^{(g)}\langle\mathbf{z}\rangle_w^{(g+1)}}_{= \mathbf{B}^{(g)}(\mathbf{D}^{(g)})^{-1}\frac{c_w}{s^{(g)}}(\mathbf{v}^{(g+1)} - \mathbf{v}^{(g)})}, \tag{D.7}$$

where $c_s^u = \sqrt{c_s(1 - c_s)}$ and c_s determines the cumulation time for $\mathbf{p}_s^{(g)}$, which is roughly

$1/c_s$.

Possible termination criteria for the algorithm are: (a) The maximum number of iterations is reached; (b) The maximum number of forward modeling computations is reached; (c) The covariance matrix becomes singular; (d) There are no significant changes in the function value over the last n_f iterations; and (e) There are no significant changes in the mean model over the last n_m iterations.

List of Figures

List of Tables

List of acronyms and their meanings

Acronyms	Full names
1-D, 2-D, 3-D	one-dimensional, two-dimensional, three-dimensional
C2C	Cartesian-to-Cartesian
EM	electromagnetic
FDM	finite-difference method
FEM	finite-element method
FFT	fast Fourier transform
FMM	fast multipole method
G2C	global-to-Cartesian
G2L	global-to-local
GDS	Geomagnetic Depth Sounding
IE	integral equation
MD	matrix decomposition
MT	Magnetotelluric
NIE	nested integral equation
OIE	ocean induction effect
RDC	rim domain concept
RHS	right-hand side
SH	spherical harmonic
Sq	solar quiet
TFs	transfer functions

Bibliography

Alekseev, D., Kuvshinov, A., & Palshin, N., 2015. Compilation of 3D global conductivity model of the Earth for space weather applications, *Earth, Planets and Space*, **67**(1), 1–11.

Amante, C. & Eakins, B. W., 2009. ETOPO1 1 arc-minute global relief model: procedures, data sources and analysis. NOAA technical memorandum NESDIS NGDC-24, *National Geophysical Data Center, NOAA*, **10**, V5C8276M.

Avdeev, D., Kuvshinov, A., & Epova, K., 2002. Three-dimensional modeling of electromagnetic logs from inclined-horizontal wells, *Izv., Phys Solid Earth*, **38**, 975–980.

Avdeev, D., Kuvshinov, A., Pankratov, O., & Newman, G., 2002a. Three-dimensional induction logging problems, Part I: An integral equation solution and model comparisons, *Geophysics*, **67**(2), 413–426.

Avdeev, D. B., Kuvshinov, A. V., Pankratov, O. V., & Newman, G. A., 1997. High-performance three-dimensional electromagnetic modelling using modified Neumann series. Wide-band numerical solution and examples, *Journal of geomagnetism and geoelectricity*, **49**(11-12), 1519–1539.

Baba, K., Utada, H., Goto, T.-n., Kasaya, T., Shimizu, H., & Tada, N., 2010. Electrical conductivity imaging of the philippine sea upper mantle using seafloor magnetotelluric data, *Physics of the Earth and Planetary Interiors*, **183**(1-2), 44–62.

Baba, K., Tada, N., Utada, H., & Siripunvaraporn, W., 2013. Practical incorporation of local and regional topography in three-dimensional inversion of deep ocean magnetotelluric data, *Geophysical Journal International*, **194**(1), 348–361.

Baba, K., Chen, J., Sommer, M., Utada, H., Geissler, W. H., Jokat, W., & Jegen, M., 2017a. Marine magnetotellurics imaged no distinct plume beneath the Tristan da Cunha hotspot in the southern Atlantic Ocean, *Tectonophysics*, **716**, 52–63.

Baba, K., Tada, N., Matsuno, T., Liang, P., Li, R., Zhang, L., Shimizu, H., Abe, N., Hirano, N., Ichiki, M., et al., 2017b. Electrical conductivity of old oceanic mantle in the northwestern Pacific I: 1-D profiles suggesting differences in thermal structure not predictable from a plate cooling model, *Earth, Planets and Space*, **69**(1), 1–23.

Bahr, K. & Filloux, J. H., 1989. Local Sq response functions from EMSLAB data, *Journal of Geophysical Research: Solid Earth*, **94**(B10), 14195–14200.

Bahr, K., Olsen, N., & Shankland, T. J., 1993. On the combination of the magnetotelluric and the geomagnetic depth sounding method for resolving an electrical conductivity increase at 400 km depth, *Geophysical Research Letters*, **20**(24), 2937–2940.

Bai, D., Unsworth, M. J., Meju, M. A., Ma, X., Teng, J., Kong, X., Sun, Y., Sun, J., Wang, L., Jiang, C., et al., 2010. Crustal deformation of the eastern Tibetan plateau revealed by magnetotelluric imaging, *Nature Geoscience*, **3**(5), 358–362.

Banks, R., 1969. Geomagnetic variations and the electrical conductivity of the upper mantle, *Geophysical Journal International*, **17**(5), 457–487.

Becker, J., Sandwell, D., Smith, W., Braud, J., Binder, B., Depner, J., Fabre, D., Factor, J., Ingalls, S., Kim, S., et al., 2009. Global bathymetry and elevation data at 30 arc seconds resolution: Srtm30_plus, *Marine Geodesy*, **32**(4), 355–371.

Bedrosian, P. A. & Feucht, D. W., 2014. Structure and tectonics of the northwestern united states from earthscope usarray magnetotelluric data, *Earth and Planetary Science Letters*, **402**, 275–289.

Berdichevsky, M. N. & Dmitriev, V. I., 2008. *Models and methods of magnetotellurics*, Springer Science & Business Media.

Blatter, D., Naif, S., Key, K., & Ray, A., 2022. A plume origin for hydrous melt at the lithosphere–asthenosphere boundary, *Nature*, **604**(7906), 491–494.

Bohlander, J. & Scambos, T., 2007. Antarctic coastlines and grounding line derived from MODIS Mosaic of Antarctica (MOA), *National Snow and Ice Data Center, Boulder, CO, USA*.

Buchen, J., Marquardt, H., Speziale, S., Kawazoe, T., Ballaran, T. B., & Kurnosov, A., 2018. High-pressure single-crystal elasticity of wadsleyite and the seismic signature of water in the shallow transition zone, *Earth and Planetary Science Letters*, **498**, 77–87.

Canning, F. X., 1989. Singular value decomposition of integral equations of EM and applications to the cavity resonance problem, *IEEE transactions on antennas and propagation*, **37**(9), 1156–1163.

Chave, A. D. & Jones, A. G., 2012. *The magnetotelluric method: Theory and practice*, Cambridge University Press.

Chen, C., Kruglyakov, M., & Kuvshinov, A., 2020. A new method for accurate and efficient modeling of the local ocean induction effects. Application to long-period responses from island geomagnetic observatories, *Geophysical Research Letters*, **47**(8), e2019GL086351.

Chen, C., Kruglyakov, M., & Kuvshinov, A., 2021. Advanced three-dimensional electromagnetic modelling using a nested integral equation approach, *Geophysical Journal International*, **226**(1), 114–130.

Chopping, R. G., Duan, J., Czarnota, K., & Kemp, T., 2016. AusLAMP long period magnetotellurics: progress update and new insights into Victorian geology and mineral prospectivity, *AGU Fall Meeting Abstracts*, pp. GP41A–03.

Dong, H. & Egbert, G. D., 2019. Divergence-free solutions to electromagnetic forward and adjoint problems: a regularization approach, *Geophysical Journal International*, **216**(2), 906–918.

Dong, H., Wei, W., Jin, S., Ye, G., Jones, A. G., Zhang, L., Jing, J., Xie, C., & Yin, Y., 2020. Shaping the surface deformation of central and south Tibetan Plateau: Insights from magnetotelluric array data, *Journal of Geophysical Research: Solid Earth*, **125**(9), e2019JB019206.

Dong, S. & Li, T., 2010. SinoProbe - A multidisciplinary research program of Earth sciences in China, *AGU Fall Meeting Abstracts*, pp. T42B–08.

Egbert, G. D. & Booker, J. R., 1992. Very long period magnetotellurics at Tucson observatory: implications for mantle conductivity, *Journal of Geophysical Research: Solid Earth*, **97**(B11), 15099–15112.

Egbert, G. D. & Kelbert, A., 2012. Computational recipes for electromagnetic inverse problems, *Geophysical Journal International*, **189**(1), 251–267.

Everett, M. E., Constable, S., & Constable, C. G., 2003. Effects of near-surface conductance on global satellite induction responses, *Geophysical Journal International*, **153**(1), 277–286.

Fainberg, E., Kuvshinov, A., & Singer, B., 1990. Electromagnetic induction in a spherical Earth with non-uniform oceans and continents in electric contact with the underlying medium, II. Bimodal global geomagnetic sounding of the lithosphere, *Geophysical Journal International*, **102**, 283–286.

Farquharson, C. G. & Miensopust, M. P., 2011. Three-dimensional finite-element modelling of magnetotelluric data with a divergence correction, *Journal of Applied Geophysics*, **75**(4), 699–710.

Fei, H., Yamazaki, D., Sakurai, M., Miyajima, N., Ohfuji, H., Katsura, T., & Yamamoto, T., 2017. A nearly water-saturated mantle transition zone inferred from mineral viscosity, *Science Advances*, **3**(6), e1603024.

Finlay, C., Lesur, V., Thébault, E., Vervelidou, F., Morschhauser, A., & Shore, R., 2017. Challenges handling magnetospheric and ionospheric signals in internal geomagnetic field modelling, *Space Science Reviews*, **206**(1), 157–189.

Grayver, A. V., 2021. Global 3-D Electrical Conductivity Model of the World Ocean and Marine Sediments, *Geochemistry, Geophysics, Geosystems*, **22**(9), e2021GC009950.

Grayver, A. V. & Bürg, M., 2014. Robust and scalable 3-D geo-electromagnetic modelling approach using the finite element method, *Geophysical Journal International*, **198**(1), 110–125.

Grayver, A. V. & Kolev, T. V., 2015. Large-scale 3D geoelectromagnetic modeling using parallel adaptive high-order finite element method, *Geophysics*, **80**(6), E277–E291.

Grayver, A. V. & Kuvshinov, A. V., 2016. Exploring equivalence domain in nonlinear inverse problems using Covariance Matrix Adaption Evolution Strategy (CMAES) and random sampling, *Geophysical Journal International*, **205**(2), 971–987.

Grayver, A. V., Schnepf, N. R., Kuvshinov, A. V., Sabaka, T. J., Manoj, C., & Olsen, N., 2016. Satellite tidal magnetic signals constrain oceanic lithosphere-asthenosphere boundary, *Science Advances*, **2**(9), e1600798.

Grayver, A. V., Munch, F. D., Kuvshinov, A. V., Khan, A., Sabaka, T. J., & Tøffner-Clausen, L., 2017. Joint inversion of satellite-detected tidal and magnetospheric signals constrains electrical conductivity and water content of the upper mantle and transition zone, *Geophysical Research Letters*, **44**(12), 6074–6081.

Grayver, A. V., van Driel, M., & Kuvshinov, A. V., 2019. Three-dimensional magnetotelluric modeling in spherical Earth, *Geophysical Journal International*, **217**(1), 532–557.

Gumerov, N. A. & Duraiswami, R., 2005. *Fast multipole methods for the Helmholtz equation in three dimensions*, Elsevier.

Guzavina, M., 2020. *Novel approaches for probing upper mantle electrical conductivity using solar quiet variations: Improved data processing and transfer functions*, Ph.D. thesis, ETH Zurich.

Guzavina, M., Grayver, A., & Kuvshinov, A., 2018. Do ocean tidal signals influence recovery of solar quiet variations?, *Earth, Planets and Space*, **70**(1), 1–15.

Guzavina, M., Grayver, A., & Kuvshinov, A., 2019. Probing upper mantle electrical conductivity with daily magnetic variations using global-to-local transfer functions, *Geophysical Journal International*, **219**(3), 2125–2147.

Haber, E. & Ascher, U. M., 2001. Fast finite volume simulation of 3D electromagnetic problems with highly discontinuous coefficients, *SIAM Journal on Scientific Computing*, **22**(6), 1943–1961.

Haber, E. & Ruthotto, L., 2014. A multiscale finite volume method for Maxwell's equations at low frequencies, *Geophysical Journal International*, **199**(2), 1268–1277.

Han, B., Li, Y., & Li, G., 2018. 3D forward modeling of magnetotelluric fields in general anisotropic media and its numerical implementation in Julia, *Geophysics*, **83**(4), F29–F40.

Han, Q., Kelbert, A., & Hu, X., 2021. An electrical conductivity model of a coastal geothermal field in southeastern China based on 3D magnetotelluric imaging, *Geophysics*, **86**(4), B265–B276.

Hansen, N., 2006. The CMA evolution strategy: a comparing review, *Towards a new evolutionary computation*, pp. 75–102.

Hansen, N. & Ostermeier, A., 2001. Completely derandomized self-adaptation in evolution strategies, *Evolutionary computation*, **9**(2), 159–195.

Hansen, P. C., 1992. Analysis of discrete ill-posed problems by means of the L-curve, *SIAM review*, **34**(4), 561–580.

Heinson, G., Constable, S., & White, A., 1996. Seafloor magnetotelluric sounding above axial seamount, *Geophysical research letters*, **23**(17), 2275–2278.

Heinson, G. S., Direen, N. G., & Gill, R. M., 2006. Magnetotelluric evidence for a deep-crustal mineralizing system beneath the olympic dam iron oxide copper-gold deposit, southern australia, *Geology*, **34**(7), 573–576.

Hursan, G. & Zhdanov, M. S., 2002. Contraction integral equation method in three-dimensional electromagnetic modeling, *Radio Science*, **37**(6), 1–13.

Jahandari, H. & Farquharson, C. G., 2014. A finite-volume solution to the geophysical electromagnetic forward problem using unstructured grids, *Geophysics*, **79**(6), E287–E302.

Johansen, S. E., Panzner, M., Mittet, R., Amundsen, H. E. F., Lim, A., Vik, E., Landrø, M., & Arntsen, B., 2019. Deep electrical imaging of the ultraslow-spreading Mohns Ridge, *Nature*, **567**(7748), 379–383.

Jones, A. G., 1999. Imaging the continental upper mantle using electromagnetic methods, *Lithos*, **48**(1-4), 57–80.

Kamm, J. & Pedersen, L. B., 2014. Inversion of airborne tensor VLF data using integral equations, *Geophysical Journal International*, **198**(2), 775–794.

Karato, S.-i., 2011. Water distribution across the mantle transition zone and its implications for global material circulation, *Earth and Planetary Science Letters*, **301**(3-4), 413–423.

Karato, S.-i. & Wang, D., 2013. Electrical conductivity of minerals and rocks, *Physics and Chemistry of the Deep Earth*, pp. 145–182.

Käufl, J. S., Grayver, A. V., Comeau, M. J., Kuvshinov, A. V., Becken, M., Kamm, J., Batmagnai, E., & Demberel, S., 2020. Magnetotelluric multiscale 3-d inversion reveals crustal and upper mantle structure beneath the hangai and gobi-altai region in mongolia, *Geophysical Journal International*, **221**(2), 1002–1028.

Kelbert, A., Schultz, A., & Egbert, G., 2009. Global electromagnetic induction constraints on transition-zone water content variations, *Nature*, **460**(7258), 1003–1006.

Kelbert, A., Kuvshinov, A., Velímský, J., Koyama, T., Ribaudo, J., Sun, J., Martinec, Z., & Weiss, C. J., 2014. Global 3-D electromagnetic forward modelling: A benchmark study, *Geophysical Journal International*, **197**(2), 785–814.

Key, K., 2016. MARE2DEM: a 2-D inversion code for controlled-source electromagnetic and magnetotelluric data, *Geophysical Journal International*, **207**(1), 571–588.

Key, K. & Weiss, C., 2006. Adaptive finite-element modeling using unstructured grids: The 2D magnetotelluric example, *Geophysics*, **71**(6), G291–G299.

Key, K., Constable, S., Liu, L., & Pommier, A., 2013. Electrical image of passive mantle upwelling beneath the northern East Pacific Rise, *Nature*, **495**, 499–502.

Khan, A., 2016. On Earth's Mantle Constitution and Structure from Joint Analysis of Geophysical and Laboratory-Based Data: An Example, *Surveys in Geophysics*, **37**(1), 149–189.

Khan, A., Kuvshinov, A., & Semenov, A., 2011. On the heterogeneous electrical conductivity structure of the earth's mantle with implications for transition zone water content, *Journal of Geophysical Research: Solid Earth*, **116**(B01103).

Koyama, T., Utada, H., & Avdeev, D., 2008. Fast and memory-saved 3-D forward modeling code for MT by using integral equation method, in *Abstract Book, Proceedings of the 19th Workshop on Electromagnetic induction in the Earth*.

Kruglyakov, M. & Bloshanskaya, L., 2017. High-performance parallel solver for integral equations of electromagnetics based on galerkin method, *Mathematical Geosciences*, **49**(6), 751–776.

Kruglyakov, M. & Kuvshinov, A., 2018. Using high-order polynomial basis in 3-D EM forward modeling based on volume integral equation method, *Geophysical Journal International*, **213**(2), 1387–1401.

Kruglyakov, M. & Kuvshinov, A., 2022. Modelling tippers on a spheres, *Geophysical Journal International*, **231**(2), 737–748.

Kruglyakov, M., Geraskin, A., & Kuvshinov, A., 2016. Novel accurate and scalable 3-d mt forward solver based on a contracting integral equation method, *Computers & Geosciences*, **96**, 208–217.

Kuvshinov, A., 2008. 3-D global induction in the oceans and solid earth: recent progress in modeling magnetic and electric fields from sources of magnetospheric, ionospheric and oceanic origin, *Surveys in Geophysics*, **29**(2), 139–186.

Kuvshinov, A. & Semenov, A., 2012. Global 3-D imaging of mantle electrical conductivity based on inversion of observatory C-responses – I. An approach and its verification, *Geophysical Journal International*, **189**, 1335–1352.

Kuvshinov, A., Utada, H., Avdeev, D., & Koyama, T., 2005. 3-D modelling and analysis of Dst C-responses in the North Pacific Ocean region, revisited, *Geophysical Journal International*, **160**(2), 505–526.

Kuvshinov, A., Grayver, A., Tøffner-Clausen, L., & Olsen, N., 2021. Probing 3-D electrical conductivity of the mantle using 6 years of Swarm, CryoSat-2 and observatory

magnetic data and exploiting matrix Q-responses approach, *Earth, Planets and Space*, **73**(1), 1–26.

Kuvshinov, A. V., Olsen, N., Avdeev, D. B., & Pankratov, O. V., 2002. Electromagnetic induction in the oceans and the anomalous behaviour of coastal C-responses for periods up to 20 days, *Geophysical Research Letters*, **29**(12), 1–4.

Larsen, J., 1975. Low frequency (0.1-6.0 cpd) electromagnetic study of deep mantle electrical conductivity beneath the Hawaiian islands, *Geophys. J. R. astr. Soc.*, **43**, 17–46.

Li, G., Cai, H., & Li, C.-F., 2019a. Alternating joint inversion of controlled-source electromagnetic and seismic data using the joint total variation constraint, *IEEE Transactions on Geoscience and Remote Sensing*, **57**(8), 5914–5922.

Li, J., Liu, J., Egbert, G. D., Liu, R., Guo, R., & Pan, K., 2019b. An efficient preconditioner for 3-D finite difference modeling of the electromagnetic diffusion process in the frequency domain, *IEEE Transactions on Geoscience and Remote Sensing*, **58**(1), 500–509.

Li, S., Weng, A., Zhang, Y., Schultz, A., Li, Y., Tang, Y., Zou, Z., & Zhou, Z., 2020. Evidence of bermuda hot and wet upwelling from novel three-dimensional global mantle electrical conductivity image, *Geochemistry, Geophysics, Geosystems*, **21**(6), e2020GC009016.

Lu, Z., Audet, P., Li, C.-F., Zhu, S., & Wu, Z., 2021. What controls effective elastic thickness of the lithosphere in the pacific ocean?, *Journal of Geophysical Research: Solid Earth*, **126**(3), e2020JB021074.

Mackie, R. L., Smith, J. T., & Madden, T. R., 1994. Three-dimensional electromagnetic modeling using finite difference equations: The magnetotelluric example, *Radio Science*, **29**(4), 923–935.

Matsuno, T., Baba, K., & Utada, H., 2020. Probing 1-D electrical anisotropy in the oceanic upper mantle from seafloor magnetotelluric array data, *Geophysical Journal International*, **222**(3), 1502–1525.

McAdoo, D. C. & Sandwell, D. T., 1985. Folding of oceanic lithosphere, *Journal of Geophysical Research: Solid Earth*, **90**(B10), 8563–8569.

Meqbel, N. M., Egbert, G. D., Wannamaker, P. E., Kelbert, A., & Schultz, A., 2014. Deep electrical resistivity structure of the northwestern US derived from 3-D inversion of USArray magnetotelluric data, *Earth and Planetary Science Letters*, **402**, 290–304.

Mitsuhata, Y. & Uchida, T., 2004. 3D magnetotelluric modeling using the T-Ω finite-element method, *Geophysics*, **69**(1), 108–119.

Mogi, T., 1996. Three-dimensional modeling of magnetotelluric data using finite element method, *Journal of Applied Geophysics*, **35**(2-3), 185–189.

Morschhauser, A., Grayver, A., Kuvshinov, A., Samrock, F., & Matzka, J., 2019. Tippers at island geomagnetic observatories constrain electrical conductivity of oceanic lithosphere and upper mantle, *Earth, Planets and Space*, **71**(1), 1–9.

Müller, R. D., Sdrolias, M., Gaina, C., & Roest, W. R., 2008. Age, spreading rates, and spreading asymmetry of the world's ocean crust, *Geochemistry, Geophysics, Geosystems*, **9**(4), Q04006.

Munch, F. D., Grayver, A. V., Kuvshinov, A., & Khan, A., 2018. Stochastic inversion of geomagnetic observatory data including rigorous treatment of the ocean induction effect with implications for transition zone water content and thermal structure, *Journal of Geophysical Research: Solid Earth*, **123**(1), 31–51.

Munch, F. D., Grayver, A. V., Guzavina, M., Kuvshinov, A. V., & Khan, A., 2020. Joint inversion of daily and long-period geomagnetic transfer functions reveals lateral variations in mantle water content, *Geophysical Research Letters*, **47**(10), e2020GL087222.

Murphy, B. S. & Egbert, G. D., 2017. Electrical conductivity structure of southeastern north america: Implications for lithospheric architecture and appalachian topographic rejuvenation, *Earth and Planetary Science Letters*, **462**, 66–75.

Naif, S., Key, K., Constable, S., & Evans, R., 2013. Melt-rich channel observed at the lithosphere-astenosphere boundary, *Nature*, **495**, 356–359.

Newman, G. A. & Alumbaugh, D. L., 2002. Three-dimensional induction logging problems, Part 2: A finite-difference solution, *Geophysics*, **67**(2), 484–491.

Nie, X. C., Yuan, N., & Liu, R., 2013. A fast integral equation solver for 3D induction well logging in formations with large conductivity contrasts, *Geophysical Prospecting*, **61**(3), 645–657.

Olsen, N., 1992. Day-to-day C-response estimation for Sq from 1 cpd to 6 cpd using the Z: Y-method, *Journal of geomagnetism and geoelectricity*, **44**(6), 433–447.

Olsen, N., 1998. The electrical conductivity of the mantle beneath europe derived from c-responses from 3 to 720 hr, *Geophysical Journal International*, **133**(2), 298–308.

Olsen, N. & Floberghagen, R., 2018. Exploring Geospace from Space: the Swarm Satellite Constellation Mission, *Space Research Today*, **203**, 61–71.

Palshin, N. A., 1996. Oceanic electromagnetic studies: a review, *Surveys in Geophysics*, **17**(4), 455–491.

Pankratov, O. & Kuvshinov, A., 2016. Applied mathematics in EM studies with special emphasis on an uncertainty quantification and 3-D integral equation modelling, *Surveys in Geophysics*, **37**(1), 109–147.

Parkinson, W. & Jones, F., 1979. The geomagnetic coast effect, *Reviews of Geophysics*, **17**(8), 1999–2015.

Patro, P. K. & Egbert, G. D., 2008. Regional conductivity structure of cascadia: Preliminary results from 3d inversion of usarray transportable array magnetotelluric data, *Geophysical Research Letters*, **35**(20), L20311.

Phillips, J. R. & White, J. K., 1997. A precorrected-FFT method for electrostatic analysis of complicated 3-D structures, *IEEE Transactions on Computer-Aided Design of Integrated Circuits and Systems*, **16**(10), 1059–1072.

Püthe, C., 2015. *Interpretation of global EM induction data from ground, sea and space: New response functions, inversion schemes and conductivity models*, Ph.D. thesis, ETH Zurich.

Püthe, C. & Kuvshinov, A., 2014. Mapping 3-D mantle electrical conductivity from space: a new 3-D inversion scheme based on analysis of matrix Q-responses, *Geophysical Journal International*, **197**(2), 768–784.

Püthe, C., Manoj, C., & Kuvshinov, A., 2014. Reproducing electric field observations during magnetic storms by means of rigorous 3-D modelling and distortion matrix co-estimation, *Earth, Planets and Space*, **66**(1), 1–10.

Püthe, C., Kuvshinov, A., & Olsen, N., 2015. Handling complex source structures in global EM induction studies: from C-responses to new arrays of transfer functions, *Geophysical Journal International*, **201**(1), 318–328.

Ranalli, G., 1995. *Rheology of the Earth*, Springer Science & Business Media.

Ren, Z., Kalscheuer, T., Greenhalgh, S., & Maurer, H., 2013a. A goal-oriented adaptive finite-element approach for plane wave 3-D electromagnetic modelling, *Geophysical Journal International*, **194**(2), 700–718.

Ren, Z., Kalscheuer, T., Greenhalgh, S., & Maurer, H., 2013b. Boundary element solutions for broad-band 3-D geo-electromagnetic problems accelerated by an adaptive multilevel fast multipole method, *Geophysical Journal International*, **192**(2), 473–499.

Ren, Z., Kalscheuer, T., Greenhalgh, S., & Maurer, H., 2014. A finite-element-based domain-decomposition approach for plane wave 3D electromagnetic modeling, *Geophysics*, **79**(6), E255–E268.

Rigaud, R., Kruglyakov, M., Kuvshinov, A., Pinheiro, K. J., Petereit, J., Matzka, J., & Marshalko, E., 2021. Exploring effects in tippers at island geomagnetic observatories due to realistic depth-and time-varying oceanic electrical conductivity, *Earth, Planets and Space*, **73**(1), 1–22.

Robertson, K., Taylor, D., Thiel, S., & Heinson, G., 2015. Magnetotelluric evidence for serpentinisation in a Cambrian subduction zone beneath the Delamerian Orogen, southeast Australia, *Gondwana Research*, **28**(2), 601–611.

Robertson, K., Heinson, G., & Thiel, S., 2016. Lithospheric reworking at the proterozoic–phanerozoic transition of australia imaged using auslamp magnetotelluric data, *Earth and Planetary Science Letters*, **452**, 27–35.

Rychert, C. A. & Shearer, P. M., 2009. A global view of the lithosphere-asthenosphere boundary, *Science*, **324**(5926), 495–498.

Rychert, C. A. & Shearer, P. M., 2011. Imaging the lithosphere-asthenosphere boundary beneath the Pacific using SS waveform modeling, *Journal of Geophysical Research: Solid Earth*, **116**(B7), B07307.

Rychert, C. A., Laske, G., Harmon, N., & Shearer, P. M., 2013. Seismic imaging of melt in a displaced hawaiian plume, *Nature Geoscience*, **6**(8), 657–660.

Samrock, F. & Kuvshinov, A., 2013. Tippers at island observatories: Can we use them to probe electrical conductivity of the earth's crust and upper mantle?, *Geophysical Research Letters*, **40**, 824–828.

Schlömer, A., Geissler, W. H., Jokat, W., & Jegen, M., 2017. Hunting for the Tristan mantle plume–An upper mantle tomography around the volcanic island of Tristan da Cunha, *Earth and Planetary Science Letters*, **462**, 122–131.

Schmucker, U., 1964. Anomalies of geomagnetic variations in the southwestern united states, *Journal of geomagnetism and geoelectricity*, **15**(4), 193–221.

Schmucker, U., 1985. Magnetic and electric fields due to electromagnetic induction by external sources, electrical properties of the earth's interior, *Landolt-Bornstein*, pp. New–Series.

Schmucker, U., 1999a. A spherical harmonic analysis of solar daily variations in the years 1964-1965: response estimates and source fields for global induction-II.Results., *Geophysical Journal International*, **136**, 455–476.

Schmucker, U., 1999b. A spherical harmonic analysis of solar daily variations in the years 1964-1965 – I. Methods, *Geophysical Journal International*, **136**, 439–454.

Schultz, A., 2010. EMScope: A Continental Scale Magnetotelluric Observatory and Data Discovery Resource, *Data Science Journal*, **8**(February), IGY6–IGY20.

Schulze, K., Marquardt, H., Kawazoe, T., Ballaran, T. B., McCammon, C., Koch-Müller, M., Kurnosov, A., & Marquardt, K., 2018. Seismically invisible water in earth's transition zone?, *Earth and Planetary Science Letters*, **498**, 9–16.

Selway, K., Hand, M., Payne, J., Heinson, G. S., & Reid, A., 2011. Magnetotelluric constraints on the tectonic setting of grenville-aged orogenesis in central australia, *Journal of the Geological Society*, **168**(1), 251–264.

Semenov, A. & Kuvshinov, A., 2012. Global 3-D imaging of mantle conductivity based on inversion of observatory C-responses-II. data analysis and results, *Geophysical Journal International*, **191**(3), 965–992.

Shimizu, H., Utada, H., Baba, K., Koyama, T., Obayashi, M., & Fukao, Y., 2010. Three-dimensional imaging of electrical conductivity in the mantle transition zone beneath the north pacific ocean by a semi-global induction study, *Physics of the Earth and Planetary Interiors*, **183**(1-2), 252–269.

Simpson, F., Steveling, E., & Leven, M., 2000. The effect of the hawaiian plume on the magnetic daily variation, *Geophysical research letters*, **27**(12), 1775–1778.

Singer, B. S., 2008. Electromagnetic integral equation approach based on contraction operator and solution optimization in Krylov subspace, *Geophysical Journal International*, **175**(3), 857–884.

Snyder, J., 1982. Map projections used by the US Geological survey, Tech. rep., US Government Printing Office.

St-Louis, B., Sauter, E., & Coles, R., 2011. INTERMAGNET technical reference manual, version 4.5, INTERMAGNET.

Suetsugu, D., Shiobara, H., Sugioka, H., Ito, A., Isse, T., Kasaya, T., Tada, N., Baba, K., Abe, N., Hamano, Y., et al., 2012. TIARES Project-Tomographic investigation by seafloor array experiment for the Society hotspot, *Earth, planets and space*, **64**(4), i–iv.

Sun, J. & Kuvshinov, A., 2015. Accelerating EM integral equation forward solver for global geomagnetic induction using SVD based matrix compression method, *Geophysical Journal International*, **200**(2), 1005–1011.

Tada, N., Baba, K., & Utada, H., 2014. Three-dimensional inversion of seafloor magnetotelluric data collected in the philippine sea and the western margin of the northwest pacific ocean, *Geochemistry, Geophysics, Geosystems*, **15**(7), 2895–2917.

Turcotte, D. L. & Schubert, G., 2002. *Geodynamics*, Cambridge university press.

Utada, H. & Baba, K., 2014. Estimating the electrical conductivity of the melt phase of a partially molten asthenosphere from seafloor magnetotelluric sounding data, *Physics of the Earth and Planetary Interiors*, **227**, 41–47.

Varilsuha, D. & Candansayar, M. E., 2018. 3d magnetotelluric modeling by using finite-difference method: Comparison study of different forward modeling approaches, *Geophysics*, **83**(2), WB51–WB60.

Velímskỳ, J., Grayver, A., Kuvshinov, A., & Šachl, L., 2018. On the modelling of M2 tidal magnetic signatures: effects of physical approximations and numerical resolution, *Earth, Planets and Space*, **70**(1), 1–15.

Wei, W., Unsworth, M., Jones, A., Booker, J., Tan, H., Nelson, D., Chen, L., Li, S., Solon, K., Bedrosian, P., et al., 2001. Detection of widespread fluids in the Tibetan crust by magnetotelluric studies, *Science*, **292**(5517), 716–719.

Weidelt, P., 1972. The inverse problem of geomagnetic induction, *J. Geophys.*, **38**, 257–289.

Wessel, P. & Smith, W. H., 1996. A global, self-consistent, hierarchical, high-resolution shoreline database, *Journal of Geophysical Research: Solid Earth*, **101**(B4), 8741–8743.

Winterbourne, J., Crosby, A., & White, N., 2009. Depth, age and dynamic topography of oceanic lithosphere beneath heavily sedimented atlantic margins, *Earth and Planetary Science Letters*, **287**(1-2), 137–151.

Wolfe, C. J., Solomon, S. C., Laske, G., Collins, J. A., Detrick, R. S., Orcutt, J. A., Bercovici, D., & Hauri, E. H., 2009. Mantle shear-wave velocity structure beneath the hawaiian hot spot, *Science*, **326**(5958), 1388–1390.

Woods, M. T. & Okal, E. A., 1996. Rayleigh-wave dispersion along the hawaiian swell: a test of lithospheric thinning by thermal rejuvenation at a hotspot, *Geophysical Journal International*, **125**(2), 325–339.

Woods, M. T., Lévêque, J.-J., Okal, E. A., & Cara, M., 1991. Two-station measurements of rayleigh wave group velocity along the hawai'ian swell, *Geophysical Research Letters*, **18**(1), 105–108.

Xu, S., Unsworth, M. J., Hu, X., & Mooney, W. D., 2019. Magnetotelluric evidence for asymmetric simple shear extension and lithospheric thinning in south china, *Journal of Geophysical Research: Solid Earth*, **124**(1), 104–124.

Xu, Y., Yang, B., Zhang, A., Wu, S., Zhu, L., Yang, Y., Wang, Q., & Xia, Q., 2020. Magnetotelluric imaging of a fossil oceanic plate in northwestern xinjiang, china, *Geology*, **48**(4), 385–389.

Yamazaki, Y. & Maute, A., 2017. Sq and EEJ-A review on the daily variation of the geomagnetic field caused by ionospheric dynamo currents, *Space Science Reviews*, **206**(1), 299–405.

Yamazaki, Y., Häusler, K., & Wild, J. A., 2016. Day-to-day variability of midlatitude ionospheric currents due to magnetospheric and lower atmospheric forcing, *Journal of Geophysical Research: Space Physics*, **121**(7), 7067–7086.

Yang, B., Egbert, G. D., Kelbert, A., & Meqbel, N. M., 2015. Three-dimensional electrical resistivity of the north-central USA from EarthScope long period magnetotelluric data, *Earth and Planetary Science Letters*, **422**, 87–93.

Yang, B., Egbert, G. D., Zhang, H., Meqbel, N., & Hu, X., 2021. Electrical resistivity imaging of continental united states from three-dimensional inversion of earthscope usarray magnetotelluric data, *Earth and Planetary Science Letters*, **576**, 117244.

Yin, Y., Jin, S., Wei, W., Ye, G., Zhang, L., Dong, H., Xie, C., Liang, H., et al., 2017. Lithospheric rheological heterogeneity across an intraplate rift basin (linfen basin, north china) constrained from magnetotelluric data: Implications for seismicity and rift evolution, *Tectonophysics*, **717**, 1–15.

Yoshimura, R. & Oshiman, N., 2002. Edge-based finite element approach to the simulation of geoelectromagnetic induction in a 3-D sphere, *Geophysical Research Letters*, **29**(3), 1–9.

Yoshino, T., 2010. Laboratory electrical conductivity measurement of mantle minerals, *Surveys in Geophysics*, **31**(2), 163–206.

Yoshino, T. & Katsura, T., 2013. Electrical conductivity of mantle minerals: role of water in conductivity anomalies, *Annual Review of Earth and Planetary Sciences*, **41**, 605–628.

Zhang, L., Jin, S., Wei, W., Ye, G., Jing, J., Dong, H., & Xie, C., 2015. Lithospheric electrical structure of South China imaged by magnetotelluric data and its tectonic implications, *Journal of Asian Earth Sciences*, **98**, 178–187.

Zhdanov, M. S., Varentsov, I. M., Weaver, J. T., Golubev, N. G., & Krylov, V. A., 1997. Methods for modelling electromagnetic fields results from COMMEMI - The international project on the comparison of modelling methods for electromagnetic induction, *Journal of Applied Geophysics*, **37**(3-4), 133–271.

Acknowledgements

Working on this Ph.D. project has been a tremendous and unforgettable experience for me, both academic and personal. This work would not happen without the support and help from a number of people.

First and foremost, I would like to thank Prof. Dr. Alexey Kuvshinov for your thoughtful supervision and support. During my four-year study here, I would not finish the dissertation without your consent. Thank you for kindly offering me an opportunity to be a Ph.D. student in the Earth and Planetary Magnetism group. Your broad knowledge in deep electromagnetic studies profoundly impacted my work. Thank you for always being available (even on weekends) for discussions. Thank you for your incredible patience and word-by-word checking of the posters, presentations, and manuscripts. I appreciate your help with preparing the SNF Mobility grant proposal, which significantly improved its quality. There is a slang in China that is one day is a teacher, life is a father. I enjoyed working with you, and it is my honor to be your Ph.D. student. I will continue to work hard and contribute to the community of deep electromagnetic studies.

The sincerest thanks are dedicated to Dr. Mikhail Kruglyakov, my co-supervisor. Your solid mathematical foundation and advanced programming skills impressed me and helped me a lot in my study. Without your help, I couldn't reach the final stage. I still remember always struggling with the project, especially in the first one and half years. When I came up with some weird results, your careful analysis and reasonable explanations helped me improve my learning.

Special thanks are given to Dr. Federico Munch (previous Ph.D. student in ETH and now the postdoc at the University of California Berkeley). Thank you a lot for your help in both science and life when I came to Zürich and started studying here. I would like to also thank Ph.D. student in ETH Rafael Rigaud for your help with estimating

the electromagnetic transfer functions used in my research.

My great thanks are given to Pengfei Liu, Mingqi Liu, Leonardo Echeverria, Yujie Liu, Felix Bissig, Johannes Käufl, Martina Guzavina, Jun Yan, Rui Wu, Xun Li and Johannes Kemper. It was a great time being with you all at ETH.

In particular, I am highly thankful to Prof. Dr. Zhengyong Ren in Central South University, China, for your constant support both in science and my personal life. My passion for electromagnetic studies came from when I was a master's student of you. Thank you for recommending that I pursue the Ph.D. degree in ETH Zürich. Also, I would like to express my deep thank to you for helping to apply for the data from Chinese geomagnetic observatories. Thank you for your guide when I was confused about my work and life.

My final thanks are given to my parents, sister, and Cuiyi Zhang. Without your understanding and support in the past four years, especially during the pandemic, I can't study here, pursue the degree and write the thesis.

Chaojian Chen

Personal Information

Major	Geophysics
Data of birth	02.04.1993
Citizenship	China
Email	chaojian.chen@outlook.com

Education

2018–2022	PhD student in geophysics at the Department of Earth Sciences, ETH Zürich, Switzerland
2015–2018	MSc student in geophysics at the School of Geosciences and Info-physics, Central South University, China
2011–2015	BSc student in geophysics at the School of Geosciences and Info-physics, Central South University, China

Peer-reviewed journals

- **Chen, C.**, Kuvshinov, A., Kruglyakov, M., Munch, F., & Rigaud, R. 2022. Constraining the crustal and mantle conductivity structures beneath islands by a joint inversion of multi-source magnetic transfer functions. *Journal of Geophysical Research: Solid Earth*, revision submitted.
- **Chen, C.**, Kruglyakov, M., & Kuvshinov, A. 2021. Advanced three-dimensional electromagnetic modeling using a nested integral equation approach. *Geophysical Journal International*, 226(1): 114-130.
- **Chen, C.**, Kruglyakov, M., & Kuvshinov, A. 2020. A new method for accurate and efficient modeling of the local ocean induction effects. Application to long-period responses from island geomagnetic observatories. *Geophysical Research Letters*, 47(8), e2019GL086351.

- **Chen, C.**, Ren, Z., Pan, K., Tang, J., Kalscheuer, T., Maurer, H., Sun, Y., & Li, Y. 2018. Exact solutions of the vertical gravitational anomaly for a polyhedral prism with vertical polynomial density contrast of arbitrary orders. *Geophysical Journal International*, 214(3), 2115-2132.

Conferences

- **Chen, C.**, Kuvshinov, A., Kruglyakov, M., Munch, F., & Rigaud, R. Constraining the crustal and mantle conductivity structures beneath islands by a joint inversion of multi-source magnetic transfer functions, Electromagnetic Induction Workshops 2022, Turkey, September 2022.
- **Chen, C.**, Kruglyakov, M., Rigaud, R., & Kuvshinov, A. Constraining crustal and upper mantle conductivity beneath islands by a joint inversion of multi-source transfer functions, IAGA – IASPEI 2021, Online, August 21-27, 2021.
- **Chen, C.**, Kruglyakov, M., Rigaud, R., & Kuvshinov, A. Joint inversion of magnetotelluric tippers and geomagnetic depth sounding transfer functions constrains electrical conductivity beneath islands, EGU General Assembly 2021, Online, 25-28 April 2021.
- **Chen, C.**, Kruglyakov, M., & Kuvshinov, A. An efficient 3-D electromagnetic forward modeling based on a nested integral equation approach, AGU Fall Meeting 2020, GP005-02, Oral presentation, Online, 4–17 December 2020.
- **Chen, C.**, Kruglyakov, M., & Kuvshinov, A. Global-to-Cartesian 3-D EM modeling using a nested IE approach with application to long-period responses from island geomagnetic observatories, EGU General Assembly 2020, Online, 4–8 May 2020.

Miscellaneous

Language skills

- Chinese
- English

Programming skills

- C
- C++
- Fortran
- Matlab